Measurement of CP Violation in B0 to Phi K0, and of Branching Fraction and CP Violation in B0 to F0(980) K0(S)

Paul E. Kutter

SLAC-R-895

Prepared for the Department of Energy
under contract number DE-AC02-76SF00515

Printed in the United States of America. Available from the National Technical Information Service, U.S. Department of Commerce, 5285 Port Royal Road, Springfield, VA 22161.

MEASUREMENT OF CP VIOLATION IN $B^0 \to \phi K^0$, AND OF BRANCHING FRACTION OF AND CP VIOLATION IN $B^0 \to f_0(980)K^0_S$

by

Paul E. Kutter

A dissertation submitted in partial fulfillment of the

requirements for the degree of

Doctor of Philosophy

(Physics)

at the

University of Wisconsin–Madison

2006

MEASUREMENT OF CP VIOLATION IN $B^0 \to \phi K^0$, AND OF BRANCHING FRACTION OF AND CP VIOLATION IN $B^0 \to f_0(980)K^0_S$

Paul E. Kutter

Under the supervision of Professor Sau Lan Wu

At the University of Wisconsin–Madison

Abstract

We measure the time-dependent *CP* asymmetry parameters in $B^0 \to K^+K^-K^0$ based on a data sample of approximately 227 million B-meson pairs recorded at the $\Upsilon(4S)$ resonance with the *BABAR* detector at the PEP-II B-meson Factory at SLAC. We reconstruct two-body B^0 decays to $\phi(1020)K^0_S$ and $\phi(1020)K^0_L$. Using a time-dependent maximum-likelihood fit, we measure $\sin 2\beta_{\rm eff}(\phi K^0) = 0.48 \pm 0.28 \pm 0.10$, and $C(\phi K^0) = 0.16 \pm 0.25 \pm 0.09$, where the first error is statistical, and the second is systematic.

We also present measurements of the *CP*-violating asymmetries in the decay $B^0 \to f_0(\to \pi^+\pi^-)K^0_S$. The results are obtained from a data sample of 209×10^6 $\Upsilon(4S) \to B\overline{B}$ decays, also collected with the *BABAR* detector at the PEP-II asymmetric-energy B Factory at SLAC. From a time-dependent maximum-likelihood fit we measure the mixing-induced *CP* violation parameter

$$S(f_0(980)K^0_S) = -\sin 2\beta_{\rm eff}(f_0(980)K^0_S) = -0.95^{+0.32}_{-0.23} \pm 0.10$$

and the direct CP violation parameter $C(f_0(980)K^0_S) = -0.24 \pm 0.31 \pm 0.15$, where the first errors are statistical and the second systematic. Finally, we present a measurement of the branching fraction of the decay $B^0 \to f_0(\to \pi^+\pi^-)K^0_S$. From a time-dependent maximum likelihood fit to a data sample of 123×10^6 $\Upsilon(4S) \to B\overline{B}$ decays we find $93.6 \pm 13.6 \pm 6.4$ signal events corresponding to a branching fraction of $\mathcal{B}(B^0 \to f_0(980)(\to \pi^+\pi^-)K^0) = (6.0 \pm 0.9 \pm 0.6 \pm 1.2) \times 10^{-6}$, where the first error is statistical, the second systematic, and the third due to model uncertainties.

Acknowledgements

There are a large number of people without whom this thesis would not have been possible. First I would like to thank my advisor, Professor Sau Lan Wu. She brought me into the field of experimental high energy physics research. These past six years she has provided me support and invaluable guidance both in my research, and in my daily life.

These measurement are the work of the collaboration of many people, in particular Matt Graham and Andreas Hoecker. Andreas, and then Matt, played the leading role in these measurements, and I have learned an invaluable amount from both of them.

There are some other people I would like to thank. Without Yibin Pan's help, I never would have been able to get started with *BABAR*. Adrian Bevan, Mousumi Datta, Katherine George, Attila Mihalyi, Steve Sekula, Jinwei Wu and Zhitang Yu were always willing to help me with any questions I had. I would also like to thank the entire *BABAR* collaboration.

Finally, I would like to thank my family for supporting me, in particular my wife, Martha, and my parents, Ed and Mary, who have encouraged my interest in science for my entire life.

Contents

List of Tables

List of Figures

Chapter 1

Introduction

1.1 Introduction to the Standard Model

We currently understand all matter to consist of members of three generations of particles, with each generation consisting of a pair of quarks, with charges of $+2/3$ and $-1/3$ that of an electron, and a lepton-neutrino pair, where the lepton has a charge equal to that of an electron, and the neutrino is neutral. The first generation is the up (u) and down (d) quarks, and the electron (e) and electron neutrino (ν_e.) The second generation is the charm (c) and strange (s) quarks, and the muon (μ) and muon neutrino (ν_μ). The third generation is the top (t) and bottom (b) quarks, and the tau (τ) and tau neutrino (ν_τ). For every kind of matter, there is also a kind of anti-matter, which is identical to its corresponding type of matter except that the values of its SU(1) properties (charge, lepton number, etc.) are opposite. Interaction between matter is governed by the gauge bosons- the massless photon (γ) and gluon(g), which mediate electromagnetic and strong nuclear interactions, and the massive W and Z particles, which mediate the weak nuclear interactions. These different interactions

have very different strengths, at least at all energies we are able to study, with the strong nuclear interaction being the strongest, and the weak nuclear interaction the weakest. Finally, the still-unobserved Higgs boson is necessary for the Higgs mechanism, which is thought to explain the origin of mass. All of this is contained within the so called Standard Model (SM). Gravity, not included in the SM, is negligable at current experimental energies. It is currently understood within the framework of general relativity, which is not easily reconciled with the quantum field theory that is used to understand the other interactions.

It is an irony of modern physics that our efforts to understand the universe on the smallest scales, in high energy particle accelerators, and on the largest scales, over the entire universe, are beginning to converge. The observation that the universe has come to consist of matter, but not antimatter, must be reconciled within the SM. This process, called bariogenesis, depends on the three Sakharov conditions [1]. First, there must be processes that violate baryon number. Second, those processes must favor the creation of baryons over antibaryons- in other words, CP violation. Finally, for reasons related to the fact that particle density is independent of time in thermal equilibrium, the universe must have been out of thermal equilibrium for some period of time. Quantitative analysis shows that there is not enough CP violation in the SM to account for the amount of baryogenesis that we have seen[2].

As we shall see, the SM allows CP violation, but makes rather stringent predictions about that violation. The *BABAR* experiment was built in part to test whether CP violation in Nature is of the type predicted by the SM. This thesis is an attempt to contribute to that end by measuring CP violation in the decays of B^0 and $\overline{B}^0$ mesons to the final states $\phi(1020)K^0$ and $f_0(980)K^0_S$.

For this thesis, we are most concerned with the weak interaction mediated by the W boson. This allows quarks or anti-quarks (hereafter referred to simply as quarks, unless otherwise noted) with a $\pm 2/3$ charge to couple to quarks with a $\mp 1/3$ charge. The decays we are most interested in tend to include mesons. A meson a quark bound to a single other anti-quark. Mesons most important to this thesis include the $\Upsilon(4S)$, the B^0, the J/Ψ, the $\phi(1020)$[1] , the $f_0(980)$[2]; the kaons: the neutral kaon K^0, the K-short K^0_S, the K-long K^0_L, and the charged kaons $K^{\pm}$; and the charged pions $\pi^{\pm}$. The properties of these mesons are in Table 1.1. The B^0, the kaons, and the charged pions all decay via the weak interaction, and are long lived on the timescale of our experiment. The resonances $\Upsilon(4S)$, the J/Ψ, the ϕ, and the f_0 decay via the strong nuclear or electromagnetic interaction. They are so short lived that on the timescale of our experiment, we consider them to have no lifetime at all.

1.2 C, P, T invariance

In this dissertation, we are concerned with CP violation in the B^0 meson system, where C represents charge conjugation, and P represents parity inversion. We also often asume that CPT invariance is not violated, where T represents time reversal. Classically, parity inversion may be understood as looking in a mirror, that is taking the position vector $\vec{r} \rightarrow -\vec{r}$. The transformation T can be seen classically as replacing time $t \rightarrow -t$. (Genuine time reversal also reverses initial and final states.) Charge conjugation has no classical analogue, and involves replacing any particle with its antiparticle. The "CPT-theorem" shows that some very general properties of quantum

[1]Throughout this document, ϕ denotes the $\phi(1020)$, and charge conjugation in decays is implied.

[2]Throughout this document, f_0 denotes the lightest, isoscalar member of the f family, $f_0(980)$.

Meson	Mass	Lifetime/Width	Quark Content	$I^G(J^{PC})$
$\Upsilon(4S)$	10.58 GeV	$20 \pm 2 \pm 4$ MeV	$b\bar{b}$	$0^-(1^{--})$
B^0	5.279 GeV	$1.54 \times 10^{-12} s$	$\bar{b}d$	$\frac{1}{2}(1^-)$
J/Ψ	3096 MeV	91 ± 3.2 MeV	$c\bar{c}$	$0^-(1^{--})$
$\phi(1020)$	1019 MeV	4.26 ± 0.05 MeV	$s\bar{s}$	$0^-(1^{--})$
$f_0(980)$	980 ± 10 MeV	$40 - 100$ MeV	†	$0^+(0^{++})$
K_S^0	498 MeV	$0.895 \times 10^{-10} s$	$s\bar{d}$	$\frac{1}{2}(0^-)$
K_L^0	498 MeV	$5.18 \times 10^{-8} s$	$s\bar{d}$	$\frac{1}{2}(0^-)$
K^+	494 MeV	$1.24 \times 10^{-8} s$	$u\bar{s}$	$\frac{1}{2}(0^-)$
π^+	140 MeV	$2.60 \times 10^{-8} s$	$u\bar{d}$	$1^-(0^-)$

Table 1.1: *Properties of different mesons that are particularly important to this dissertation[3]. Note that only uncertainties in the mass and lifetime/width that are greater than about* 1% *are shown.* †*: The quark content for the* $f_0(980)$ *is not entirely known. Significant* $s\bar{s}$ *content is likely. See Section 5.1 for more information.*

field theory lead to CPT invariance [4–8]. Since it is so difficult to conceive of a theory that violates CPT invariance, it is usually assumed to hold [8].

CP invariance is violated if we can distinguish between particles and anti-particles. The weak interaction is known to violate both C and P individually in that it couples to only left-handed fermions, or right-handed anti-fermions. This was first proposed by Lee and Yang in 1956 [9] based on observations of $K^{\pm}$ decays to 2π and 3π states with opposite parities. In 1957, Wu *et al.*[10] used ^{60}Co at $0.01°K$ inside a solenoid to show that the weak interaction violated P and C separately. In 1964, Christenson *et al.*[11] observed combined CP violation in the neutral kaon system. The existence of CP violation in the SM turns out to be intimately connected with the Cabbibo-Kobayashi-Maskawa (CKM) matrix.

1.3 The CKM Matrix and *CP* Violation

The CKM matrix represents how strongly the weak interaction couples two quarks with differing flavor. The CKM matrix is show in Table 1.2. Note that there are no tree-level neutral flavor-changing currents in the Standard Model. As we shall see, CP violation can exist in the standard model only if the CKM matrix has a non-reducible phase. An arbitrary $N \times N$ matrix has N^2 moduli and N^2 phases. However, the CKM matrix is unitary, so this leaves only $\frac{1}{2}N(N+1)$ phases left. We can remove still more phases because to determine what is observable, we only take the modulus of a matrix element, *e.g.*$| < \phi_j|H|\phi_i > |$, where H is the Hamiltonian, and $|\phi >$ is a state vector, so that we can change the phase of any vector $|\phi >$ without changing the physical predictions made by our theory. Since we have $2N$ quarks, we would be able to change $2N$ phases, except that changing all the quark phases is equivalent to changing $2N-1$ quark phases, plus multiplying the entire CKM phase by a single global phase. So we can remove an additional $2N-1$ phases from individual elements of the CKM matrix. For N generations of quarks we have $\frac{1}{2}N(N+1)-(2N-1)$ irreducible phases, which means that for $N=3$ there is exactly one irreducible phase.

$$\begin{pmatrix} V_{ud} & V_{us} & V_{ub} \\ V_{cd} & V_{cs} & V_{cb} \\ V_{td} & V_{ts} & V_{tb} \end{pmatrix}$$

Table 1.2: The CKM matrix, with each element identified using the standard notation.

In Table 1.3 we parameterize the CKM matrix to make explicit its unitary nature, and that it has a single irreducible phase. Current best measurements of the moduli

of the different CKM elements are shown in Table 1.4. We can use the so-called Wolfenstein parameterization to incorporate the measured values of the CKM matrix into its parameterization. We expand it in terms of $\lambda \equiv S_{12} = 0.22$. We also define $S_{23} \equiv A\lambda^2$, $S_{13}e^{-i\delta} \equiv A\lambda^3(\rho - i\eta)$, where A, ρ and η are of order 1. We follow convention and refer to (λ, A, ρ, η) as the Wolfenstein parameters. The CKM matrix is parameterized this way in Table 1.5. Immediately, we can see that the different CKM matrix elements have very different sizes, of order 1 for quarks within the same generation, order λ for quarks from the first and second generation, λ^2 for quarks from the second and third generations, and λ^3 for quarks from the first and third generation. This difference in sizes of the different CKM matrix elements will be seen to be very important for finding modes to measure experimentally that can be easily compared to theoretical predictions.

$$\begin{pmatrix} C_{12}C_{13} & S_{12}C_{13} & S_{13}e^{-i\delta} \\ -S_{12}C_{23} - C_{12}S_{23}S_{13}e^{i\delta} & C_{12}C_{23} - S_{12}S_{23}S_{13}e^{i\delta} & S_{23}C_{13} \\ S_{12}C_{23} - C_{12}C_{23}S13e^{i\delta} & -C_{12}S_{23} - S_{12}C_{23}S_{13}e^{i\delta} & C_{23}C_{13} \end{pmatrix}$$

Table 1.3: *The CKM matrix parameterized to make explicit its unitary nature and single irreducible phase.* $C_{ij} = \cos(\theta_{ij})$, $S_{ij} = \sin(\theta_{ij})$, δ *is the irreducible phase.*

$$\begin{pmatrix} 0.97377 \pm 0.00027 & 0.2257 \pm 0.0021 & (4.31 \pm 0.3) \times 10^{-3} \\ 0.230 \pm 0.011 & 0.957 \pm 0.017 & (41.6 \pm 0.6) \times 10^{-3} \\ (7.4 \pm 0.8) \times 10^{-3} & (40.6 \pm 2.7) \times 10^{-3} & > 0.78 \end{pmatrix}$$

Table 1.4: *Current best estimates of the moduli of the CKM matrix elements, as compiled by [3].*

$$\begin{pmatrix} 1-\frac{\lambda^2}{2} & \lambda & A\lambda^3(\rho-i\eta) \\ -\lambda & 1-\frac{\lambda^2}{2} & A\lambda^2 \\ A\lambda^3(1-\rho-i\eta) & -A\lambda^2 & 1 \end{pmatrix}$$

Table 1.5: *The Wolfenstein parameterization of the CKM matrix.*

The unitary nature of the CKM matrix allows us to write the following 3 relations:

$$V_{ud}V_{us}^{\star} + V_{cd}V_{cs}^{\star} + V_{td}V_{ts}^{\star} = 0 \quad (1.1)$$

$$V_{us}V_{ub}^{\star} + V_{ub}V_{cb}^{\star} + V_{ts}V_{tb}^{\star} = 0 \quad (1.2)$$

$$V_{ud}V_{ub}^{\star} + V_{cd}V_{cb}^{\star} + V_{td}V_{tb}^{\star} = 0 \quad (1.3)$$

Since the three terms of each equation can be seen as three vectors in the complex plane that must add to 0, they can be used to construct three triangles. The third equation in particular can be used to construct a triangle that is important enough to be referred to simply as "the Unitarity Triangle." It is shown in Figure 1.1. By measuring the three angles of the triangle, we can overconstrain it and test the consistency of the Standard Model. This thesis is concerned with measurements of the angle β:

$$\beta = \arg\left[-\frac{V_{cd}V_{cb}^{*}}{V_{td}V_{tb}^{*}}\right] \quad (1.4)$$

In particular, we look to measure β from $e^+e^- \rightarrow \Upsilon(4S) \rightarrow B^0\overline{B}^0$ where $B^0 \rightarrow f_0K_s^0$ and $B^0 \rightarrow \phi K^0$.

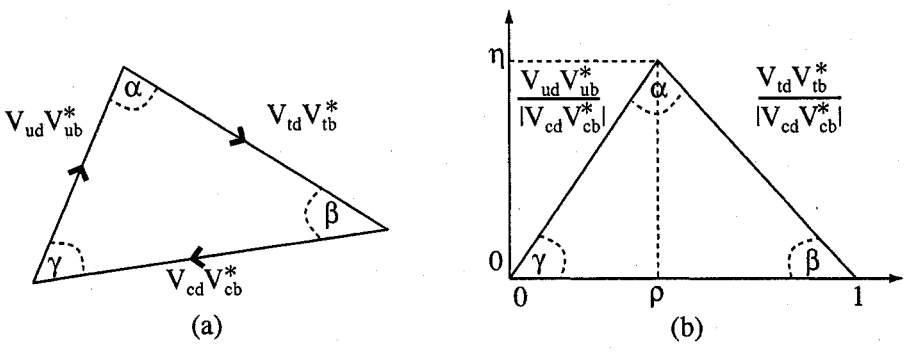

Fig. 1.1.— *The Unitarity Triangle (a), and the rescaled Unitarity Triangle (b). We rescale the Unitarity Triangle by choosing a phase convention such that $V_{cd}V_{cb}^*$ is real, and dividing the length of all sides by $|V_{cd}V_{cb}^*|$ so that one leg has length 1 and is on the real axis.*

1.4 The B^0 Meson and $B^0\overline{B}^0$ Mixing

The flavor eigenstates of the B_d meson are not the same as the mass eigenstates [3]. This means that the flavor content of a particular neutral B_d meson will fluctuate between that of a B^0, $\bar{b}d$, and a $\overline{B}^0$, $b\bar{d}$ [4]. Given a B_d meson, we want to describe the time-dependent evolution of its state $a|B^0> + b|\overline{B}^0>$. The Schrodinger equation tells us that:

$$i\frac{d}{dt}\begin{pmatrix} a \\ b \end{pmatrix} = H\begin{pmatrix} a \\ b \end{pmatrix} = (M - \frac{i}{2}\Gamma)\begin{pmatrix} a \\ b \end{pmatrix}$$

where M and Γ are both hermitian. If we diagonalize this equation, we find two solutions which in the neutral B_d correspond to light and heavy mass eigenstates $|B_L>$ and $|B_H>$ with masses M_L and M_H:

$$|B_L> \;=\; p|B^0> + q|\overline{B}^0> \tag{1.5}$$

[3]This discussion closely follows [12] and [8], where more information may be found.

[4]The convention is that the B^0 is the isospin partner of the B^+, and so has a $\bar{b}$ quark.

$$|B_H> \;=\; p|B^0> - q|\overline{B}^0> \tag{1.6}$$

where $p^2 + q^2 = 1$. If we define $\Delta m_B = M_H - M_L$ and the difference in lifetime $\Delta\Gamma_B = \Gamma_H - \Gamma_L$, then we find:

$$\begin{aligned} \frac{q}{p} &= -\frac{2(M_{12}^* - \frac{i}{2}\Gamma_{12}^*)}{\Delta m_B - \frac{i}{2}\Delta\Gamma_B} \\ (\Delta m_B)^2 - \frac{1}{4}(\Delta\Gamma_B)^2 &= 4(|M_{12}|^2 - \frac{1}{4}|\Gamma_{12}|^2) \\ \Delta m_B \Delta\Gamma_B &= 4Re\,(M_{12}\Gamma_{12}^*) \end{aligned}$$

The difference in width, $\Delta\Gamma$, is expected to be small. It is produced by decay channels common to both B^0 and $\overline{B}^0$, and the branching fractions of these channels is at or below 10^{-3}. Since the different channels contribute with differing signs, one does not expect their sum to greatly exceed their individual contributions, so in a fairly model independent way, we can expect[12]:

$$\Delta\Gamma_B/\Gamma_B = \mathcal{O}(10^{-2})$$

The value of Δm_B has been measured[3]:

$$x_d \equiv \Delta m_B/\Gamma_B = 0.188 \pm 0.003$$

Then we know that: $\Delta\Gamma << \Delta m$. Therefore we can write:

$$\begin{aligned} \Delta m_B &= 2|M_{12}| \\ \Delta\Gamma_B &= \frac{2Re(M_{12}\Gamma_{12}^*)}{|M_{12}|} \\ \frac{q}{p} &= \frac{-|M_{12}|}{M_{12}} \end{aligned}$$

We can now write expressions for the wave function of a B_d meson:

$$|B_d> \;=\; a_H(t)|B_H> + a_L(t)|B_L> \tag{1.7}$$

$$\;=\; a_H(t=0)e^{-iM_H t}e^{-\frac{1}{2}\Gamma_H t}|B_H> + a_L(t=0)e^{-iM_L t}e^{-\frac{1}{2}\Gamma_L t}|B_L> \tag{1.8}$$

where $a_H(t)$ and $a_L(t)$ represent the $|B_H>$ and $|B_L>$ components of our $|B_d>$ as a function of time. It is more convenient, though, to express $|B_d>$ as a function of the flavor eigenstates $|B^0>$ and $|\overline{B}^0>$. Suppose that at time $t = 0$ $|B_d>=|B^0>$ or $|B_d>=|\overline{B}^0>$. We need to express the time dependent wave function. If at $t = 0$, $|B_d>=|B^0>$ then we call the time dependent wave function $|B^0_{\rm phys}(t)>$; if $|B_d>=|\overline{B}^0>$, we call the time dependent wave function $|\overline{B}^0_{\rm phys}(t)>$. The we can use equations 1.5, 1.6, and 1.8 to find:

$$\begin{aligned} |B^0_{\rm phys}(t)> &= g_+(t)|B^0> + \frac{q}{p} g_-(t)|\overline{B}^0> \\ |\overline{B}^0_{\rm phys}(t)> &= \frac{p}{q} g_-(t)|B^0> + g_+(t)|\overline{B}^0> \end{aligned}$$

where we define:

$$\begin{aligned} g_+(t) &= e^{-imt} e^{-\Gamma\frac{t}{2}} \cos(\Delta m \frac{t}{2}) \\ g_-(t) &= e^{-imt} e^{-\Gamma\frac{t}{2}} i \sin(\Delta m \frac{t}{2}) \end{aligned}$$

where $m = \frac{M_L + M_H}{2}$ and $\Gamma = \frac{\Gamma_L + \Gamma_H}{2}$.

At *BABAR*, a e^+e^- pair is collided at the $\Upsilon(4S)$ resonance mass so that when a pair of neutral B_d mesons are produced, they are in a coherent $L = 1$ state. One way to think of this is that we have two neutral B_d mesons that each evolve in time as if an independent B_d meson, but in such a way that there is always exactly one B^0 and one $\overline{B}^0$, at least until one of them decays. In the center-of-mass (CM) frame, the two mesons are produced back-to-back. We can distinguish each one by the its decay angle, and by the time since it was produced. Then we can write the state function of our two meson system as a function of the time-since-production of the forward and

backward mesons, t_f and t_b:

$$\begin{aligned} S(t_f,t_b) &= \frac{1}{\sqrt{2}}\Big\{|B^0_{\rm phys}(t_f,\theta,\phi)>|\overline{B}^0_{\rm phys}(t_b,\pi-\theta,\phi+\pi)> \\ &- |\overline{B}^0_{\rm phys}(t_f,\theta,\phi)>|B^0_{\rm phys}(t_b,\pi-\theta,\phi+\pi)>\Big\}\sin\theta \\ &= \frac{1}{\sqrt{2}}e^{-(\frac{\Gamma}{2}+im)(t_f+t_b)}\left\{\cos\left[\Delta m\frac{(t_f-t_b)}{2}\right]\left(|B^0_f,\overline{B}^0_b>\right.\right. \\ &\quad -|\overline{B}^0_f,B^0_b>\Big) - i\sin\left(\Delta m\frac{t_f-t_b}{2}\right)\left(\frac{p}{q}|B^0_f,\overline{B}^0_b>\right. \\ &\quad \left.\left.-\frac{q}{p}|\overline{B}^0_f,B^0_b>\right)\right\}\sin\theta_f \end{aligned}$$

Here, θ_f is the angle that the forward-moving B_d meson makes with the path of the e^+, $|B^0_f,\overline{B}^0_b>$ denotes the B^0 component of the forward moving B_d meson and the $\overline{B}^0$ component of the backward moving B_d meson, and $|\overline{B}^0_f,B^0_b>$ denotes the $\overline{B}^0$ component of the forward moving B_d meson and the B^0 component of the backward moving B_d meson. Notice that so long as neither meson has decayed, $t_f=t_b$, and we have exactly one B^0 meson and one $\overline{B}^0$ meson. As soon as one meson decays, then in general $t_f\neq t_b$ and we might have both a B^0 and a $\overline{B}^0$ meson. We can use this expression for the state to calculate the amplitude for the two mesons to decay to the final states f_1 and f_2 at time t_1 and t_2:

$$\begin{aligned} A(t_1,t_2) &= \frac{1}{\sqrt{2}}e^{-(\frac{\Gamma}{2}+im)(t_f+t_b)}\zeta(t_1,t_2)\left\{\cos\left[\Delta m\frac{t_1-t_2}{2}\right]\right. \\ &\quad \Big(A_1\bar{A}_2-\bar{A}_1A_2\Big) - i\sin\left[\Delta m\frac{t_1-t_2}{2}\right]\left(\frac{p}{q}A_1A_2\right. \\ &\quad \left.\left.-\frac{q}{p}\bar{A}_1\bar{A}_2\right)\right\}\sin\theta_1 \end{aligned}$$

Here the subscript indexes the two B_d mesons, A_i is the amplitude of a transition from B^0 to f_1, and $\bar{A}$ is the amplitude of a transition from $\overline{B}^0$ to f_2, and t_i is the time that the $i^{\rm th}$ meson decays. Now suppose that we look for decays such that one B_d meson

decays to a state that determines its flavor, and the other meson decays to some CP eigenstate, $f_{\rm cp}$. Then $A_1 = \bar{A}_1 \equiv A_{f_{\rm cp}} = \eta_{f_{\rm cp}} A_{\bar{f}_{\rm cp}}$, and $A_2 = 0, \bar{A}_2 \equiv \bar{A}_{\rm tag}$ or $\bar{A}_2 = 0, A_2 \equiv A_{\rm tag}$. It is now straight-forward to calculate the time-dependent rate. If $\bar{A}_2 = \bar{A}_{\rm tag}$, the rate is:

$$\begin{aligned} R &= Ce^{-\Gamma(t_{\rm tag}+t_{f_{\rm cp}})}|\bar{A}_{\rm tag}|^2|A_{f_{\rm cp}}|^2\left\{1+|\lambda_{f_{\rm cp}}|^2\right. \\ &\quad +(1-|\lambda_{f_{\rm cp}}|^2)\cos\left[\Delta m(t_{f_{\rm cp}}-t_{\rm tag})\right] \\ &\quad \left.-2Im(\lambda_{f_{\rm cp}})\sin\left[\Delta m(t_{f_{\rm cp}}-t_{\rm tag})\right]\right\} \end{aligned}$$

If $A_2 = A_{\rm tag}$ then we must switch the sign of the sine term. We define

$$\begin{aligned} \lambda_{f_{\rm cp}} &= \frac{q}{p}\frac{\bar{A}_{f_{\rm cp}}}{A_{f_{\rm cp}}} \\ &= \eta_{f_{\rm cp}}\frac{q}{p}\frac{\bar{A}_{\bar{f}_{\rm cp}}}{A_{f_{\rm cp}}} \end{aligned}$$

We can now calculate the time-dependent decay asymmetry $a_{f_{\rm cp}}$:

$$\begin{aligned} a_{f_{\rm cp}} &= \frac{R(f_{\rm cp},{\rm tag}=B^0)-R(f_{\rm cp},{\rm tag}=\overline{B}^0)}{R(f_{\rm cp},{\rm tag}=B^0)+R(f_{\rm cp},{\rm tag}=\overline{B}^0)} \\ &= \frac{2Im(\lambda_{f_{\rm cp}})\sin(\Delta m\Delta t)-(1-|\lambda_{f_{\rm cp}}|^2)\cos(\Delta m\Delta t)}{1+|\lambda_{f_{\rm cp}}|^2} \end{aligned}$$

where Δt is the time between the two B decays. For convenience, we can rewrite this as using the parameters S and C:

$$a_{f_{\rm cp}} = S\sin(\Delta m\Delta t) - C\cos(\Delta m\Delta t) \tag{1.9}$$

where $C = \frac{1-|\lambda_{f_{\rm cp}}|^2}{1+|\lambda_{f_{\rm cp}}|^2}$ and $S = \frac{2Im(\lambda_{f_{\rm cp}})}{1+|\lambda_{f_{\rm cp}}|^2}$. If CP is conserved, then $a_{f_{\rm cp}} = 0$.

As mentioned earlier, many phase changes are not physically significant. In general, we can change the following phases without affecting the physical predictions

of our theory:

$$\begin{aligned} |f_{\rm cp}> &\rightarrow e^{i\gamma_f}|f_{\rm cp}> \\ |B^0> &\rightarrow e^{i\gamma}|B^0> \\ |\overline{B}^0> &\rightarrow e^{i\bar{\gamma}}|\overline{B}^0> \end{aligned}$$

Then:

$$\begin{aligned} A_{f\rm cp} &\rightarrow e^{i(\gamma-\gamma_f)}A_{f\rm cp} \\ \bar{A}_{f\rm cp} &\rightarrow e^{i(\bar{\gamma}-\gamma_f)}\bar{A}_{f\rm cp} \\ \frac{q}{p} &\rightarrow e^{i(\gamma-\bar{\gamma})}\frac{q}{p} \end{aligned}$$

so: $\left|\frac{q}{p}\right|$, $\left|A_{f\rm cp}\right|$, $\left|\bar{A}_{f\rm cp}\right|$ and $\lambda_{f\rm cp}$ are all phase invariant, allowing them to be physically significant (as can be seen by the fact that they all affect the value of $a_{f\rm cp}$.)

For CP to be a good symmetry, $CP^2 = 1$. (In fact, in general we only need to require that CP^2 be equal to any number with a modulus of unity, and for convenience we choose this number to be unity.) Let $CP|B^0>= e^{i\zeta}|\overline{B}^0>$ and $CP|\overline{B}^0>= e^{-i\zeta}|B^0>$. Then CP is conserved only if the mass eigenstates formed by the mixing $|B^0>$ and $|\overline{B}^0>$ states are also CP eigenstates, that is if $\frac{q}{p} = \pm e^{i\zeta}$ or $\left|\frac{q}{p}\right| = \pm 1$. If $\left|\frac{q}{p}\right| \neq \pm 1$ then this is called CP violation in mixing. It is expected that $1 - \left|\frac{q}{p}\right| \sim 10^{-3}$[12].

Similarly, if CP is conserved, then

$$\begin{aligned} A_{f\rm cp} &= e^{i\zeta}\bar{A}_{f\rm cp} \\ &= e^{i\zeta}\eta_{f\rm cp}\bar{A}_{\bar{f}\rm cp} \end{aligned}$$

so $\left|A_{f\rm cp}\right| = \left|\bar{A}_{\bar{f}\rm cp}\right|$. If $\left|A_{f\rm cp}\right| \neq \left|\bar{A}_{\bar{f}\rm cp}\right|$ then this is called "direct CP violation", or "CP violation in decay." We can see what is required for direct CP violation by

writing

$$\left|\frac{\bar{A}_{\bar{f}_{\rm cp}}}{A_{f_{\rm cp}}}\right| = \left|\frac{\sum_i A_i e^{i(\delta_i-\phi_i)}}{\sum_i A_i e^{i(\delta_i+\phi_i)}}\right|$$

where δ_i is the $i^{\rm th}$ "strong phase" (a phase which does not have its sign changed by a CP transformation), and ϕ_i is the $i^{\rm th}$ "weak phase" (a phase which does have its sign changed by a CP transformation.) This sum does not equal 1 only if at least two terms with weak phases also acquire strong phases:

$$|A|^2 - |\bar{A}|^2 = -2\sum A_i A_j \sin(\phi_i - \phi_j)\sin(\delta_i - \delta_j)$$

Finally, if CP is conserved,

$$\frac{q}{p}\frac{\bar{A}_{f_{\rm cp}}}{A_{f_{\rm cp}}} = \pm e^{i\zeta}$$

If $\left|\lambda_{f_{\rm cp}}\right| = \pm 1$ but $\lambda_{f_{\rm cp}}$ has a non-zero phase, then this is called "CP violation in the interefence between mixing and decay." In modes we are most concerned with in this thesis, namely $B^0 \to \phi K^0$ and $B^0 \to f_0 K^0_s$, to a good approximation this is the only type of CP violation present. Then $a_{\rm cp}(\Delta t) = -Im(\lambda_{f_{\rm cp}})\sin\Delta m\Delta t$. We can relate the phase of $\lambda_{f_{\rm cp}}$ to the irreducible phase of the CKM matrix.

Relating any measurement of $a_{\rm cp}(\Delta t)$ to SM predictions is difficult. Typically, a low-energy effective Hamiltonian is used. It is constructed using an operator production expansion (OPE) to separate the short- and long-distance contributions to the decay. The effective Hamiltonian is:

$$\mathcal{H}_{\rm eff} = \frac{G_F}{\sqrt{2}}\sum_{p=u,c}\lambda_p^{(D)}\left(C_1 Q_1^p + C_2 Q_2^p + \sum_{i=3}^{10} C_i Q_i + C_{7\gamma}Q_{7\gamma} + C_{8g}Q_{8g}\right) + \text{h.c.}$$

where $\lambda_p^{(D)} = V_{pb}V_{pD}^*$, D represents a d or s quark depending on the mode considered, $p = u, c, t$, $Q_{1,2}^p$ are the left-handed current-current operators arising from W-boson exchange, $Q_{3,\ldots,6}$ and $Q_{7,\ldots,10}$ are QCD and electroweak penguin operators, and

$Q_{7\gamma}$ and Q_{8g} are the electromagnetic and chromomagnetic dipole operators [13]. The short-distance effects can be perturbatively calculated, and are formally grouped into Wilson coefficients C_i. The long-distance effects are grouped into the non-perturbative hadronic matrix elements. Traditionally, these have been calculated using so called "naive factorization", which separates four-quark operators into two two-quark operators. However, this ignores final state interactions (FSI) which in many cases are important for predicting direct CP asymmetries. QCD factorization allows one to correct for this to order $\mathcal{O}(\Lambda_{\rm QCD}/m_b)$ by writing, for example:

$$< \pi\pi|Q|\overline{B}^0 >=< \pi|j_1|\overline{B}^0 >< \pi|j_2|0 > \cdot \left[1 + \sum r_n \alpha_s^n + \mathcal{O}(\Lambda_{\rm QCD}/m_b)\right]$$

where $j_{1,2}$ are bilinear quark currents, and m_b is the mass of the b quark[14].

1.5 Measuring $\sin 2\beta$

1.5.1 Measuring $\sin 2\beta$ using Charmonium

The decay $B^0 \to J/\psi K_S^0$ is dominated by a single tree diagram, shown in Figure 1.3. Additionally, the dominant penguin contribution has the same weak phase as the tree diagram. (The decay $K_S^0 \to \pi^+\pi^-$ is dominated by the tree diagram shown in Figure 1.4.) Since (to $O(\lambda^2)$) there is a single weak phase, we can calculate the phase of $\bar{A}_{J/\psi K_S^0}/A_{J/\psi K_S^0}$ without having to calculate any non-perturbative hadronic matrix elements. Three factors affect the phase of $\lambda_{J/\psi}$: $\frac{q}{p}$ from $B^0 - \overline{B}^0$-mixing, given by M_{12} (see equation 1.7); $\frac{\bar{A}_{J/\psi \bar{K}^0}}{A_{J/\psi K^0}}$; and finally, $K^0\bar{K}^0$ mixing:

$$\lambda_{J/\psi K_S^0} = \left(\frac{V_{tb}^* V_{td}}{V_{tb} V_{td}^*}\right)\left(\frac{V_{cs}^* V_{cb}}{V_{cs} V_{cb}^*}\right)\left(\frac{V_{cd}^* V_{cs}}{V_{cd} V_{cs}^*}\right)$$

The factor of $\left(\frac{V_{tb}^* V_{td}}{V_{tb} V_{td}^*}\right)$ comes from the $B^0 - \overline{B}^0$ mixing, and is calculated by the box diagrams in Figure 1.2. Mixing from top quark exchange is enhanced due to the larger t-quark mass. The factor of $\left(\frac{V_{cs}^* V_{cb}}{V_{cs} V_{cb}^*}\right)$ is due to the tree diagrams in Figure 1.3. Finally, the factor of $\left(\frac{V_{cd}^* V_{cs}}{V_{cd} V_{cs}^*}\right)$ is due to $K^0 - \bar{K}^0$ mixing. Then:

$$a_{J/\psi K_S^0} = \sin(2\beta)\sin(\Delta m \Delta t)$$

To order $O(\lambda^2)$ we are able to relate the time-dependent asymmetry of $B^0 \to J/\psi K_S^0$, and of other charmonium modes as well, to the CKM angle β, independent of any hadronic uncertainties. These modes are also very clean experimentally. B-factories have measured $\sin 2\beta$ to within about 5%. (*cf.*Table 1.6). The latest *BABAR* measurement of $a_{f_{\rm CP}}$ for charmonium is show in Figure 1.5.

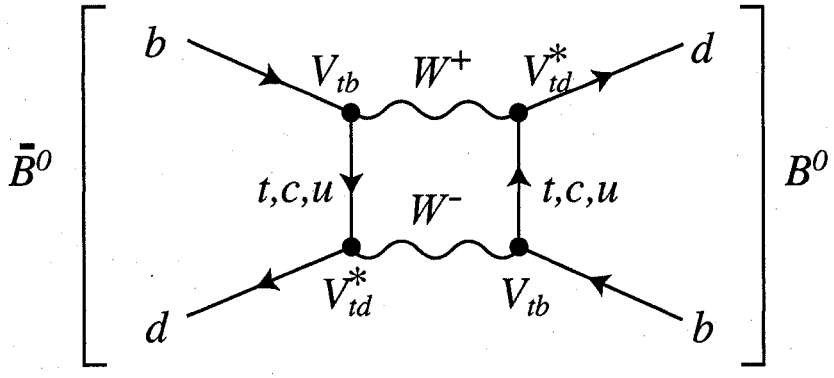

Fig. 1.2.— *Box diagrams like this are responsible for $B^0/\overline{B}^0$ mixing in the SM.*

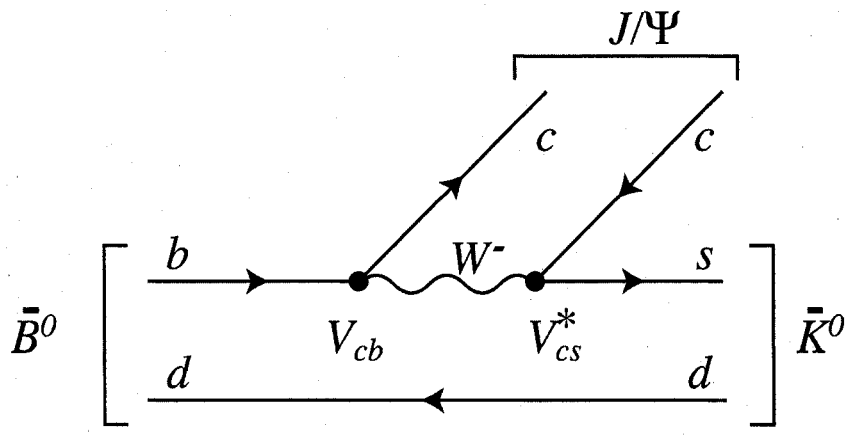

Fig. 1.3.— *The dominant tree contribution to* $B^0 \to J/\psi K^0_s$ *decays.*

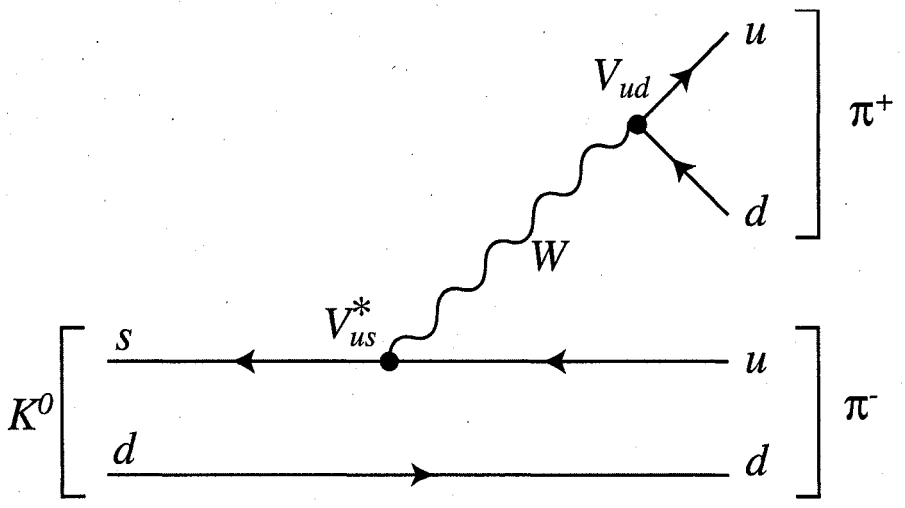

Fig. 1.4.— *The dominant tree contribution to* $K^0_s \to \pi^+\pi^-$ *decays.*

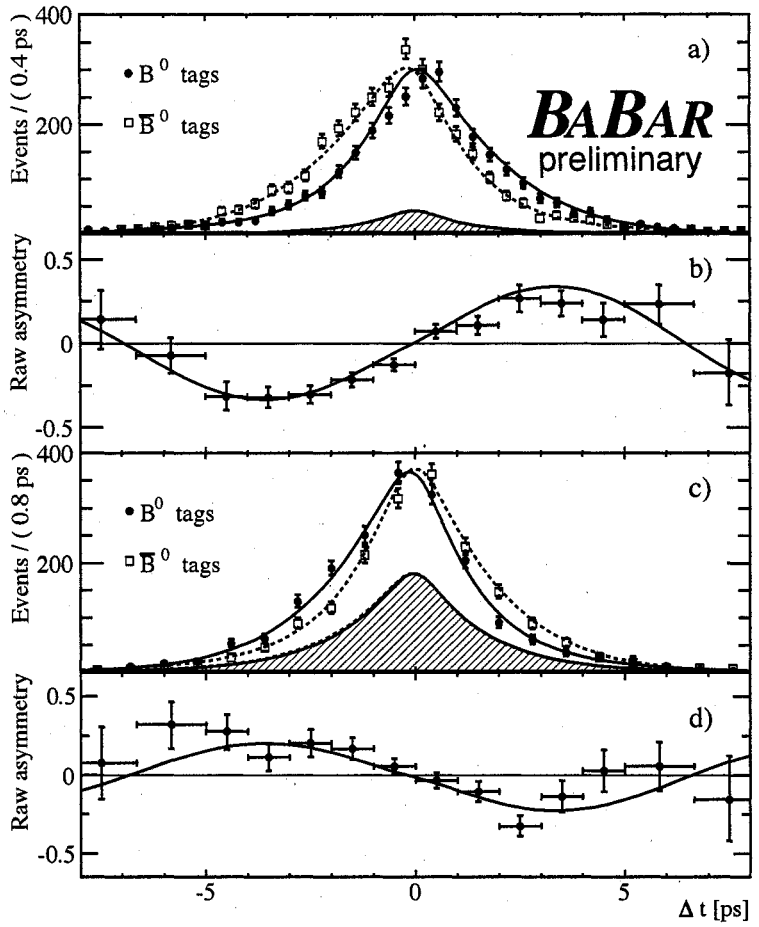

Fig. 1.5.— *a) Number of $\eta_f = -1$ candidates ($J/\psi K^0_S$, $\psi(2S)K^0_S$, $\chi_{cl}K^0_S$ and $\eta_c K^0_S$.) in the signal region with a B^0 tag (N_{B^0}) and with a $\overline{B}^0$ tag ($N_{\overline{B}^0}$), and b) the raw asymmetry $(N_{B^0} - N_{\overline{B}^0})/(N_{B^0} + N_{\overline{B}^0})$, as a function of Δt. Figures c) and d) are the corresponding distributions for the $\eta_f = +1$ mode $J/\psi K^0_L$. The solid (dashed) curves represent the fit projections in Δt for B^0 ($\overline{B}^0$) tags. The shaded regions represent the estimated background contributions [15].*

1.5.2 Measuring $\sin 2\beta$ using $b \to s\bar{s}s$ gluonic penguins

Diagrams like those shown in Figure 1.6 are important to a class of decays that includes $B^0 \to \phi K^0$ and $B^0 \to f_0 K^0$. If we assume that the diagram in Figure 1.6 is the only contributing decay, then we can write the decay amplitude as a sum of the contribution from each of the three diagrams formed by the three separate virtual quarks in the loop:

$$A = V_{cs}V_{cs}^*(P^c) + V_{ts}V_{ts}^*(P^t) + V_{us}V_{us}^*(P^u)$$

where P^q represents the contribution from the diagram with a virtual q-quark. We can rewrite this using the unitarity condition in equation 1.3:

$$A = V_{cs}V_{cs}^*(P^c - P^t) + V_{us}V_{us}^*(P^u - P^t)$$

The second term is CKM suppressed with respect to the first by a factor of the Wolfenstein parameter λ^2. Then the parameter $\lambda_{f_{\rm CP}}$ for these three diagrams, which we call $\lambda_{b\to s\bar{s}s}$, is:

$$\lambda_{b\to s\bar{s}s} = \left(\frac{V_{tb}^*V_{td}}{V_{tb}V_{td}^*}\right)\left(\frac{V_{cb}^*V_{cs}(P^c - P^t) + V_{ub}^*V_{us}(P^u - P^t)}{V_{cb}V_{cs}^*(P^c - P^t) + V_{ub}V_{us}^*(P^u - P^t)}\right)\left(\frac{V_{cd}^*V_{cs}}{V_{cd}V_{cs}^*}\right) \quad (1.10)$$

$$\approx \left(\frac{V_{tb}^*V_{td}}{V_{tb}V_{td}^*}\right)\left(\frac{V_{cb}^*V_{cs}}{V_{cb}V_{cs}^*}\right)\left(\frac{V_{cd}^*V_{cs}}{V_{cd}V_{cs}^*}\right) \quad (1.11)$$

So for a particular final state f, so long as we can neglect diagrams with a weak phase different than $\left(\frac{V_{cb}^*V_{cs}}{V_{cb}V_{cs}^*}\right)$, the time-dependent asymmetry will be equal in value to a number close to $\sin 2\beta$ which we call $\sin 2\beta^f_{\rm eff}$:

$$a_f(\Delta t) = -\eta_f \sin(2\beta^f_{\rm eff})\sin(\Delta m \Delta t) = -\eta_f \sin(2\beta)\sin(\Delta m \Delta t)$$

In general, how close $\beta^f_{\rm eff}$ is to β will depend on the final state f. Even if the diagram shown in Figure 1.6 is the only contributing diagram, in general the relative strengths of $P^c - P^t$ and $P^u - P^t$ will depend on hadronic matrix elements. Additionally, different modes have contributing diagrams in addition to the gluonic penguin shown in Figure 1.6. For this thesis, we measure *CP* violation in $B^0 \to \phi K^0$ and $B^0 \to f_0 K^0_S$. Since both these modes are penguin dominated, we expect them to generically be more susceptible to new physics from the weak and higher scales[16,17]. So, a lack of agreement between $\sin 2\beta^{\phi K^0}_{\rm eff}$ or $\sin 2\beta^{f_0 K^0}_{\rm eff}$ and $\sin 2\beta$ as measured by charmonium could indicate physics beyond the SM. Possible sources of new physics include tree-level flavor-changing neutral currents (FCNC) or penguin diagrams containing undiscovered bosons in the loop[17]. (*cf.* Figure 1.7.)

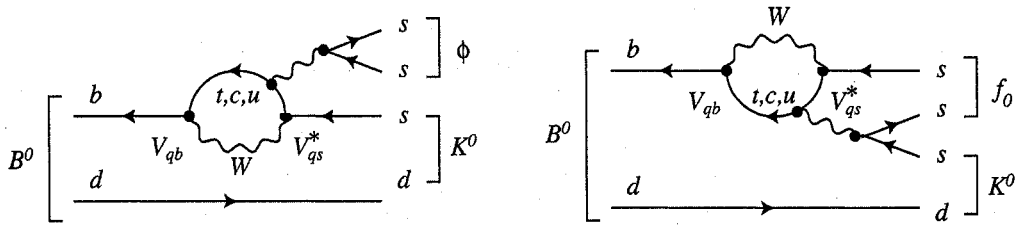

Fig. 1.6.— *The $b \to s\bar{s}s$ gluonic penguin contribution to $B^0 \to \phi K^0$ (left) and $B^0 \to f_0 K^0$.*

The decay $B^0 \to \phi K^0$ is among the cleanest of these $b \to s\bar{s}s$ (and, more generally, $b \to s\bar{q}q$) gluonic penguin modes, both experimentally and theoretically. Theoretically, next-to-leading order factorization calculations predict the difference $|\beta - \beta_{\rm eff}|$ to be only a few degrees ($\sin 2\beta_{\rm eff} - \sin 2\beta = 0.02 \pm 0.01$) [18]. Experimentally, the narrowness of the ϕ resonance, and the fact that all the particles in the final state are charged, makes the channel extremely clean. Finally, the branching fraction makes

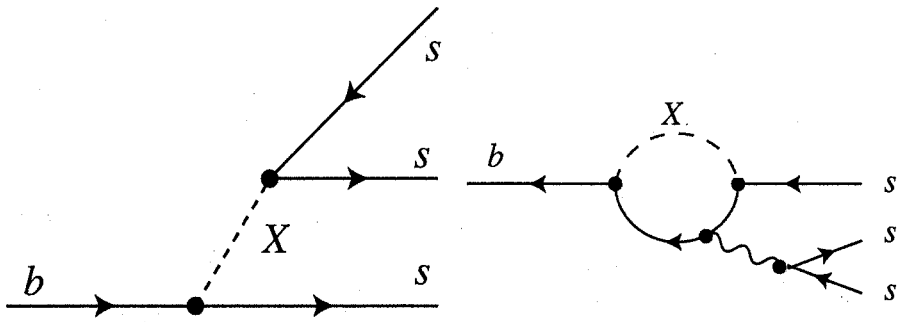

Fig. 1.7.— *Possible new physics contributions to the* $b \to s\bar{s}s$ *gluonic penguin modes: a tree-level neutral flavor-changing current (left), and a penguin diagram with a still-undiscovered bosons. For the tree-level diagram, the mass of X is expected to be roughly that of the Z boson. For the penguin diagram, the mass of X may be anywhere from approximately* $400\,\mathrm{GeV}/c^2$ *to* $2-3\,\mathrm{TeV}/c^2$ *[17].*

the mode accessible: $BR(B^0 \to \phi K^0) = (8.6^{+1.3}_{-1.1}) \times 10^{-6}$[3].

The theoretical study of *CP* violation in $B^0 \to f_0 K^0_s$ is complicated by the structure of the scalar meson f_0, which has been discussed for decades but is still obscure. There were attempts to interpret it as $K\overline{K}$ molecular states[19], four-quark states[20] and normal $q\bar{q}$ states[21]. However, recent studies of $\phi \to \gamma f_0$ ($f_0 \to \gamma\gamma$)[22, 23] and $D^+_s \to f_0\pi^+$[24] decays favor the $q\bar{q}$ state models. In this interpretation the flavor content of the f_0 is given by $f_0 = \cos(\phi_s)s\bar{s} + \sin(\phi_s)n\bar{n}$, with $n\bar{n} = (u\bar{u}+d\bar{d})/\sqrt{2}$. A mixing phase of $\phi_s = -48° \pm 6°$ has been experimentally determined from $\phi \to \gamma f_0$ decays[23].

Measuring the *CP* violation in $B \to f_0 K$, and also its branching fractions to compare with theoretical predictions using various QCD calculation approaches based on assumptions of the f_0 structure, compliment each other in the sense that a good

understanding of the hadron and a reliable approach to calculate strong interaction are necessary for the precise determination of the CKM phases. In particular, the measurement of direct *CP* violation effectively tests the hypothesis of penguin dominance.

There is a possible tree contribution to $f_0 K_S^0$ via $b \to u\bar{u}s$, shown in Fig. 1.8(a), but this is both doubly Cabibbo-suppressed (with respect to the leading penguin diagram) and color-suppressed. If the assumption is true that the f_0 state has a sizable content of $s\bar{s}$, then the process $f_0 K_S^0$ would be dominated by the penguin process, $b \to s\bar{s}s$ (*cf.* Fig. 1.8(b)).

BABAR and Belle have observed the decay $B^+ \to f_0 K^+$ and consistently measured the product branching fraction $\mathcal{B}(B^+ \to f_0(\to \pi^+\pi^-)K^+) = (9.2 \pm 1.2^{+2.1}_{-2.6} \times 10^{-6}$[25] and $\mathcal{B}(B^+ \to f_0(\to \pi^+\pi^-)K^+) = (9.6^{+2.5}_{-2.3}{}^{+1.5}_{-1.5}{}^{+3.4}_{-0.8}) \times 10^{-6}$[26], respectively, resulting in approximately $\mathcal{B}(B^+ \to f_0 K^+) \sim 20 \times 10^{-6}$. We can reasonably expect that $\mathcal{B}(B^0 \to f_0 K^0)$ has a value of similar magnitude. Additionally, Belle has recently used a (not time-dependent) full dalitz analysis to measure the the branching fraction of $B^0 \to f_0(\to \pi^+\pi^-)K_S^0$ to be $7.6 \pm 1.7 \pm 0.7^{+0.5}_{-0.7}$ [27].

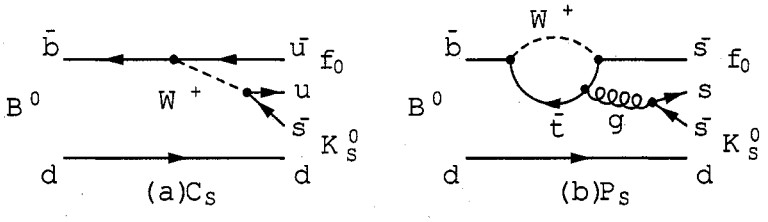

Fig. 1.8.— *The color-suppressed tree (a) and dominant gluonic penguin (b) are diagrams that could contribute to the decay* $B^0 \to f_0 K_S^0$.

A variety of $b \to s\bar{q}q$ penguin dominated modes have been measured by both

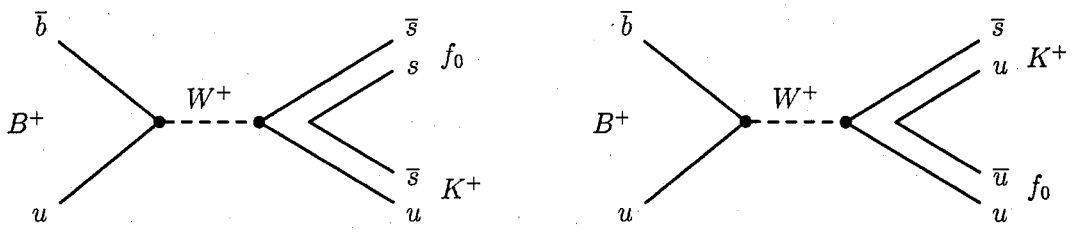

Fig. 1.9.— *Annihilation diagrams contributing to* $B^+ \to f_0 K^+$. *No corresponding diagrams exist for* $B^0 \to f_0 K^0$.

BABAR and Belle. A summary of these measurements as of October 2006 is shown in Table 1.6.

Mode	Experiment	$\sin 2\beta_{\rm eff}$	C	Reference
ϕK^0	Belle	$0.50 \pm 0.21 \pm 0.06$	$-0.07 \pm 0.15 \pm 0.05$	hep-ex/0608039
$\eta' K^0$	*BABAR*	$0.55 \pm 0.11 \pm 0.02$	$-0.15 \pm 0.07 \pm 0.03$	hep-ex/0607100
	Belle	$0.64 \pm 0.10 \pm 0.04$	$0.01 \pm 0.07 \pm 0.05$	hep-ex/0608039
	Average	0.59 ± 0.08	-0.08 ± 0.06	
$K^0_S K^0_S K^0_S$	*BABAR*	$0.66 \pm 0.26 \pm 0.08$	$-0.14 \pm 0.22 \pm 0.05$	hep-ex/0607108
	Belle	$0.30 \pm 0.32 \pm 0.08$	$-0.31 \pm 0.20 \pm 0.07$	hep-ex/0608039
	Average	0.51 ± 0.21	-0.23 ± 0.15	
$\pi^0 K^0_S$	*BABAR*	$0.33 \pm 0.26 \pm 0.04$	$0.20 \pm 0.16 \pm 0.03$	hep-ex/0607096
	Belle	$0.33 \pm 0.35 \pm 0.08$	$0.05 \pm 0.14 \pm 0.05$	hep-ex/0609006
	Average	0.33 ± 0.21	0.12 ± 0.11	
ρK^0_S	*BABAR*	$0.20 \pm 0.52 \pm 0.24$	$0.64 \pm 0.41 \pm 0.20$	hep-ex/0608051
ωK^0_S	*BABAR*	$0.62^{+0.25}_{-0.30} \pm 0.02$	$-0.43^{+0.25}_{-0.23} \pm 0.03$	hep-ex/0607101
	Belle	$0.11 \pm 0.46 \pm 0.07$	$0.09 \pm 0.29 \pm 0.06$	hep-ex/0609006
	Average	0.48 ± 0.24	-0.21 ± 0.19	
$f_0 K^0$	Belle	$0.18 \pm 0.23 \pm 0.11$	$0.15 \pm 0.15 \pm 0.07$	hep-ex/0609006
$\pi^0 \pi^0 K^0_S$	*BABAR*	$-0.84 \pm 0.71 \pm 0.08$	$0.27 \pm 0.52 \pm 0.13$	hep-ex/0508017
$K^+ K^- K^0$	*BABAR*	$0.41 \pm 0.18 \pm 0.07 \pm 0.11_{\text{CP-even}}$	$0.23 \pm 0.12 \pm 0.07$	hep-ex/0507016
	Belle	$0.68 \pm 0.15 \pm 0.03^{+0.12}_{-0.09\text{CP-even}}$	$0.09 \pm 0.10 \pm 0.05$	hep-ex/0609006
	Average	$0.58 \pm 0.13^{+0.12}_{-0.09\text{CP-even}}$	0.15 ± 0.09	
Mode	Experiment	$\sin 2\beta$	C	Reference
Charmonium	*BABAR*	$0.710 \pm 0.034 \pm 0.019$	$0.070 \pm 0.028 \pm 0.018$	hep-ex/0607107
	Belle	$0.642 \pm 0.031 \pm 0.017$	$-0.018 \pm 0.021 \pm 0.014$	hep-ex/0608039
	Average	0.674 ± 0.026	0.012 ± 0.022	

Table 1.6: *Measurements of* $\sin 2\beta_{\rm eff}$ *of different* $b \to s\bar{q}q$ *penguin-dominated modes, and of* $\sin 2\beta$ *from charmonium, as of October 2006, as compiled and averaged by [30].*

Chapter 2

The *BABAR* Detector

2.1 Overview

To measure *CP* in ϕK^0 and $f_0 K_S^0$ we need to *BABAR* detector to be able to: vertex the distance between the two B-meson decays so that Δt may be calculated; measure the speeds and momentums of the daughter pions and kaons, so that we may use particle identification (ID) and kinematics cuts to select ϕK^0 and $f_0 K_S^0$ decays; and identify K_L^0 mesons, and measure the direction of their momentum to select ϕK_L^0 decays; finally, we use the full capabilities of the detector to find the flavor of one of the B-mesons at the moment of its decay.

The *BABAR* detector operates at PEP-II B-factor which is located at the Stanford Linear Accelerator. PEP-II is an asymmetric e^+e^- collider operating at a center-of-mass energy of 10.58 GeV, which is the mass of the $\Upsilon(4S)$ resonance, and designed to operate at a luminosity of $3 \times 10^{33} cm^{-2} s^{-1}$. In PEP-II, the electron beam of 9.0 GeV collides head-on with the positron beam of 3.1 GeV, which results in a Lorentz boost of $\beta\gamma = 0.56$ to the $\Upsilon(4S)$ resonance. This Lorentz boost makes possible the

reconstruction of the two B-meson decay vertices, which in turn allows an analysis of the time-dependent CP asymmetry of their decay rates in general, and in particular in the cases when one of the B-mesons decays to ϕK^0 or $f_0 K_S^0$.

The *BABAR* detector consists of five different subdetectors. The silicon vertex tracker (SVT) is the innermost detector. It is surrounded by the drift chamber (DCH), which is in turn surrounded by the detector of internally reflected Cherenkov light (DRC), a novel type of detector used for particle identification. The DRC is surrounded by an electromagnetic calorimeter (the EMC). All of these are surrounded by a 1.5T superconducting magnetic solenoid. The instrumented flux return of the solenoid (the IFR) is fitted with resistive plate chambers. A 2-tiered triggering system integrates trigger information from the DCH, the EMC and the IFR. The data is written inspected by a user in real time (the data quality manager, or DQM), and written to disk. All this takes place as part of the online data acquisition system (DAQ.)

In general, many decays will produce charged particles with a momentum of less than 1 GeV/c so that multiple scattering is a significant limitation on the track parameter resolution. Hence, an effort is made to minimize the amount of material in the active region of the detector.

We now focus on each part of the detecter. More information may be found in Ref. [31], which is the source of the figures in this chapter.

2.2 The Silicon Vertex Tracker (SVT)

The SVT must in general measure the momentum and angles of charged tracks. It must also provide the distance between the decays of the two B-mesons, which means that the mean vertex resolution along the z-axis for a fully reconstructed B

decay must be better tham 80 μm. SVT track measurements are also important for extrapolation to the DRC, EMC and IFR. The SVT is particularly important for tracks with a transverse momentum of less than 100 MeV.

There are a number of physical constraints on the design of the SVT. It must fit inside the ~4.5 m-long support tube which extends the length of the detector. It must withstand 2 MRad of ionizing radiation. It is not easily accessible; any replacement of internal parts takes an estimated 4-5 months. So the SVT must be extremely reliable and robust.

The SVT is made of three inner and two outer layers of double sided silicon strip sensors. Strips on opposite sides of each sensor are oriented orthogonal to each other. The ϕ measuring strips are parallel to the beam, and the z measuring strips are oriented transversely to the beam axis. The sensors are organized into modules. The modules of the inner layers are straight, while those of the outer layers are arched. This arched design is to minimize the amount of silicon required to cover the solid angle, while increasing the crossing angle for particles near the edges of acceptance. Different sensor sizes are used ranging from 43 x 42 mm^2 (z x ϕ) to 68 x 53 mm^2. The half modules are given stiffness by two carbon fiber/kevlar ribs. A picture of the finished SVT is show in Figure 2.1. Diagrams of the front and side cross sections of the SVT are shown in Figure 2.2.

2.3 The Drift Chamber (DCH)

The purpose of the drift chamber is to provide detection, momentum measurements, tracking, and particle ID through dE/dx measurements of charged particles. In particular, reconstruction of K_s^0 mesons relies exclusively on the DCH. This means

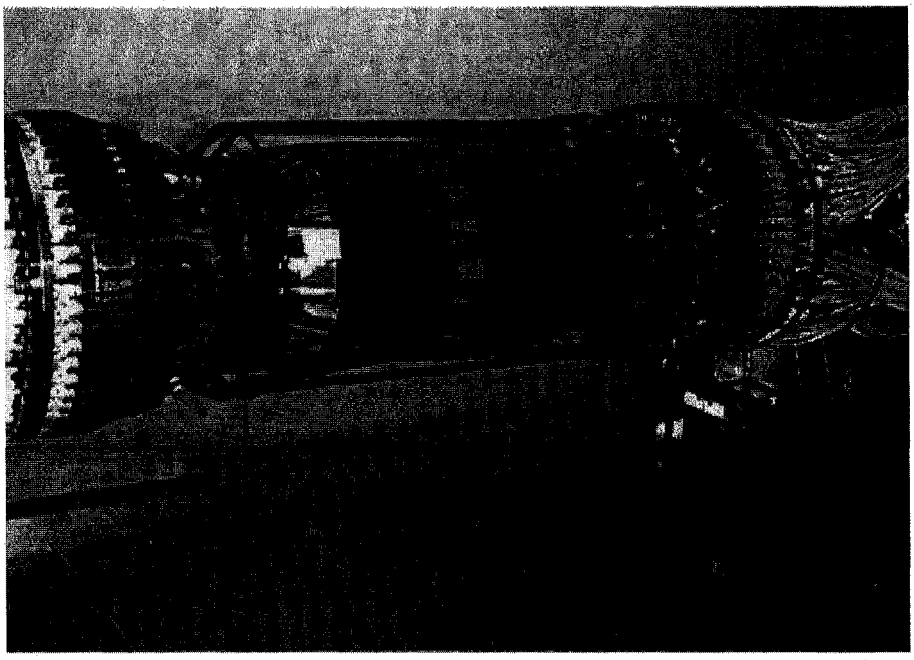

Fig. 2.1.— *This shows the finished SVT. The sensor modules can be seen on its surface. The black, cord-like structure is the carbon fiber space frame.*

that the DCH must be able to measure not only the transverse momenta and position of tracks, but also the longitudinal position with a resolution of 1 mm. DCH track measurements are also important for extrapolation to the DRC, EMC and IFR. Particle ID of low momentum requires DCH dE/dx measurements. A resolution of about about 7% allows π/K separation up to 700 MeV/c. Finally, the DCH must operate despite beam-generated background approximately $5kHz$/cell in the innermost layers.

The DCH is 3m long and has an inner radius of $0.236m$, which is limited by the size of the support tube, and an outer radius of $0.89m$, which is limited by the size of the DRC. The total thickness of the DCH at normal incidence is $1.08\%X_0$ [1] , of which the wires and gas mixture contribute $0.2\%X_0$, and the inner wall $0.28\%X_0$. The inner

[1]One X_0 is one radiation length

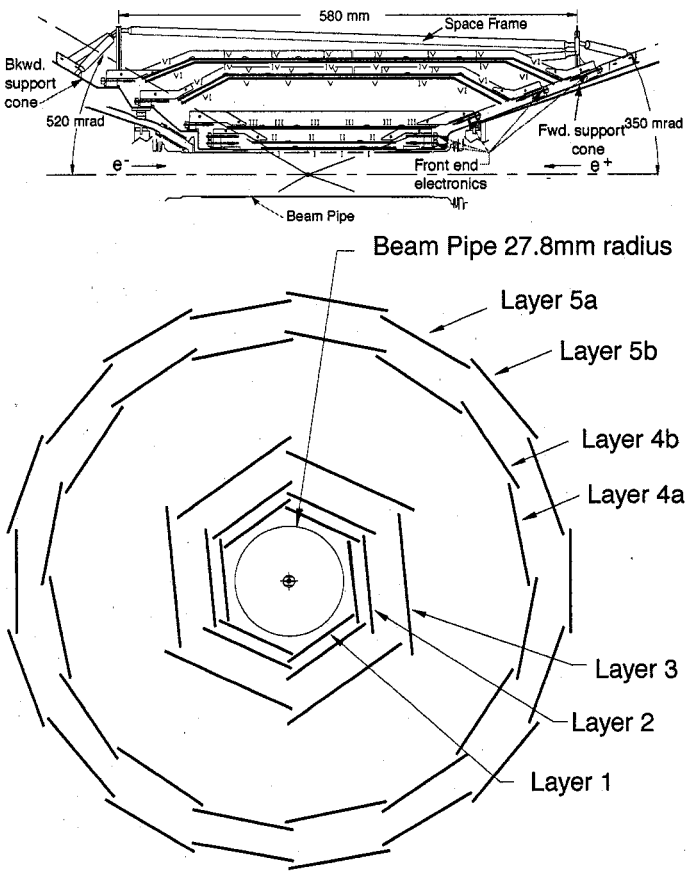

Fig. 2.2.— *Diagrams of the SVT, from the side (top) and from the front.*

cylindrical of the DCH is made of $1mm$-thick beryllium. The DCH has 40 layers of small, hexagonal cells providing up to 40 spatial and ionization loss measurements for charged particles with transverse momentum greater tham 180 MeV/c. Logitudinal position is obtained by placing the wires in 24 of the 40 layers at small anges with respect to the z-axis. The gas used is an 80:20 mixture of helium:isobutane. Its properties are presented in Table 2.1. This mixture has a radiation length that is five times larger than that of commonly used argon-based gases.

Parameter	Values
Mixture He:C_4H_10	80:20
Radiation Length	807 m
Primary Ions	21.2/cm
Drift Velocity	22μm/ns
Lorentz Angle	32°
dE/dx Resolution	6.9%

Table 2.1: *Properties of the helium-isobutane gas mixture used in the DCH, at atmospheric pressure. The Lorentz angle is stated for a 1.5 T magnetic field.*

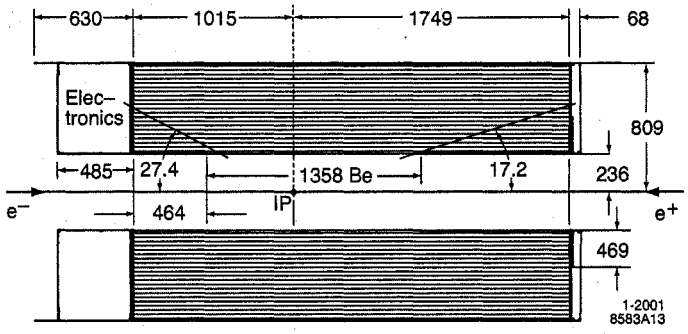

Fig. 2.3.— *Longitudinal section of the DCH. The chamber center is offset from the interaction point (IP) by 370 mm.*

2.4 Detector of Internally Reflected Cherenkov Light(DRC)

The DRC provides particle identification for charged tracks that are too energetic for the DCH to identify, that is tracks with an energy above about 700 MeV. This is essential for any measurement of time-dependent *CP* violation because it is needed to identify the flavor one of the B^0-mesons via the cascade decay $b \to c \to s$. The kaons used for flavor tagging have momenta that can be as high as 2 GeV/c, but generally are below 1 GeV/c. Additionally, for this analysis, kaon and pion discrimination of

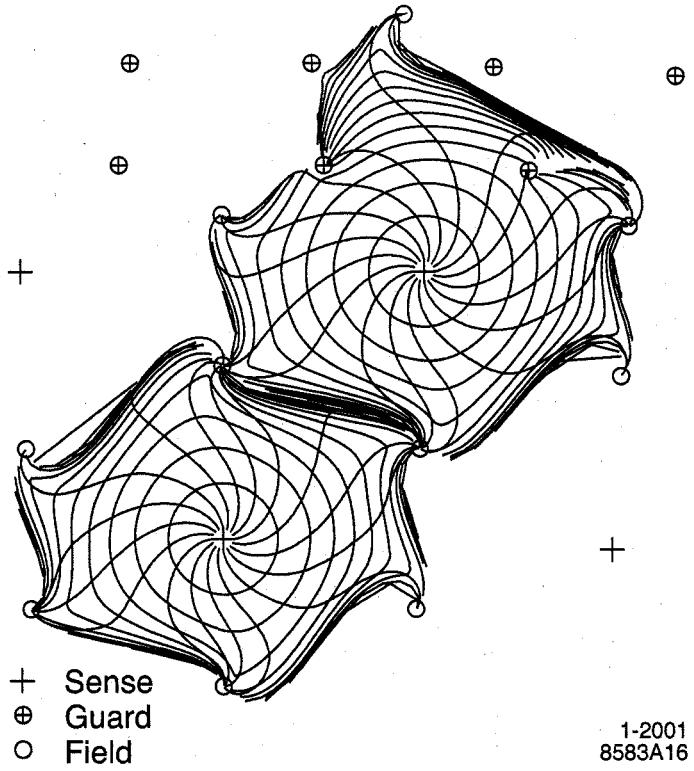

Fig. 2.4.— *Contours of equal drift times of ions in the cells of layers 3 and 4 of an axial superlayer. The isochrones are spaced by 100 ns. They are circular near the sense wires, but become more irregular near the field wires, and extend into the gaps between the superlayers.*

tracks too energetic for the DCH can help reduce background levels.

When charged particles pass through the rectangular synthetic fused silica of the DRC, they emit light at an angle that is determined by the familiar relation $\cos\theta_c = 1/n\beta$. Here, $\beta = v/c$, v is the velocity of the particle, c is the speed of light, and $n = 1.473$ is the index of refraction of the silicon. Since $\beta \approx 1$, some of the photons will internally reflect down the silica box to either end. One end has a mirror so that any photons will be reflected towards the opposite end. This other end connects to a

chamber full of water called the standoff box. A fused silica wedge reflects the light at large angles relative to the bar axis to reduce the required detection surface, and to prevent photons from being lost do to reflection at the silica-water interface. An array of photomultiplier tubes (PMTs) collect the photons about 1.17 m away from the end of the silica. Each PMT is surrounded by a light catcher cones to help collect photons the PMTs might otherwise miss. Ultimately, the DRC detects what amounts to a conic section formed by the photons emitted from the particle, which carries information about the angle of the emitted light, and ultimately the particle's speed. This is depicted in Figure 2.5.

The DRC has 144 rectangular synthetic fused silica bars. Each bar is 17 mm-thick, 35 mm-wide, and 4.9 m-long, and is assembled from four 1.225m pieces glued end-to-end. The bars are grouped into 12 groups of 12 bars each. Each group is stored in a separate hermetically container called a bar box, which is made out of very thin aluminum-hexcel panels. The standoff box is made of stainless steel, consists of a cone, a cylinder, and 12 sectors of PMTs, and holds about 6000 liters of purified water. Each of the 12 PMT sectors contains 896 PMTs, each with a diameter of 29mm. The effective active surface area light collection fraction is about 90%. Figure 2.6 shows different diagrams of the DRC. The DRC has a thickness of about 17% of a radiation length at normal incidence. The radiator bars subtend a solid angle corresponding to about 94% of the total azimuth and 83% of the CM polar angle cosine.

2.5 The Electromagnetic Calorimeter(EMC)

The electromagnetic calorimeter (EMC) measures electromagnetic showers with an excellent efficiency, and energy and angular resolution over an energy range from

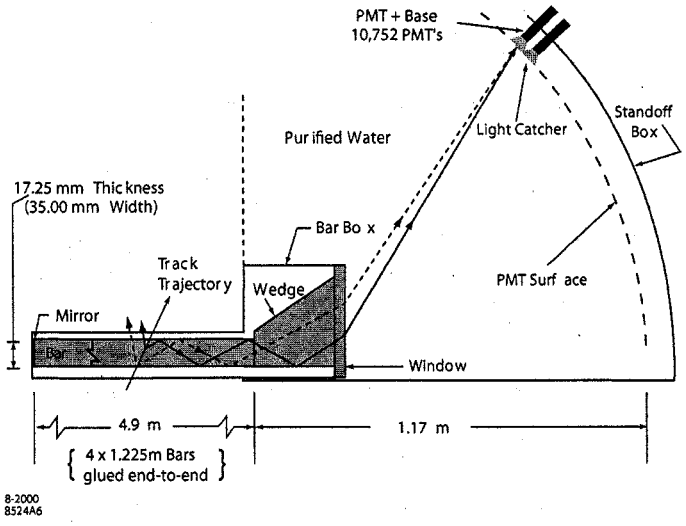

Fig. 2.5.— *A schematic of the operation of the DRC. Not shown is a 6 mrad angle on the bottom surface of the wedge.*

20 MeV to 9 GeV. It is very important for identifying K_L^0's. It also identifies electrons, which helps with B-meson tagging via semi-leptonic decays. Finally, it is important to muon detection. This is needed for reconstructing J/ψ mesons, which are part of most precision $\sin 2\beta$ measurements.

The EMC is composed of thallium doped CsI crystals. The properties of the CsI(Tl) crystals are shown in Table 2.2. The crystals provide full coverage of the azimuthal angle. Coverage is provided over the polar angle from 15.8° to 141.8°, which gives a 90% solid angle coverage in the CM system. The barrel contains a total of 5760 crystals in 48 rings, with 120 identical crystals each. The endcap contains 820 crystals in 8 rings, so this makes a total of 6580 crystals. The length of each crystal varies from 29.6cm towards the back of the EMC to 32.4cm towards the front, to limit the effects of shower leakage from increasingly energetic particles. The EMC

Parameter	Values
Radiation Length	$1.85cm$
Molière Radius	$3.8cm$
Density	$4.53g/cm^3$
Light Yield	$50,000\gamma/MeV$
Light Yield Temp. Coeff.	$0.28\%/°C$
Peak Emission λ_{max}	$565nm$
Refractive Index(λ_{max})	1.80
Signal Decay Time	$680ns(64\%)$
	$3.34\mu s(36\%)$

Table 2.2: *Properties of CsI(Tl) used as the material for the EMC crystals*

is supported only by the outer radius, with a thin gas shield at the front. Its barrel and the outer five rings of its endcap have less than $0.3 - 0.6X_0$ of material in front of the crystal faces. The SVT support and electronics, and the B1 dipole magnet are between the inner 3 rings and the beam, so that the inner 3 rings have $3.0X_0$ of material blocking them.

The crystals themselves are made from CsI salt doped with 0.1% thallium. They are shaped into tapered trapezoids with a tolerance of $\pm 150\mu m$, and then polished. The typical front face is $4.7 \times 4.7cm^2$, and the typical back face area is $6.1 \times 6.0cm^2$. Each crystal scintillates. With the aid of two layers of diffuse white reflector about $165\mu m$ thick on each crystal, it also guides the scintillated light. Each crystal is also wrapped in $25\mu m$ thick aluminum foil which is electronically connected to the metal housing of a photodiode preamplifier to provide a faraday shield. Finally, an outside covering of $13\mu m$ thick mylar assures electrical isolation. Two $2 \times 1cm^2$ silicon PIN diodes glued to the back of each crystal detect the light

2.6 The Instrumented Flux Return(IFR)

The instrumented flux return (IFR) is designed to identify muons with high efficiency and good purity, and neutral hadrons (K_L^0's and neutrons mostly) over a wide range of momenta and angles. Muons are important for tagging via semileptonic decays, and for reconstructing J/ψ muons. All of this requires large solid angle coverage, good effiency and high background rejection for muons down to below 1 GeV/c. To achieve this we use single gap resistive plate chambers (RPCs). The RPCs detect streamers from ionizing particles via capacitive readout strips. They are have a low cost of construction, and can cover odd shapes with minimal dead space. They produce large signals with a fast response time, about $1-2ns$. A position resolution of a few mm is achievable. The planar RPCs consist of two $2mm$ bakelite sheets separated by a gap of $2mm$. The gap is enclosed by a $7mm$ wide frame. The gap width is kept uniform by $0.8cm^2$ polycarbonate spacers glued to the bakelite, and spaced at distances of $10cm$. Finally, the bakelite surfaces that face the gap are treated with linseed oil. The RPCs are operated in limited-streamer mode, and the signals are read out capacitively on both sides of the gap by external electrodes made of aluminum strips on a mylar substrate. The cylindrical RPCs have resistive electrodes made of a special plastic composed of a conducting polymer and ABS plastic. They have a gap thickness and spacers identical to the planar RPCs. No linseed oil or other surface treatments are applied to them.

The RPCs are installed in gaps of the finely segmented steel of the barrel and end doors of the flux return. The steel segmentation was chosen on the bases of MC studies. The flux return consists of 18 plates, which increase in thickness from $2cm$

at its interior, to $10cm$ at its exterior. The nominal gap is $3.5cm$ in the inner layers, and $3.2cm$ elsewhere. In all, there are 19 RPC layers in the barrel and 18 in the endcaps. Two layers of cylindrical RPCs are installed between the EMC and magnet cryostat to detect particles exiting the EMC. The total active area of the IFR is about $2001m^2$, covered by 806 RPC modules. More than 25 different shapes and sizes of RPCs were built, and their sizes and shapes are matched to the steel dimensions to create very little dead space. There are 57 in each of the six barrel sectors, 108 in each of the four half-end doors, and 32 in the two cylindrical layers. They operate with a non-flammable gas mixture, typically 56.7% argon, 38.8% freon 134a (1,1,1,2 tetraflouroethane), 4.5% isobutane.

2.7 The Trigger and Data Acquisition(DAQ) System

The trigger system must keep the total event rate under about 120 Hz; the background is about 20 kHz each for one or more tracks in the DCH with transverse momentum greater than 120 MeV/c or at least one EMC cluster with a deposited energy greater than 100 MeV. The trigger system must be also be responsible for very little dead time, ideally less than 1%. It consists of a two-level system, L1 in hardware, and L3 in software. (The moniker L2 was reserved in case a third layer had to be added to the trigger system.)

The L1 has a typical output rate of 1kHz. It produces triggers within a fixed latency window of 11-12 μs after collision, which it delivers to the fast control and timing system (FCTS.) These triggers are based in information from the DCH, EMC, and IFR, and are produced by the DCH trigger (DCT), the EMC trigger (EMT), and the IFR trigger (IFT), respectively. The DCT and EMT can produce triggers more or

less independently, which gives a high level of redundency that is useful for testing and diagnostic purposes. The IFT triggers on $\mu^+\mu^-$, which can be used to study cosmic rays for diagnostic purposes. In any case, the data used to form the trigger decision is saved. The DCT and EMT feed the triggers, and the type of trigger event, into the global level trigger (GLT) every $134ns$. The GLT sends this to the FCTS, which decides whether to trigger based on the trigger event.

Any triggered events are ultimately given to the L3 trigger, which reduces the rates for the main physics sources, identifies and flags special categories of events needed for luminosity determination, diagnostic, or calibration purposes. To do this, the L3 trigger partially reconstructs the events using a linux online computer farm. It runs within the Online Event Processing (OEP) framework, which delivers the events to L3, and then logs what L3 tells it to. Since the events are partially reconstructed, they can be used for online quality monitoring. The L3 output rate is about 100 Hz.

The data acquisition (DAQ) system includes everything in the data collection chain from the common front end electronics (FEE) to the L3 trigger to the logging of event data. It must support an L1 trigger accept rate of up to 2 kHz, with an average event size of approximately 32 kbytes, and a max output (L3 trigger rate) of 120 Hz. On average it should not contribute more than 3% deadtime. The online dataflow system (ODF) is responsible for communication with and control of the detector systems' front end electronics, and for the acquisition and building of event data from them. The OEP system is responsible for processing of complete events, including the L3 software triggering, for data quality monitoring, and for the final stages of calibrations. The logging manager (LM) is responsible for receiving selected events from OEP, and writing them to disk for input to the online prompt reconstruction (OPR)

processing. The online detector control (ODC) system must control and monitor the environmental conditions for the detector systems. The online run control (ORC) system ties together the other systems, and must sequence their operations. It provides a GUI to aid its operators.

The entire DAQ system is coded primarily in C++, with some JAVA for the GUIs. The FEE are controlled by and communicated with via 157 custom VME Readout Modules (ROMs.) These ROMs are grouped by detector subsystem, and housed in 23 data acquisition VME crates that are controlled by ODF software. One ROM in each crate aggregates data, and then forwards it for event building in a linux workstation PC farm. The crates and farm machines communicate via 100 Mbits/s ethernet linked by a network switch- the event builder switch. ROMs are supported by a boot server which provides core and system-specific code and configuration information. Farm machines host OEP and L3 trigger software. The information is written to a disk buffer via LM software. Several additional file servers hold the online databases and productions software releases. A further set of application servers host the central functions of the various online subsystems. Operator displays are supported by a group of ten console servers. Fifteen VME crates contain data acquisition hardware for detector control subsystems. All VME crates, the online farm, and all application and console servers are connected via a switched 100Mbits/s ethernet network that is distinct from that used for event building, with a 1Gbits/s fiber ethernet used for file servers and interswitch links. The DAQ system is controlled through a custom Motif GUI for run control, and an extensive hierarchy of displays for detector control, including control panels, strip charts and an alarm handler. The electronic logbook is available through a web browser interface.

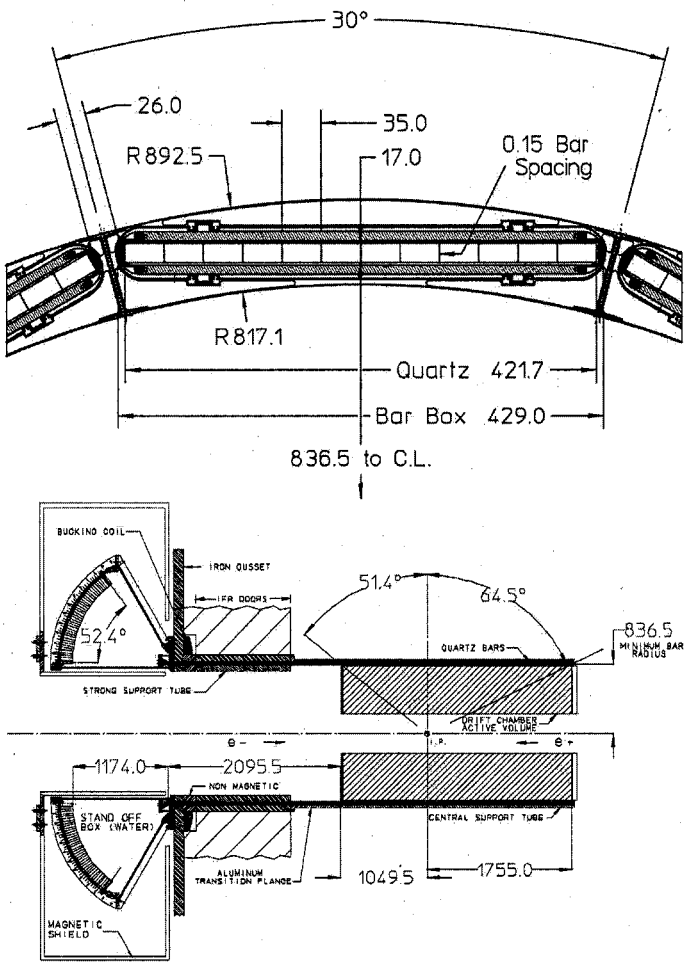

Fig. 2.6.— *Diagrams of the DRC. The top figure shows a transverse section of the nominal DRC bar box. The bottom shows the geometry of the entire DRC. The end plug is not shown. All dimensions are given in mm.*

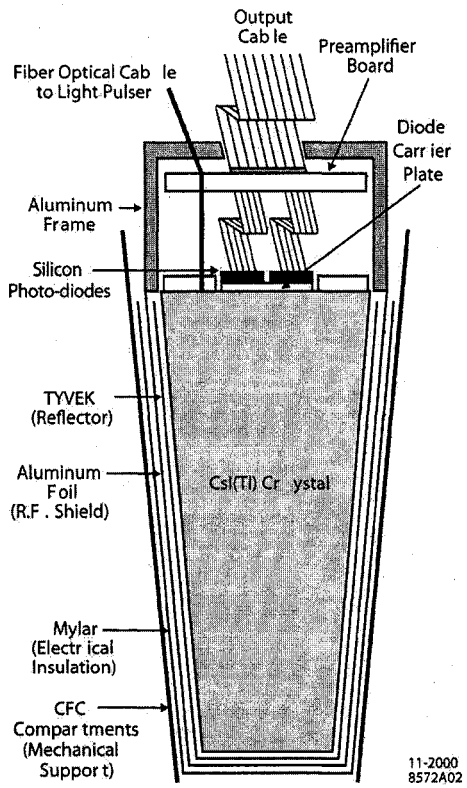

Fig. 2.7.— *Diagram of an individual EMC crystal.*

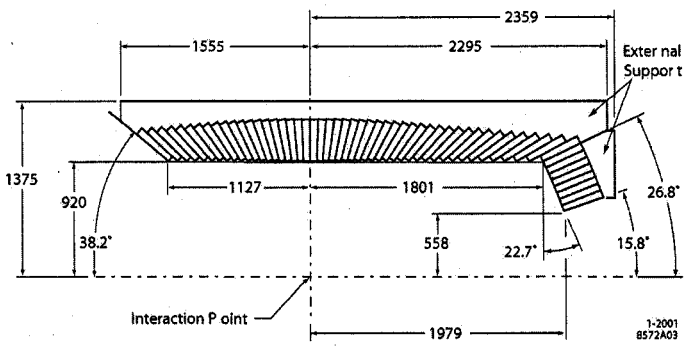

Fig. 2.8.— *Longitudinal diagram of the top half of the EMC*

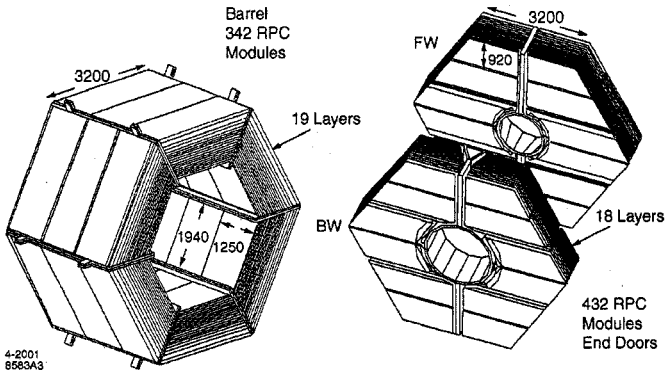

Fig. 2.9.— *Diagram of the steel chambers of the IFR.*

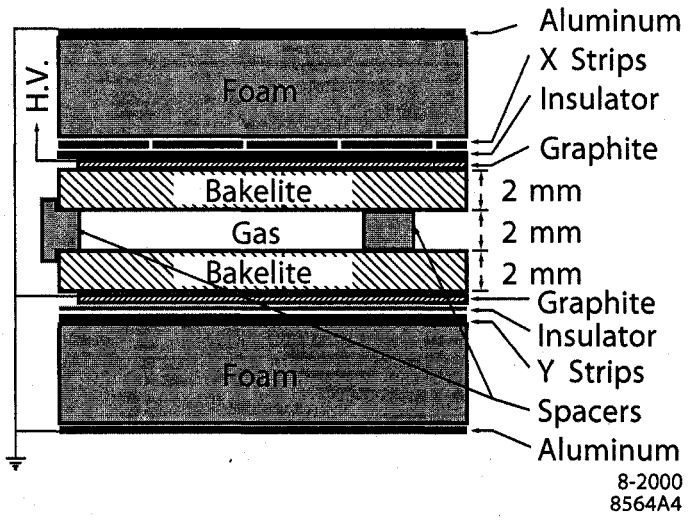

Fig. 2.10.— *Diagram of an IFR RPC module.*

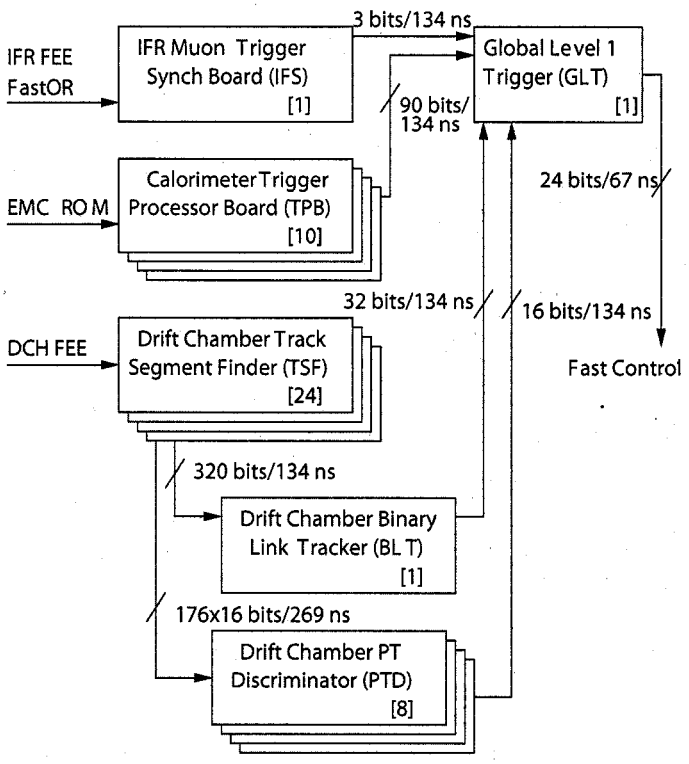

Fig. 2.11.— *Schematic of the level 1 trigger.*

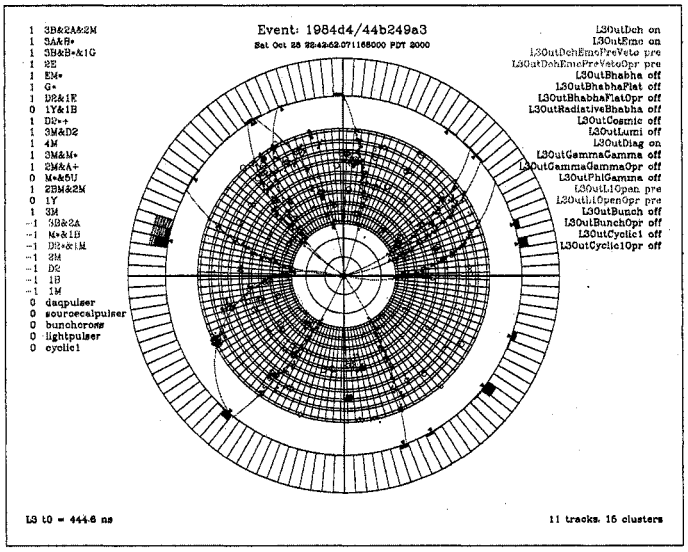

Fig. 2.12.— *The level 3 trigger display.*

Chapter 3

Experimental Analysis Overview

3.1 Extracting the CP parameters S and C

The analysis presented in this note uses the so-called quasi-2-body (Q2B) approximation, which represents a branch cut in the Dalitz Plot in order to isolate the resonant ϕK^0 or $f_0 K^0_S$ decay. In this approximation, ϕK^0 or $f_0 K^0_S$ is a CP eigenstates. Assuming CP violation in $B^0\overline{B}^0$ mixing is absent ($|q/p| = 1$), and assuming $\Delta\Gamma_{B_d} = 0$ as well as CPT invariance, the time-dependent probability density function (PDF) for events tagged as B^0 and $\overline{B}^0$, respectively, can be written in a model-independent way as

$$\begin{aligned} f_{B^0\text{tag}}(\Delta t) &= \frac{e^{-|\Delta t|/\tau_{B^0}}}{4\tau_{B^0}}\Big(1 + S\sin(\Delta m_d \Delta t) - C\cos(\Delta m_d \Delta t)\Big), \\ f_{\overline{B}^0\text{tag}}(\Delta t) &= \frac{e^{-|\Delta t|/\tau_{B^0}}}{4\tau_{B^0}}\Big(1 - S\sin(\Delta m_d \Delta t) + C\cos(\Delta m_d \Delta t)\Big), \end{aligned} \tag{3.1}$$

where the unknown parameters S and C are defined in equation 1.9, and violate CP symmetry if their values are non-zero. The parameter S probes mixing-induced CP

violation (CPV) and C determines direct CPV. (*cf.* Section 1.4.)

3.2 Signature of Charmless 3-body Decays

B-mesons decay predominately through $b \to c$ transitions. Charmless 3-body decays tend to involve either a $b \to u$ transition, or are penguin-only decay modes (such as $B^0 \to \phi K^0$), and have a branching fraction of the order of 10^{-6}. The cross section for continuum production is roughly the same as that for $b\bar{b}$ production at the $\Upsilon(4S)$ resonance (see Table 3.1), so that we must supress continuum background by a factor of roughly 10^6. We do this by making cuts on the kinematic variables, dalitz variables, and event shape information. We use advanced, multi-variable techniques to exploit as much information from the variables as possible. Ultimately, a tight cut on the mass of the ϕ candidate makes the ϕK^0_S mode relatively clean. However, the greater width of the f_0, and the increased background due to K^0_L reconstruction, make continuum much more of a problem for the $f_0 K^0_S$ and ϕK^0_L modes.

$e^+e^- \to$	Cross-section(nb)
$b\bar{b}$	1.05
$c\bar{c}$	1.30
$s\bar{s}$	0.35
$u\bar{u}$	1.39
$d\bar{d}$	0.35
$\tau^+\tau^-$	0.94
$\mu^+\mu^-$	1.16
e^+e^-	~ 40

Table 3.1: *Calculated production cross-sections at* $\sqrt{s} = M(\Upsilon(4S))$. *The* e^+e^- *corss-section is the effective cross-section, expected within the experimental acceptance[12].*

A B meson candidate is characterized kinematically by the beam energy substi-

tuted mass

$$m_{\rm ES} = \sqrt{(\frac{1}{2}s + \mathbf{p}_0 \cdot \mathbf{p}_B)^2/E_0^2 - p_B^2}\ . \tag{3.2}$$

and the energy difference

$$\Delta E = E_B^* - \frac{1}{2}\sqrt{s}\ , \tag{3.3}$$

where $\sqrt{s} = 10.58\,\mathrm{GeV}$ is the CM energy[1] , and the B momentum and the four-momentum of the initial state, $(E_i, \mathbf{p}_i)$ are defined in the laboratory frame. $m_{\rm ES}$ peaks at the B^0 mass for signal, with a width of about 2.5 MeV, and is limited mainly by knowledge of the beam energy and direction. Continuum $m_{\rm ES}$ is parameterized by the ARGUS shape[32], which simply reflects the relationship of $m_{\rm ES}$ to phase space. The typical ΔE resolution is about 15 MeV. If a non-signal B-decay channel is reconstructed as signal, any missing tracks will cause the ΔE resolution from that channel to peak at a value greater than or less than zero. For four and five body modes, reconstruction misses tracks, and their ΔE distribution peaks below zero; for two body modes, reconstruction adds tracks, and their ΔE peaks above zero. We parameterize continuum ΔE shapes with low order polynomials.

For the K_L^0 analyses, we are able to measure the direction, but not the magnitude, of the K_L^0 candidate's momentum. We assume a nominal B-meson mass, and can no longer use $m_{\rm ES}$. The distribution of ΔE is then quite different from that of a typical three-body mode, and becomes analogous to $m_{\rm ES}$. For ϕK_L^0, the typical resolution ΔE resolution is about 2.5 MeV.

In the analyses described in this note, a B candidate is formed by producing an

[1]The value of s is measured on a per-event basis using the total magnetic bending strength (including effects of off-axis quadrupole fields, steering magnets, and wigglers) and the average deviations of the accelerating frequencies from their central values[31].

$h^+h^-K^0_S$ candidate where $h = \pi$, or K, or by producing a $K^+K^-K^0_L$ candidate. Any ϕK^0_S or $f_0K^0_S$ candidate must then pass the (loose) requirements that $m_{\rm ES} > 5.1\,{\rm GeV}$ and $\Delta E < 0.450\,{\rm GeV}$, while a ϕK^0_L candidate must satisfy $|\Delta E| < 0.15\,{\rm GeV}$. This is referred to as the "preselection" stage of reconstruction.

The quasi-2-body approximation consists of reducing the decay kinematics of the kinematically allowed region in the Dalitz plot to bands or cross-bands, which (usually) are dominated by a single resonance, with more or less significant cross feed from other resonances through interference. We cut on the Dalitz plot by cutting on the mass of the ϕ or f_0 candidate, and by cutting on the absolute value of their helicity, which is defined as the angle between the positive kaon or pion in the ϕ or f_0 center-of-mass frame, and the ϕ or f_0 flight direction in the laboratory frame.

3.3 Misreconstruction of Signal

Signal candidates may be misreconstructed. We call these events self-cross-feed (SCF). Typically this occurs when a soft track is mistaken for a daughter of the f_0 or ϕ resonance. The K^0_L may also be misidentified. If the anything besides the K^0_L is misreconstructed, in general the distribution of the discriminating variables will be different. In particular, the $m_{\rm ES}$ and ΔE resolution is decreased. For this reason, the final fit must parameterize SCF and truth matched signal events separately. However, since reconstruction involves only charged tracks, SCF is not a large problem for ϕK^0_S or $f_0K^0_S$. The rate of K^0_L misreconstruction is somewhat higher, but does not result in a significantly different ΔE resolution, and does not need to be parameterized separately in the final fit.

3.3.1 Decay Topology

We can exploit the shape of the decay tracks in the center-of-mass frame to discriminate between signal and continuum background. Since the center-of-mass energy is close to the combined mass of the two B-mesons, they are produced almost at rest, and each decays fairly isotropically. Continuum events, on the other hand, are characterized by jets produced by the two quarks. If a particular event is a B decay, all the tracks not used to reconstuct the signal B-meson should be roughly isotropic. To quantify how isotropic or jet-like those tracks are, we use the **monomials L_n**, a set of momentum-weighted sums over the tracks in the rest-of-the-event (ROE) with respect to the B thrust axis T_B [33]:

$$L_n = \sum_{i=\mathrm{ROE}} p_i \times |\cos(\theta_{T_B,i})|^n \ , \tag{3.4}$$

where we use in particular L_0 and L_2 [34]. We require that any neutral object in the ROE have a minimum energy of 100 MeV.

Multivariate Analyzer techniques can be used to combine L_0 and L_2 with other event shape or kinematic variables to enhance supression of continuum background. To simplify systematic studies we do not include kinematics specific to the ϕ or f_0 (for example, dalitz plot variables) in the MVA, including them in the likelihood fit instead.

We have tried several combination of non-global variables [35] and found that the combination of the following four leads to close-to optimal results, while maintaining simplicity. Note that all variables used below are defined in the center-of-mass.

- L_0 and L_2.

- $\mathbf{cos\theta_{B,z}}$, the cosine of the angle between the CM B direction and the z axis. With full detector acceptance, it follows a $\sin^2\theta$ (uniform) distribution for signal (continuum background) events. We use the modulus $|\cos\theta_{B,z}|$ in the MVA.

- $\mathbf{cos\theta_{T_B,z}}$, the cosine of the angle between the candidate's thrust axis and the z axis. With full detector acceptance, It has a uniform $1+\cos^2\theta$ distribution for signal (continuum background). We use the modulus $|\cos\theta_{T_B,z}|$ in the MVA.

Two MVA techniques, a linear Fisher discriminant (FI) [36], and a non-linear Neural Network (NN) [37], have been studied. The latter is a *MultiLayerPerceptron* Neural Network with the following architecture:

- number of input variables: $N_{\rm var} = 4$;

- number of output classes: 2 (signal and background;

- number of layers: 4 (input, output & 2 hidden layers);

- number of neurons per layer: $N_{\rm var}$, $N_{\rm var}-1$, $N_{\rm var}-2$, 2;

- number of training cycles: ca. 5000;

- size of the training samples: 10000 signal MC events and 10000 off-resonance data events.

Optimization and training of the MVAs uses off-resonance data contained in the signal region to reduce residual correlations of the NN with the kinematic variables used in the ML fit, and is done separately for each analysis.

3.3.2 B background

We introduce a corrective probability density function (PDF) in the likelihood for classes of major contaminating modes, that is more than one event expected in the data sample after the candidate selection. An extensive list of exclusive charmless $B\overline{B}$ modes has been studied to evaluate the systematics on the event yields and the CP parameters due to cross-feed from these modes. The modes can be categorized as two-, three- and four-body final states, for which the decay kinematics differ significantly.

- **Two-body modes**: to reconstruct, *e.g.*, a $B^0 \to f_0 K^0_S$ or ϕK^0_S candidate from pairs of π/K^0_S, one adds an additional object (charged or K^0_S) taken from the rest of the event: as a consequence, these events populate the positive ΔE region. Since background from two-body events is weak, we do not apply an additional cut on the invariant mass of track pairs. The rates of the two-body decays are well-known experimentally.

- **Three-body modes**: by exchanging K^0_S or pions between the signal B and the ROE, or by picking up misidentified kaons, one can reconstruct a $B^0 \to f_0 K^0_S$ or ϕK^0 candidate from another three-body mode. This approximately leaves ΔE unaltered, *i.e.*, $\Delta E\,(\text{three}-\text{body}) \sim 0$ – albeit with worse resolution. The kinematics of these processes resemble that of the signal, so that the three-body cross-feed is difficult to suppress without compromising the signal efficiency. In particular, three-body background exhibits similar kinematic properties as misreconstructed signal events. The branching fractions of most of the three-body modes have been measured.

- **Four-body modes**: by using only three objects of a four-body decay, one can reconstruct a $B^0 \to f_0 K_S^0$ or ϕK^0 candidate that accumulates in the negative ΔE region. Many of the four-body decays have not been measured yet although good progress has been made recently.

- **Higher multiplicity modes**: the rates of modes with five or more particles in the final state are unknown in general and thus cannot be accounted for in a systematic way in the analysis. Kinematically, these modes resemble charmed $b \to c$ background due to the large negative ΔE values. Since we apply a relatively tight ΔE requirement for signal candidates, cross-feed from $\geq$ 5-body charmless background is assumed to be taken care of by the generic B and the continuum contributions to the likelihood.

We use the world average branching fractions computed by the HFAG [30] for the experimentally known decay modes. In cases where only upper limits are given, we translate the limits into branching fractions using the available information from the related publications. Educated guesses are used to deduce the branching fractions for the unknown modes. This is done using wherever possible similar modes that are known, together with rules based on isospin symmetry and/or form factor arguments, where naive factorization of the matrix elements is assumed in the latter cases. If such rules are not available, we rely on theoretical results from QCD Factorization [13], or *ad hoc* assumptions that consequently entail large systematic uncertainties.

In B decays into two vector mesons the vector-vector state can have $L = 0, 1, 2$ orbital angular momenta corresponding to longitudinal and transverse polarizations. Only longitudinally polarized particles create sufficiently fast decay pions and kaons

to produce significant background after the candidate selection. We assume in the following in cases when the polarization is unknown that the corresponding modes be longitudinally saturated, which is in accordance with recent experimental results [39]. An uncertainty of 100% is assigned to this assumption.

In the fit, individual modes with expected contamination of one or more events after selection are classified within two classes for charged charmless B decays, seven classes for neutral charmless B decays, and each one class for charged and neutral $b \to c$ decays, respectively. The classes regroup modes with similar PDFs and each class represents a corrective term in the likelihood. Their branching fractions, selection efficiencies and expected number of events, computed for an integrated on-resonance luminosity of 112 fb^{-1}, are discussed below and summarized in Tables 5.3-5.4.

Note that, if not stated otherwise, all branching fractions are given as products of branching fractions including the rates of sub-decays.

3.3.3 Tagging Efficiencies

For B-background modes faking our signal by picking a track from the tag side, or leaving a track to the tag side, the tagging properties can be modified compared to the signal case. (For more information on B-flavour tagging, see Section 3.6.) In particular, the tagging efficiencies per each tagging category can be affected. For example, the `Lepton` category owes less tracks on the tag side than other hadronic categories, leaving less room for combinatorial effects with the CP side. This leads to a lower tagging efficiency in this category for the concerned modes, which is to say that there is less B-related background in this category. Specific B-background tagging efficiencies are obtained from MC simulation. For charm B background, we

use the default BReco tagging efficiencies (*cf.* Ref. [40] and Section 4.6). The mistag probabilities are assumed to be mode-independent, so that we can use the numbers obtained from fits to BReco events [40].

3.3.4 *CP* Parameters

We use the same Δt model parameters for the B background as for signal. All model parameters are varied coherently among all modes for systematics. We neglect the difference in the vertex resolution between a nominal signal candidate and a B-background event. If the *CP* parameters are known, then they are set to their known values. Otherwise, they are set to zero. In any case they are varied as a systematic.(Since the notion of charge is absent in these analyses, the sensitivity to charge-related asymmetries, *e.g.*, tag-charge correlations, is greatly reduced.) The tagging fractions are obtained from MC simulation.

3.4 Track Lists

Reconstructed tracks, or groups of tracks, that pass certain critera are placed in "lists". The following lists are used for reconstruction:

- **ChargedTracks**: Any candidate with a non-zero charge; a pion mass is assumed.
- **KsDefault**: Any pair of candidates from **ChargedTracks** with a mass between $0.47627\,\mathrm{GeV}/c^2$ and $0.52267\,\mathrm{GeV}/c^2$.
- **GoodTracksVeryLoose** Any candidate from the **ChargedTracks** list that also has a maximum momentum of 10 GeV, a maximum distance of closest ap-

proach to (0,0) in the xy plane that is less than $1.5cm$, and a distance of closest approach to $z = 0$ that is less than $10cm$.

- **GoodTracksLoose** Any candidate that is in the **GoodTracksVeryLoose** list that has has a minimum transverse momentum of 100 MeV and at least 12 hits in the DCH.

- **KlongEMCLoose** Selects candidates in the EMC that may be a K_L^0. A simple minimum energy requirement (greater than 0.1 GeV) is placed on the energy deposited in the calorimeter.

- **KlongEMCTight** More discriminating that **KlongEMCLoose**. Cuts more tightly on the minimum required deposited energy, as well as a maximum energy (between 0.2 GeV and 2.0 GeV. The track must not be too much in the forward direction ($-1 < \cos(\theta) < 0.935$). The track must not be associated with any tracks in the DCH or SVT. Finally, it must not look like a merged π^0.

- **KlongIFRLoose** Selects candidates in the IFR that may be a K_L^0. Requires that the candidate have generated hits in the IFR (rather than just in the inner RPCs.)

- **KlongIFRTight** More discriminating than **KlongIFRLoose**. Require that the candidate not be pointed too much in either the forward or backward direction ($-0.7 < \cos(\theta) < 0.936$). The candidate cannot look like a kaon. Finally, the first hit on the endcap must not be beyond the 13th layer.

3.5 Vertexing and Δt Determination

Determining Δz and, from that quantity, Δt, is critical to these analyses. The SVT is responsible for the physical measurement of Δz. We use the same vertexing algorithms as the $\sin 2\beta$ from charmonium analyses does[41].

In calculating Δt from Δz, the $\sin 2\beta$ analysis in [41] includes a correction for the momentum of the two B-mesons in the $\Upsilon(4S)$ rest frame. This is called the average τ_b approximation, and works well for very clean channels. However, we have much more continuum background. A continuum event, of course, has no B-mesons, and using the average τ_b approximation for continuum events creates correlations between Δt and $\sigma(\Delta t)$ that are very difficult to model. To avoid this problem, we use the "boost" approximation, which does not correct for the momentum of the two B-mesons in the $\Upsilon(4S)$ rest frame. Instead, $\Delta t = \Delta z/(\gamma\beta c)$, where $\gamma\beta c\tau_b = 250\mu m$. The resolution of the Δt distribution is only 4% worse when using the boost approximation than when using the average τ_b approximation.

3.6 B-flavor Tagging

Determining, or tagging, the flavor of one of the B-mesons is essential to measuring time-dependant asymmetry. We reconstruct one B-meson candidate as decaying to the signal mode. A variety of methods are used to reconstruct the flavor of the other, "tag" B-meson. The Moriond tagging algorithm used in the present analyses is described in detail can be found in Ref. [42]. The brief review and the results given below are taken from that document, and from Ref. [43].

Semileptonic B-decays can be used to determine the flavor of the tagged B-meson. The most important variable for determing whether a particular track which

has been identified as a likely electron is also the daughter of a semileptonic B-decay that can be used to tag the flavor of the B is the center-of-mass momentum of that track.

Kaons can also be used to determine the flavor of the tagged B-meson. The dominant source of kaons are $b \rightarrow c \rightarrow s$ decays, which produce "right sign" kaons, meaning that a K^+ indicates a B^0 tag. A number of other processes also produce right sign, wrong sign, and neutral kaons. The multiplicities for right and wrong sign kaons from B decays have been measured by ARGUS[44]

$$n(B^0 \rightarrow K^+X) = 0.58 \pm 0.01 \pm 0.08 \tag{3.5}$$

$$n(B^0 \rightarrow K^-X) = 0.13 \pm 0.01 \pm 0.05 \tag{3.6}$$

Even a single kaon candidate can be used to tag the B flavor. For events with multiple candidates, tags based on the three best kaon candidates are used; the correlation of these three variables provide better tagging performance than just using the charge of the best kaon candidate.

Slow pions from $D^{*\pm}$ decays also tag the B flavor. In this case, a π^- indicates a B^0 tag. The $D^{*\pm}$ decays to a pion, and a D^0, which are emitted nearly at rest. Then the slow pion and the D^0 are boosted in the same direction by the momentum of the $D^{*\pm}$, which means we can expect that the slow pion direction in the B rest grame will be along the direction of both the D^0 decay products and the remainder of the B decay products.

Simply taking the charge of the track with the highest momentum in the $\Upsilon(4S)$ center-of-mass frame can also sometimes identify the flavor of the B. The purpose of this is to identify fast particles (for example fast pions from $B^0 \rightarrow D^*\pi$) and to recover

high momentum leptons that may have been missed by other tagging methods using other types of information. Any such particle is prompt and therefore a cut of 1 mm on the impact parameter in the transverse plane is made.

Technically, the event is evaluated separately using the physics information described above so that it has seven different tags assigned to it: `Electron`, `Muon`, `Kinematic Lepton` (uses kinematics of tracks to try to identify them as leptons), `Kaon`, `Slow Pion`, `K-Pi` (attempts to exploit correlations between kaons and slow pions), and `Max` p^*.

These seven different tags are then fed into a neural net, which combines them, and outputs a single tag between -1 and 1, with 1 representing a B^0 and -1 representing a $\overline{B}^0$. Each event is assigned one of nine mutually exclusive tagging categories, based on the physics content of the fit, e.g. how successful particular aspects of the tagging algorithm appear to have been at extracting the flavor of the tag. These categories are: `Electron`, `Muon`, `Electron-Kaon`, `Muon-Kaon`, `Kaon-Slow Pion`, `Kaon I`, `Slow Pion`, `Kaon II`, `Other`. These categories are then combined in into five final hierarchical categories:

- `Lepton` ≡ `Electron` + `Muon` + `Electron-Kaon` + `Muon-Kaon`.
- `KPIorK` ≡ `Kaon-Slow Pion` + `Kaon I`.
- `KorPI` ≡ `Kaon II` + `Slow Pion`.
- `Inclusive` ≡ `Other`.
- `Untagged` ≡ Neural net output less than 0.2.

Category	f	$\langle D \rangle$	ΔD	μ
Lepton	0.094 ± 0.001	0.919 ± 0.012	0.029 ± 0.022	-0.006 ± 0.019
Kaon I	0.164 ± 0.002	0.806 ± 0.012	0.043 ± 0.021	-0.038 ± 0.015
Kaon II	0.195 ± 0.002	0.600 ± 0.014	0.075 ± 0.022	0.003 ± 0.015
Inclusive	0.202 ± 0.002	0.366 ± 0.015	0.082 ± 0.023	0.006 ± 0.015
Untagged	0.345 ± 0.004	0	0	0

Table 3.2: *Tagging efficiencies f^c, average dilution $\langle D \rangle_c$, dilution difference ΔD_c, and tagging efficiency asymmetry μ_c for each tagging category c, as determined in the full* BReco *sample [43].*

Table 3.2 shows the breakdown of events into the five tagging categories $c = 1, \ldots, 5$ (first column), the average dilutions $\langle D \rangle_c$ (second column), dilution differences ΔD_c (third column), and the tagging efficiency asymmetries μ_c (last column) as determined from the full BReco sample. No difference has been found between pre- and 2003 data in Ref. [43], so we use the same parameters for the entire data set. Since we do not refit the BReco sample to obtain the tagging (and Δt resolution) parameters simultaneously with the signal observables, we treat the uncertainties on the parameters as part of the systematic errors (*cf.* Sections 5.8.1 and 4.8.1). Since the tagging efficiency asymmetries μ are not significant, we ignore them in the final fits. However, tagging asymmetries in charged B-background or self-tagging neutral B-background events are introduced for systematic studies, since non-zero values can occur in presence of direct CP violation. We also take into account tagging asymmetries for continuum background events, which are determined simultaneously with the signal parameters from on-resonance data.

3.7 Data Sample and Processing

The data is divided into four runs. Runs 1-3 is from 1999-2003. It may be processed using two slightly different software versions, the "release 12" (R12) software, or the "release 14"(R14) software. Runs 1-3 processed with R14 software includes slightly different amounts of data. Run 4 is from 2003-2004. Run 4 is itself divided into three data sets dubbed green circle (GC), blue square (BS) and black diamond (BD). The BS data set contains the GC data set, and the BD data set contains the BS data set.

Runs 1-3 when processed with the R12 software contains the following amount of data:

- Run-1 (R12): on-resonance - 20.5 fb^{-1}, off-resonance - 2.6 fb^{-1};
- Run-2 (R12): on-resonance - 60.3 fb^{-1}, off-resonance - 6.8 fb^{-1};
- Run-3 (R12): on-resonance - 29.5 fb^{-1}, off-resonance - 2.4 fb^{-1};
- Total number of $B\overline{B}$ events: (122.56 ± 0.68) million

Runs 1-4 when processed with the R14 software contains the following amount of data:

- Run-1 (R14): on-resonance - 19.5 fb^{-1}, off-resonance - 2.6 fb^{-1};
- Run-2 (R14): on-resonance - 60.1 fb^{-1}, off-resonance - 6.8 fb^{-1};
- Run-3 (R14): on-resonance - 30.1 fb^{-1}, off-resonance - 2.4 fb^{-1};
- Run-4(GC) (R14): on-resonance - 54.9 fb^{-1};

- Run-4(BS) (R14): on-resonance - 80.9 fb^{-1};
- Run-4(BD) (R14): on-resonance - 94.6 fb^{-1};
- Total number of GC $B\overline{B}$ events: 181 million
- Total number of BS $B\overline{B}$ events: 209 million
- Total number of BD $B\overline{B}$ events: 227 million

The $f_0K^0_s$ analysis described here consists of two different final fits. An original $f_0K^0_s$ fit is done for the *CP* asymmetry in and the yield of $B^0 \to f_0(980)(\to \pi\pi)K^0_s$. The yield is used to find a branching fraction. We will refer to this as the branching fraction (BR) fit, even though it also measures *CP* quantities. It is finally done to runs 1-3 processed with R12. The branching fraction is found to be systematics limited due to model assumptions (*cf.* Section 5.8.5.)

A second $f_0K^0_s$ fit is done that is more or less identical to the branching fraction fit, except that it is to a larger data set. We will call it the *CP* fit, even though it also fits for a yield. However, the necessary systematics have not been done to quote a true branching fraction from it. It is finally done to a data set of runs 1-3 processed with R12, and the BS run 4 processed with R14.

The final ϕK^0 fit is finally done to the BD data set, all processed with R14. We refer to it as the ϕK^0 fit.

For Monte Carlo (MC) studies we use Geant4 SP5 samples produced with the R12 software and SP6 samples produced with the R14 software. The signal MC sample size is 68k. For background studies, we use a sample of 171.73 million B^+B^- and 134.87 million $B^0\overline{B}^0$ SP5 events. We also use a wide variety of charmless modes

that have been generated for a many specific B backgrounds. These samples are are typically ~50–100K events.

3.8 Maximum Likelihood Fit

For all analyses, the selected on-resonance data sample is assumed to consist of signal, continuum-background and B-background components, separated by the flavor and category of the tag side. The variables that discriminate signal from background may include Δt, $m_{\rm ES}$, ΔE, NN′(the transformed NN shape, see Sections 4.4 and 5.3.2), and the Dalitz Plot ($m(h^+h^-)$ and $\cos\theta(h^+h^-)$, taken to be uncorrelated), depending on the fit. In particular, the Δt measurement allows us to determine mixing-induced CPV (3.1), and also provides additional continuum-background rejection. The signal likelihood consists of the sum of a correctly reconstructed (TM) component and a small misreconstructed (SCF) component for the $f_0K^0_S$ fits. (An SCF component is not needed for the ϕK^0 fit because the amount of SCF is small, or is due to a misreconstructed K^0_L.) The fit strategy is to determine as many continuum shape and asymmetry parameters as possible simultaneously with the signal parameters by the fit, which reduces systematic effects from the description of the dominant background piece.

The probability density $\mathcal{P}^c_i$ for a single event i in tagging category c is the sum of the probability densities of all components, namely (we have separated out the time-integrated asymmetry parameters),

$$\begin{aligned}\mathcal{P}^c_i \;\equiv\; & N_{sig} f^c_{sig}\left[(1-f^c_{\rm SCF})\mathcal{P}^c_{sig-{\rm TM},i} + f^c_{\rm SCF}\mathcal{P}^c_{sig-{\rm SCF},i}\right] \\ & + N^c_{q\bar{q}}\frac{1}{2}\left(1+q_{{\rm tag},i}A^c_{q\bar{q},{\rm tag}}\right)\mathcal{P}^c_{q\bar{q},i}\end{aligned}$$

$$+ \sum_{j=1}^{N_{\rm class}^{B^+}} N_{B^+j} f_{B^+j}^c \frac{1}{2} \left(1 + q_{{\rm tag},i} \langle D \rangle_c A_{B^+,{\rm tag},j}\right) \mathcal{P}_{B^+,ij}^c$$

$$+ \sum_{j=1}^{N_{\rm class}^{B^0}} N_{B^0j} f_{B^0j}^c \frac{1}{2} \left(1 + q_{{\rm tag},i} \langle D \rangle_c A_{B^0,{\rm tag},j}\right) \mathcal{P}_{B^0,ij}^c \ , \qquad (3.7)$$

where,

- N_{sig} is the total number of signal events the data sample;
- f_{sig}^c is the fraction of signal events that are tagged in category c;
- $f_{\rm SCF}^c$ is the fraction of misreconstructed signal events (SCF) in tagging category c;
- $\mathcal{P}_{sig-{\rm TM},i}^c$ and $\mathcal{P}_{sig-{\rm SCF},i}^c$ are the products of PDFs of the discriminating variables used in tagging category c, for truth-matched (TM) and SCF events, respectively;
- $N_{q\bar{q}}^c$ is the number of continuum events that are tagged in category c;
- $q_{{\rm tag},i}$ is the tag flavor of the event; we use $q_{{\rm tag},i} = 1$ for B^0-tag and $q_{{\rm tag},i} = -1$ for $\overline{B}^0$-tag (note that the working convention in RhoPiTools is opposite to this definition);
- $A_{q\bar{q},{\rm tag}}^c$ parameterizes possible category-specific tag asymmetries in continuum events;
- $\mathcal{P}_{q\bar{q},i}^c$ is the continuum PDF for tagging category c;
- $N_{\rm class}^{B^+}$ ($N_{\rm class}^{B^0}$) is the number of charged (neutral) B-related background classes considered (*cf.* Section 3.3.2);

- N_{B^+j} (N_{B^0j}) is the number of expected events in the charged (neutral) B-related background class j;
- $f^c_{B^+j}$ ($f^c_{B^0j}$) is the fraction of charged (neutral) B-related background events of class j that are tagged in category c;
- $\langle D \rangle_c$ are tagging dilutions due to mistagging
- $A_{B^+,\mathrm{tag},j}$ ($A_{B^0,\mathrm{tag},j}$) describes the tag asymmetry in the charged (neutral) B-background class j; this parameterizes a possible charge asymmetry in the B-background events;
- $\mathcal{P}^c_{B^+,ij}$ is the B^+-background PDF for tagging category c and class j;
- $\mathcal{P}^c_{B^0,ij}$ is the B^0-background PDF for tagging category c and class j; the time-dependent PDF is non-trivial as neutral B background can exhibit direct and mixing-induced CPV;

The PDFs $\mathcal{P}^c_X$ are the product of the PDFs of the (as many as) six discriminating variables x_k, $k = 1, \ldots, 6$:

$$\mathcal{P}^c_{X,i(j)} \equiv \prod_k P^c_{X,i(j)}(x_k) \; . \tag{3.8}$$

Finally, the extended likelihood over all tagging categories is given by

$$\mathcal{L} \equiv \prod_{c=1}^{5} e^{-\overline{N}^c_i} \prod_i^{N^c} \mathcal{P}^c_i \; , \tag{3.9}$$

where $\overline{N}^c$ is the number of events expected in category c. Including this term allows for the direct fitting of event yields rather than fractions. We fix the number of B-background events in the fit, and vary that number as a systematic.

The individual PDFs in Eq. (3.7) are discussed in the chapters on the individual analyses.

3.8.1 Time Dependence

The Δt-resolution function for signal and B-background events is a sum of three Gaussian distributions and scaled by the Δt per-event-error, with parameters determined by a fit to fully reconstructed B^0 decays (the `BReco` data set)[45]. The `BReco` data set consists of several high purity (approximately $80-90\%$) fully reconstructed $D^{(\star)}$-containing modes. Since the resolution of the tagged B-meson is so much worse than that of the signal B-meson, it dominates the Δz, and Δt, distributions of both the `BReco` and analyses data sets, so that the distributions should be identical to within the sensitivity of the final fits. For the B-background modes, the CP-violating parameters are fixed to 0 or to their known values. The continuum Δt distribution is also parameterized as the sum of three Gaussian distributions with two distinct means and three distinct widths which are scaled by the Δt per-event-error, but its parameters are determined in each final fit to data. The four continuum tag asymmetries are also determined in each final fit to data.

3.8.2 Correlations

The likelihood model assumes that the discriminating variables do correlate with each other. Violation of this assumption leads to biases in the fit. In general one expects the following tendencies:

- if the discriminating variables are correlated for the signal events, the observed (*i.e.*, fitted) signal yield will be larger than the true number of signal events in

the sample.

- if the discriminating variables are correlated for the background events, the observed signal yield will be lower than the true number of signal events in the sample.

In both cases, the goodness-of-fit test via a full likelihood projection comparison between data and fit model will reveal the problems [35]. Significant correlations are only observed in all fits for TM events between $m_{\rm ES}$ and ΔE. Their linear correlation coefficient amounts to -8.6%, which is a known feature and understood to be dominated by the common uncertainty on the beam energy. It can be approximated by [46,47]

$$\rho(m_{\rm ES}, \Delta E) \approx -\frac{\sigma(m_{\rm ES})}{\sigma(\Delta E)} = -8.4 times 10^{-2} . \tag{3.10}$$

Correcting ΔE for the error on the beam energy gauged, by $m_{\rm ES}$[48]

$$\Delta E \longrightarrow \Delta E + \delta_{E^*_{\rm beam}} \approx \Delta E + (m_{\rm ES} - \langle m_{\rm ES} \rangle) , \tag{3.11}$$

with $\langle m_{\rm ES} \rangle \simeq 5.2795$, reduces significantly the correlation[38]. *Note that we do not apply the correction (3.11) for the present analysis since dedicated MC fits did not reveal any significant bias when neglecting the correlations.* Figure 3.1 shows some typical correlations found between the discriminating variables.

Additionally, for $f_0 K^0_s$, significant correlations are observed between $\sigma(\Delta t)$ and the NN′ for TM signal events, which originate in the dependence of the vertexing on the kinematics of the ROE. It can be (handwavingly) understood as follows:

- L_0 is simply the sum of the ROE momenta (tracks and neutrals): the more tracks with significant momentum, the better the vertexing is;

- the same argument holds for L_2, but the effect is diluted by the shape of the event;
- the direction of the B momentum is only weakly correlated with the shape or the geometry of the event, so that no effect on $\sigma(\Delta t)$ is observed;
- acceptance effects make the vertexing worse when the B thrust axis approaches the beam pipe.

We assumed that the bias introduced by the $\sigma(\Delta t)$-vs-NN′ correlations when using both variables in the likelihood fit is neutralized by the per-event treatment ($\sim \Delta t/\sigma(\Delta t)$) in the Δt resolution function. Tests with embedded Monte Carlo samples have not revealed significant biases. We note that a potential bias due to this effect is present in all time-dependent analyses using MVA variables in the likelihood fit.

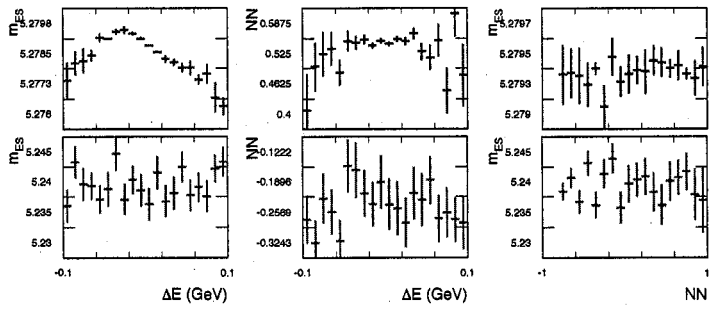

Fig. 3.1.— *Correlation profiles of* $m_{\rm ES}$ *versus* ΔE *(left column),* NN′ *versus* ΔE *(center column), and* $m_{\rm ES}$ *versus* NN′ *(right column), for* ϕK^0_S *events (upper line) and off-resonance events (lower line).*

3.9 Blind Analysis

The values of S and C of the ϕK^0 fit, and of S, C and the signal and continuum yields of the $f_0 K_s^0$ fit were hidden until the analysis cuts and fitting procedures were finalized. This prevents biasing the final results[49].

Chapter 4

ϕK^0 Analysis

4.1 Overview

The narrowness of the ϕ resonances helps reduce background in the study of both $B^0 \to \phi K_S^0$ and $B^0 \to \phi K_L^0$. This, compounded with the presences of only charged particles in the final state, makes $B^0 \to \phi K_S^0$ experimentally extremely clean. The neutral K_L^0 in the mode $B^0 \to \phi K_L^0$ complicates its study. We are able to reconstruct the direction of the K_L^0 momentum, but not its magnitude, or its energy. For reconstruction, we must assume a nominal B mass, effectively eliminating $m_{\rm ES}$ as a useful variable. After performing two different sets of cuts designed to select ϕK_S^0 or ϕK_L^0 candidates, we perform a single maximum likelihood fit for the CP parameters S and C on a data set of approximately 227 million $B\overline{B}$ pairs, where we assume that $S_{\phi K_S^0} = -S_{\phi K_L^0}$. Since $\eta_{\phi K_S^0} = -\eta_{\phi K_L^0} = -1$, we expect that $S_{\phi K_S^0} = \sin 2\beta$.

4.2 Event Selection: ϕK_S^0

The candidate selection is straightforward and uses general quasi-two-body (Q2B) rules.

- **Preselection**: a B candidate is formed by producing an $h^+h^-K_S^0$ candidate where $h = \pi$, or K. The kinematic cuts that we use for the preselection are $m_{\rm ES} > 5.1\,{\rm GeV}$ and $\Delta E < 450\,{\rm MeV}$.

- **Lists**: tracks are taken from the **GoodTracksVeryLoose** list and K_S^0 candidates are taken from the **KsDefault** list (using tracks from the **ChargedTracks** list).

- **Charged track requirements**:

  - Number of hits in the DCH ≥ 12.

  - $p_T({\rm track}) > 0.1\,{\rm GeV/c^2}$.

  The above track quality cuts make the list used in the analysis equivalent to **GoodTracksLoose**.

- **PID**: The K^+K^- candidates must identify as kaons, but not pions. No PID requirements are applied to the $\pi^+\pi^-$ pair coming from the K_S^0.

- **K_S^0 requirements**: the $K_S^0 \to \pi^+\pi^-$ decay (the $K_S^0 \to \pi^0\pi^0$ branch is ignored in the present analysis) is reconstructed from two oppositely charged tracks, without applying particle identification, fit to a common vertex. A candidate is required to have

  - a $\pi^+\pi^-$ invariant mass within $|m(\pi^+\pi^-) - m(K_S^0)| < 10\,{\rm MeV}/c^2$

- a lifetime significance, calculated in three dimensions, $\ell(K^0_S)/\sigma_{\ell(K^0_S)} > 5$.
- an opening angle α between the K^0_S flight direction and the vector between the ϕ and the K^0_S vertices of $\cos\alpha > 0.999$ ($\alpha < 2.6°$).

- **Dalitz plot (DP)**: The quasi-2-body approach consists of choosing a particular band in the Dalitz plot, which is determined by the presence of a ϕ resonance. The requirement applied is:
  - $1.01 < m(\phi \to \pi^+\pi^-) < 1.03\,\mathrm{GeV}/c^2$
  - The decay angle between the positive kaon and the momentum of the ϕ in the B frame is referred to as $\cos\theta(K^+K^-) = \cos\theta_H$. No cut on this angle is applied. It is used as a variable in the likelihood fit.

  The Dalitz plot requirements remove about 99% of the continuum background and 9% of the signal events.

- **Kinematic cuts**:
  - $\boldsymbol{m_{\mathrm{ES}}}$, the energy-substituted mass. We require $5.20 < m_{\mathrm{ES}} < 5.288$ GeV/c^2. (See left hand plot in Fig. 4.1 for the signal and continuum distributions of m_{ES}.)
  - $\boldsymbol{\Delta E}$, the difference between the reconstructed B energy in the CM, and the nominal CM beam energy is required to be within the interval $-0.1 < \Delta E < 0.1\,\mathrm{GeV}$.

- $\boldsymbol{\Delta t}$: We require $|\Delta t| < 20$ ps and $\sigma_{\Delta t} < 2.5$ ps, where $\sigma_{\Delta t}$ is the Δt per-event error .

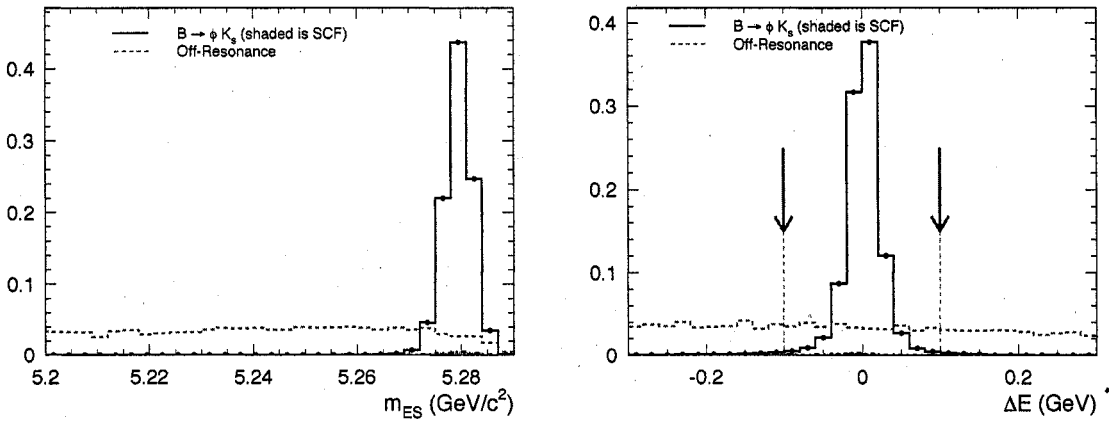

Fig. 4.1.— *Distributions of $m_{\rm ES}$ (left plot) and ΔE (right plot) for correctly reconstructed ϕK^0_S signal (solid with dots), SCF signal (shaded area), and continuum events from off-resonance data (dashed). The arrows indicate the requirements applied.*

- **MVA**: a description of the dedicated continuum-fighting Multivariate Analyzer (MVA) is given in Section 4.4. We use a four-variable Neural Network for which the output is required to be larger than -0.8 (Fig. 4.2).

If there is more than one candidate in an event which passes these criteria, the candidate with the best K_s mass is chosen. Of truth matched(TM) events[1], 0.2% have more than 1 candidate pass all selection; for events self-crossfeed (SCF) events[2], this number is 8.9%. The fraction of SCF events is $\sim$2% and comes from misidentified kaons (not from the pions from the K^0_S). This is small enough that the final fit does not need a separate SCF component for ϕK^0_S. The selection efficiencies are summarized in Table 4.1. A total of 2082 events remain after all cuts. In the following, the grand side-band (GSB) used for offpeak events refers to the above cuts but with $|\Delta E| < 0.4\,\mathrm{GeV}/c^2$.

[1]A truth matched event is one in which all of the tracks (the two from the ϕ and the two from the K^0_S) are correctly assigned in the event.

[2]An SCF event is one in which at least one of the tracks has been incorrectly assigned.

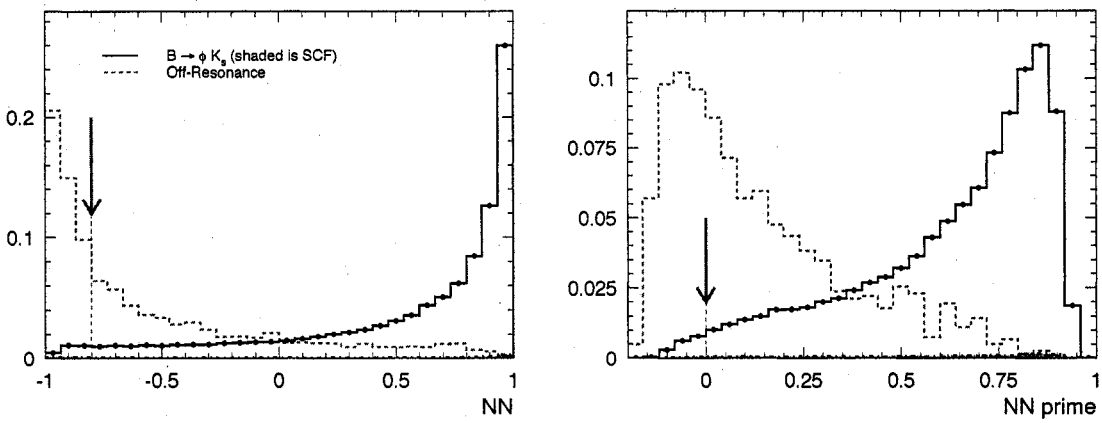

Fig. 4.2.— *Distributions of* NN *and* NN′ *for correctly reconstructed* ϕK_S^0 *signal (solid with dots), SCF signal (shaded area), and continuum events from off-resonance data (dashed). The arrows indicate the requirements applied. The* NN′ *is simply a transform so that the range is in [0,1].*

Cuts	Relative Efficiencies		
	$\epsilon^{\rm MC}_{\phi K^0_S}$	$\epsilon^{\rm data}_{\rm on-res}$	$\epsilon^{\rm data}_{\rm off-res}$
Preselection	0.6198 ± 0.0029	———	———
Track Quality	0.9987 ± 0.0001	0.9987 ± 0.0001	0.9987 ± 0.0001
$-0.1 < \Delta E < 0.1$	0.9184 ± 0.0013	0.3132 ± 0.0007	0.3167 ± 0.0005
m_{es} >5.2	0.9942 ± 0.0003	0.7515 ± 0.0011	0.7339 ± 0.0008
1.03> $m_{K^+K^-}$ >1.01	0.8621 ± 0.0009	0.0191 ± 0.0003	0.0188 ± 0.0001
$\lvert\Delta t\rvert$ <20 ps	0.9928 ± 0.0004	0.9525 ± 0.0040	0.9541 ± 0.0026
$\sigma(\Delta t)$ <2.5 ps	0.9520 ± 0.0009	0.8926 ± 0.0070	0.8846 ± 0.0048
K_s Quality	0.9383 ± 0.0013	0.2716 ± 0.0150	0.2734 ± 0.0124
Kaon PID	0.9364 ± 0.0013	0.2498 ± 0.0294	0.2453 ± 0.0193
NN>-0.8	0.9820 ± 0.0008	0.6797 ± 0.0612	0.6545 ± 0.0424
Total Efficiency	0.4009 ± 0.0040	———	———

Table 4.1: *Summary of* ϕK_S^0 *efficiencies.*

4.3 Event Selection: ϕK^0_L

Aside from the K^0_L selection, the ϕK^0_L and ϕK^0_S candidate selection are very similar.

- **Preselection**: a B candidate is formed by producing an $h^+h^-K^0_L$ candidate where $h = \pi$, or K. After contraining the candidates mass to the B mass, we cut on the $\Delta E < 150\,\mathrm{MeV}$.

- **Lists**: tracks are taken from the **GoodTracksVeryLoose** list and K^0_L candidates are taken from the **EMCKlDefault** and **IFRKlDefault** list.

- **Charged track requirements**:

  - Number of hits in the DCH ≥ 12.

  - $p_T(\mathrm{track}) > 0.1\,\mathrm{GeV/c^2}$.

  The above track quality cuts make the list used in the analysis equivalent to **GoodTracksLoose**.

- **PID**: The K^+K^- candidates must identify as kaons, but not pions.

- $\boldsymbol{K^0_L}$ **requirements**: We require that the K^0_L is on either the **EMCKlTight** or **IFRKlTight** list. In addition, we have constructed dedicated K^0_L neural nets for EMC candidates. For validation, we refer to [50], which uses $J/\psi K^0_L$ events. We use the following variables:

  - E_{cal}: Energy deposited in the Calorimeter

- Lat: Lateral shape parameter of the EMC shower
- S1S9: Energy of the most energetic crystal divided by the energy sum of the 3x3 crystal block with the most energetic crystal in it's center.
- S9S25: The energy sum of the 3x3 crystal block with the most energetic crystal in its center, divided by the energy sum of the 5x5 crystal block with the most energetic crystal in its center.
- $|z42|$: absolute value of the Zernike moment 4,2 in the EMC shower
- $|z20|$: absolute value of the Zernike moment 2,0 in the EMC shower
- $|p_\theta|$: Cosine of the theta of the momentum of the K_L^0 as detected in the EMC
- $cos(\theta(\text{EMC,IFR})_{\text{best}})$: The smallest angles of all the angles between the measured momentum of a given EMC K_L^0 candidate, and every IFR K_L^0 candidate on the IfrLoose list and in the same event.
- N_{crystals}: Number of crystals in the EMC cluster

- **Dalitz plot (DP)**: The same DP cuts applied for ϕK_S^0 are applied for ϕK_L^0, namely:
  - $1.01 < m(\phi \to \pi^+\pi^-) < 1.03\,\text{GeV}/c^2$ (*cf.* left hand plot in Fig. 5.2).
  - No cut on the decay angle is applied. It is used in the likelihood fit.
- **Kinematic cuts**: Since there is no energy information available for the K_L^0, we conduct a kinematic fit to the ϕK_L^0 candidate contraining the decay to the nominal B mass, thus losing m_{ES} as a discriminating variable.

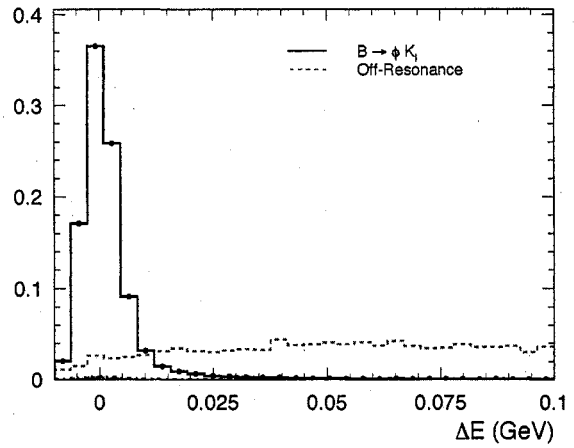

Fig. 4.3.— *ΔE for correctly reconstructed ϕK_L^0 signal (solid with dots), misreconstructed signal (shaded area), and continuum events from off-resonance data (dashed). The arrows indicate the requirements applied.*

  - **ΔE**, the difference between the reconstructed B energy in the CM, and the nominal CM beam energy is required to be within the interval $-0.01 < \Delta E < 0.05\,\mathrm{GeV}$. The ΔE distribution for single MC and continuum is shown in Figure 4.3.

- **Δt**: Vertexing is done using just the charged tracks from the ϕ candidate. We require $|\Delta t| < 20$ ps and $\sigma_{\Delta t} < 2.5$ ps, where $\sigma_{\Delta t}$ is the Δt per-event error.

- **MVA**: We use a five-variable Neural Network for which the output is required to be larger than -0.4 (Fig. 4.4). In addition to the four of the variables used for the ϕK_S^0 MVA, we input the missing momentum, which is simply the momentums of all tracks and neutrals but the K_L^0 subtracted from the momentum of the beam. See Section 4.4 for more details.

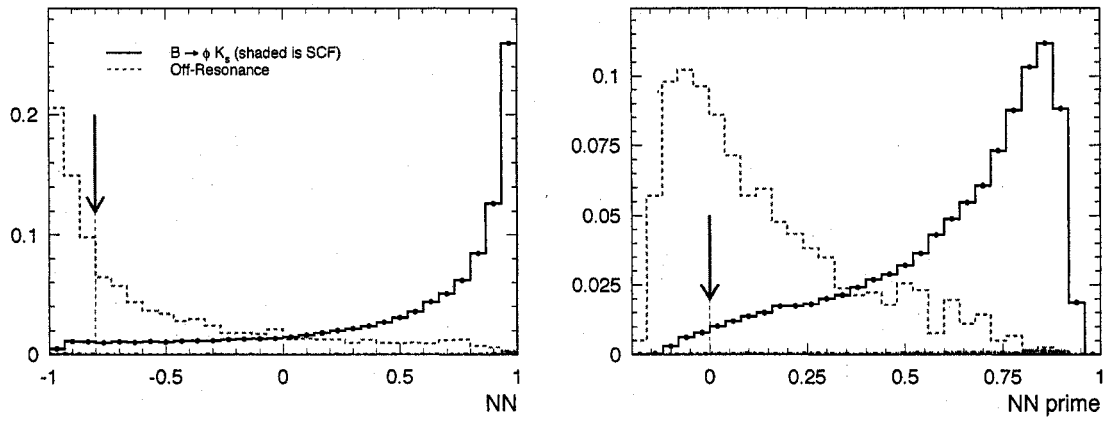

Fig. 4.4.— *Distributions of* NN *and* NN′ *for correctly reconstructed* ϕK_L^0 *signal (solid with dots), misreconstructed signal (shaded area), and continuum events from off-resonance data (dashed). The arrows indicate the requirements applied.*

Of the signal events passing the above criteria, 6.4% have more than one candidate. We select the best candidate as follows:

- An EMC candidate is automatically preferred over an IFR candidate, e.g. if there is even one EMC candidate then we choose it.
- Among EMC candidates, we choose the one with the most energy deposited in the calorimeter.
- Among IFR candidates, we choose the one with the most layers in the IFR.

Looking at MC events, we see that $\sim$ 22.5% are not truth matched. In almost all of these events, it is the K_L^0 identification that is incorrect. However, since we don't use (or even have) the energy of the K_L^0 "track", instead using only it's direction, all of the distributions for these SCF events (e.g. ΔE) look similar to the truth matched distributions. Because of this, we do not separate the signal into TM and

SCF components when we do the likelihood fit.

The selection efficiencies are summarized in Table 4.2. A total of 10343 events from remain after all cuts.

Cuts	Relative Efficiencies		
	$\epsilon^{\mathrm{MC}}_{\phi K^0_L}$	$\epsilon^{\mathrm{data}}_{\mathrm{on-res}}$	$\epsilon^{\mathrm{data}}_{\mathrm{off-res}}$
Preselection	0.6449 ± 0.0032	———	———
Track Quality	0.9133 ± 0.0015	0.9358 ± 0.0003	0.9364 ± 0.0001
$-0.01 < \Delta E < 0.05$	0.9319 ± 0.0013	0.3690 ± 0.0012	0.3690 ± 0.0004
$1.03 > m_{K^+K^-} > 1.01$	0.8901 ± 0.0005	0.2801 ± 0.0017	0.2888 ± 0.0006
$\lvert\Delta t\rvert$ <20 ps	0.9795 ± 0.0007	0.9354 ± 0.0007	0.9304 ± 0.0002
$\sigma(\Delta t)$ <2.5 ps	0.9442 ± 0.0013	0.9310 ± 0.0007	0.9295 ± 0.0002
K^0_L Quality	0.6871 ± 0.0041	0.2875 ± 0.0008	0.0723 ± 0.0003
Kaon PID	0.8834 ± 0.0025	0.2063 ± 0.0060	0.2027 ± 0.020
NN>-0.4	0.9140 ± 0.0022	0.2860 ± 0.0162	0.2768 ± 0.0057
Total Efficiency	0.2445 ± 0.0067	———	———

Table 4.2: *Summary of ϕK^0_L efficiencies.*

4.4 Multivariate Continuum Suppression

Optimization and training of the MVAs has been performed using off-resonance data contained in the signal region to reduce residual correlations of the NN with the kinematic variables used in the ML fit (see also the detailed description in Appendix D of Ref. [35]). Optimization was performed separately for ϕK^0_S and ϕK^0_L.

Two MVA techniques, a linear Fisher discriminant (FI) [36], and a non-linear Neural Network (NN) [37], have been studied. The latter is a *MultiLayerPerceptron* Neural Network with the following architecture:

- number of input variables: $N_{\rm var} = 4$ (5 for ϕK^0_L);
- number of output classes: 2 (signal and background);
- number of layers: 4 (input, output & 2 hidden layers);
- number of neurons per layer: $N_{\rm var}$, $N_{\rm var} - 1$, $N_{\rm var} - 2$, 2;
- number of training cycles: ca. 5000;
- size of the training samples: 10000 signal MC events and 10000 off-resonance data events.

In addition to these four variables, the ϕK^0_L NN uses a fifth variable, the magnitude of the missing momentum, defined as the momentums of all tracks and neutrals but the K^0_L subtracted from the momentum of the beam.:

For the ϕK^0_S selection, we observe similar performance for both MVAs, which indicates that the correlations between the discriminating variables are mainly linear.

However for the ϕK^0_L selection there is a clear improvement for the NN over the Fisher. We use the NN technique for both the ϕK^0_S and ϕK^0_L analysis.

To simplify an empirical fit of the NN output shape for continuum events, one can transform the MVA:

$$\mathrm{NN} \longrightarrow \mathrm{NN}' \equiv 1 - \arccos\left(\mathrm{NN} + \mathrm{offset}\right) / \arccos\left(\mathrm{NN}_{cut} + \mathrm{offset}\right) \ , \qquad (4.1)$$

where we use and offset of 0.001.

4.5 B-Related Background

4.5.1 B-Background in ϕK^0_S

Due to the small width of the ϕ, the majority of potential B-related background events are cut away by the $m(K^+K^-)$ cut. We have studied generic $B\overline{B}$ MC and several exclusive modes and concluded that there is no significant B-background contamination from 2-body or 4-body charmless modes. Two 4-body modes that have the potential to contaminate the sample, $B^0 \to \phi K^* \to K^+K^-K_s\pi^0$ and $B^+ \to \phi K^{+*} \to K^+K^-K_s\pi^+$, are each removed by the tight ΔE cut. The branching ratios for these two modes were taken from the *BABAR* analysis described in Ref. [51] and the decays were conservatively assumed to be 100% longitudinal. Less than 1 event from these modes is expected to pass all cuts.

Decays to the same final state as the signal ($K^+K^-K^0_S$) can be extremely important since they will be indistinguishable from ϕK^0_S in the discriminating variables and they will also interfere with the signal. Of particular importance are the S-wave components from non-resonant $K^+K^-K^0_S$, $B^0 \to f_0K^0_S$, or higher f_x resonances since these have opposite *CP* and will dilute the S and C measurements.

The *BABAR* measurement for the inclusive $K^+K^-K_s$ branching fraction, excluding ϕK_s, is $10.3 \pm 1.8 \times 10^{-6}$ [52]. The selection efficiency of non-resonant S-wave is $\epsilon = 0.0004$ and we expect less than one non-resonant event to pass our selection.

A more serious concern is the f_0K^0 mode. In this thesis, we measure $B^0 \to$

$f_0(\to \pi^+\pi^-)K^0_S$ decays to have a branching fraction of

$$\mathcal{B}(B^0 \to f_0 K^0) \times \mathcal{B}(f_0 \to \pi^+\pi^-) \;=\; (6.0 \pm 0.9 \pm 1.3) \times 10^{-6}$$

and a mass and width of

$$\begin{aligned} m_{f_0} &= (980.6 \pm 4.1 \pm 0.5 \pm 4.0)\,\mathrm{MeV}/c^2\,, \\ \Gamma_{f_0} &= (43^{+12}_{-9} \pm 3 \pm 9)\,\mathrm{MeV}/c^2\,. \end{aligned}$$

We estimate the selection efficiency by using $B^0 \to f_0(\to K^+K^-)K^0_S$ MC to obtain the efficiency of the selection, estimated to be ~ 0.06. From isospin arguments, the branching fraction for $f_0 \to K^+K^-$ is expected to be

$$(K\overline{K}) = \frac{3}{4} \cdot (\pi\pi) \quad \Longrightarrow \quad (K^+K^-) = 4 \cdot (K^0_S K^0_S) = \frac{9}{16} \cdot (\pi^+\pi^-) = \frac{9}{8} \cdot (\pi^0\pi^0)\;. \quad (4.2)$$

Based on this estimate, we expect ~ 8.5 $B^0 \to f_0(\to K^+K^-)K^0_S$ events in our final data sample. Since the Q2B approximation assumes nothing interferes with the ϕ, we include the effect of interference on S and C as a systematic.

In addition to $B^0 \to f_0 K^0_S$, there may be higher $B^0 \to f_x K^0_S$ decays which contaminate the ϕ. These decays have not yet been unmeasured and we will not include them explicitly in our B-background model.

A summary of the efficiencies and number of events expected in the final sample is given in Table 4.3.

4.5.2 B-Background in ϕK^0_L

Along with more continuum background, the ϕK^0_L sample also has much more B-related background than ϕK^0_S. In addition to the $f_0 K^0$ background, calculated the same way as above, there is background from ϕK^* modes where the K^* decays to $K^0_L\pi$.

We take these branching ratios [51] and assume that the decays have a longitudinally polarized fraction equal to $0.52 \pm 0.05 \pm 0.02$ from *BABAR* measurement[53]. There is also combinatoric B-background which we estimate from generic charged- and neutral-$B\overline{B}$ Monte Carlo. In the $B^0 \to f_0 K^0_S$ analysis we observe that the number of generic background events was overestimated by about a half (*cf.*Section 5.4), so we assign a 50% uncertainty to the expected number of generic events.

Each different source of B-Background are separated into classes (see Table 4.3) and fixed in the likelihood fit described in Section 4.6.

4.6 Building the Likelihood

The likelihood is similar to that described in Section 3.8. We perform a single likelihood fit, where we assume that $S_{K^0_S} = -S_{K^0_L}$.

Class	Id	Mode	BR $[10^{-6}]$	Efficiency (%)	$N_{\rm exp}$
		ϕK_S^0 B-Backgrounds			
0	5179	$B^0 \to f_0(980)(\to K^+K^-)K_S^0(\to \pi^+\pi^-)$	1.2 ± 0.34	2.5 ± 0.02	6.8 ± 1.4
		ϕK_L^0 B-Backgrounds			
0	5180	$B^0 \to f_0(980)(\to K^+K^-)K_L^0$	1.7 ± 0.5	1.5	5.7 ± 1.2
1	3565	$B^0 \to \phi K^{0*} \to K_L\pi^0$	0.9 ± 0.1	13.5	12.6 ± 2.2
2	5181	$B^0 \to \phi K(1430)^0 \to K_L\pi^0$	0.5 ± 0.5	4.9	4.1 ± 4.4
3		Charged Charmed			275 ± 118
4		Neutral Charmed			84 ± 39

Table 4.3: *Classification of background from charged B and neutral B decays. The efficiencies are obtained from MC simulation. The expected number of events in the selected data sample correspond to an integrated on-resonance luminosity of* 207 fb^{-1} *(black diamond).*

4.7 Results

4.7.1 Nominal *CP* and Yield Fit

The results of the full *CP* fit after convergence for the ϕK^0_S and ϕK^0_L selected on-resonance data samples are given in Tables 4.4 and 4.5. Also included in the table are the global correlation coefficients. Table 4.6 summarizes the results of the ϕK^0_S and ϕK^0_L separate fits and the result from the combined fit, which constrains that S and C from both modes be the same. We do not include the fitted values for all variables in the combined fit since they do not change significantly from the parameters in the separate fits. The correlations coefficients from the combined fits for a selection of parameters are given in Table 4.7.

4.7.2 Fit Quality

Figure 4.6 shows the distribution of likelihood values from toys thrown with the values from the fit to data. For both the ϕK^0_S and ϕK^0_L fits there is good agreement.

The fit quality can be further illustrated by means of the likelihood projections[33,35]

$$r^c_i = \frac{(1-f^c_{\rm SCF})\mathcal{P}^c_{fK_S-{\rm TM},i} + f^c_{\rm SCF}\mathcal{P}^c_{fK_S-{\rm SCF},i}}{(1-f^c_{\rm SCF})\mathcal{P}^c_{fK_S-{\rm TM},i} + f^c_{\rm SCF}\mathcal{P}^c_{fK_S-{\rm SCF},i} + \left(1+q_{{\rm tag},i}A^c_{q\bar{q},{\rm tag}}\right)\mathcal{P}^c_{q\bar{q},i}}\,, \qquad (4.3)$$

for all selected events $i = 1, \ldots, \sum_c N_c$ in tagging category c. The data distribution for a given mode is compared to the sum of the various signal and background contributions of the likelihood fit, obtained from high statistics toy integration and normalized to the fit results given in Table 4.4 for ϕK^0_S and 4.5 for ϕK^0_L. The corresponding

Parameter	Fit Value	Global Corr.
Signal Parameters:		
$N_{\phi K^0_S}$	90.9 ± 11.0	0.114
S	0.287 ± 0.349	0.212
C	0.067 ± 0.296	0.218
$\langle m_{\rm ES} \rangle$ (GeV/c^2)	5.27967 ± 0.00033	0.050
$\langle \Delta E \rangle$ (GeV)	(0.780 ± 2.350) $\times 10^{-3}$	0.042
Continuum Parameters:		
$N_{q\bar{q}}$ (Lepton)	20.0 ± 4.5	0.020
$N_{q\bar{q}}$ (Kaon I)	243.3 ± 15.7	0.030
$N_{q\bar{q}}$ (Kaon II)	387.3 ± 19.8	0.029
$N_{q\bar{q}}$ (Inclusive)	409.9 ± 20.3	0.023
$N_{q\bar{q}}$ (Untagged)	924.4 ± 30.5	0.033

Table 4.4: *Results and global correlation coefficients for selected floating parameters in the ϕK^0_S on-resonance fit after convergence.*

Parameter	Fit Value	Global Corr.
Signal Parameters:		
$N_{\phi K^0_L}$	96.5 ± 20.2	0.362
S	0.922 ± 0.531	0.569
C	0.414 ± 0.519	0.564
$\langle \Delta E \rangle$ (GeV)	(-0.315 ± 0.857) $\times 10^{-3}$	0.171
Continuum Parameters:		
$N_{q\bar{q}}$ (Lepton)	97.5 ± 11.2	0.077
$N_{q\bar{q}}$ (Kaon I)	1057.4 ± 33.4	0.065
$N_{q\bar{q}}$ (Kaon II)	1833.4 ± 43.8	0.070
$N_{q\bar{q}}$ (Inclusive)	1793.1 ± 43.4	0.080
$N_{q\bar{q}}$ (Untagged)	5091.9 ± 72.6	0.084

Table 4.5: *Results and global correlation coefficients for selected floating parameters for the ϕK^0_L on-resonance fit after convergence.*

	ϕK_S^0 Only	ϕK_L^0 Only	Combined ϕK_S^0 ϕK_L^0
$N_{\phi K_S^0}$	90.9 ± 11.0	—	90.9 ± 11.0
$N_{\phi K_L^0}$	—	96.5 ± 20.2	98.7 ± 20.1
S	0.287 ± 0.349	0.922 ± 0.531	0.475 ± 0.277
C	0.067 ± 0.296	0.414 ± 0.519	0.158 ± 0.253

Table 4.6: *Fit results from the ϕK_S^0 only, ϕK_L^0 only, and combined fits.*

projections are displayed in Figs. 4.7 and 4.8. Agreement is observed between data and the toy MC expectation for both signal modes.

Likelihood projections of the various discriminating variables in the fit are shown in Figures 4.9 and 4.10. The likelihood ratio cut that was chosen to make these plots was arbitrary and is meant to just show the compatibility of the model to data.

Figure 4.9 shows M_{es}, ΔE, $\cos\theta_H$, and NN projections for the ϕK_S^0 shapes while 4.10 shows the corresponding plots for the ϕK_L^0 shapes. There appears to be good agreement between the model and the data in all cases.

Using the total efficiency from Table 4.1, the ϕK_S^0 fitted yield corresponds to a branching ratio of:

$$BR(B^0 \to \phi K^0)_{\phi K_S^0} = 6.1 \pm 0.7 \times 10^{-6}, \tag{4.4}$$

and from the ϕK_L^0 fitted yield:

$$BR(B^0 \to \phi K^0)_{\phi K_L^0} = 7.1 \pm 1.5 \times 10^{-6}, \tag{4.5}$$

where the errors are statistical only, compared to the published *BABAR*[56] value of

$$BR(B^0 \to \phi K^0)_{BAD742} = 8.4 \pm 1.4 \times 10^{-6}, \tag{4.6}$$

whose error includes statistical and sytematic uncertainties.

	$N_{\phi K^0_S}$	$N_{\phi K^0_L}$	S	C
$N_{\phi K^0_S}$	1	0.001	-0.022	0.013
$N_{\phi K^0_L}$	-	1	-0.044	0.032
S	-	-	1	-0.232

Table 4.7: *Correlation coefficients found between selected parameters in the final combined $\phi K^0_S/\phi K^0_L$ on-resonance fit.*

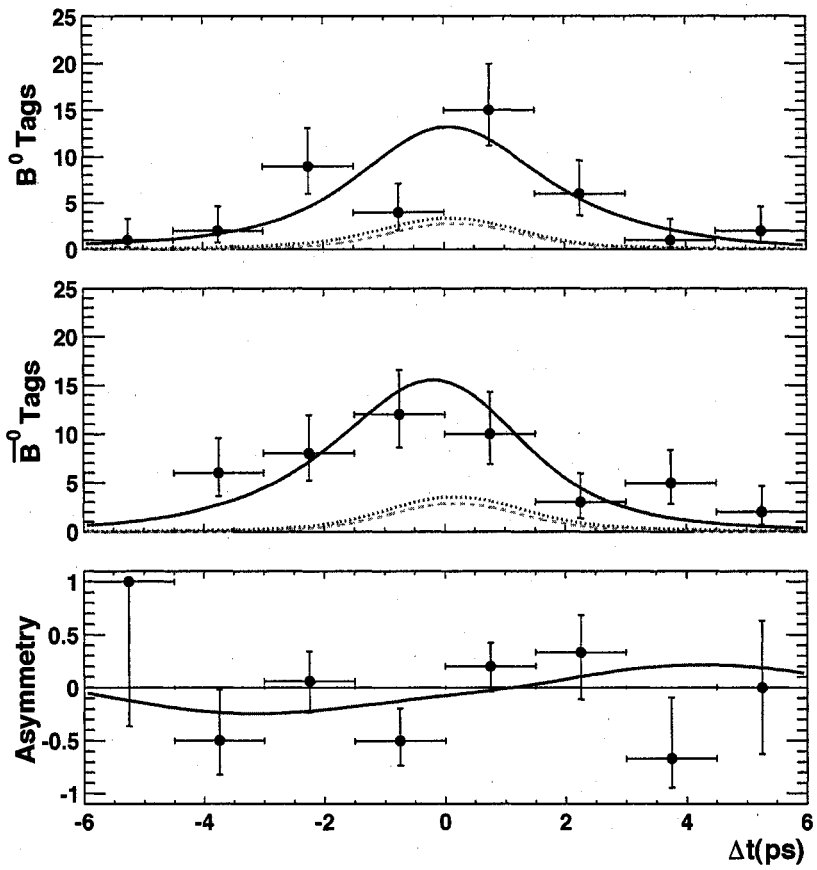

Fig. 4.5.— *Time distributions for events selected to enhance the ϕK^0 signal tagged as $B^0_{\rm tag}$ (upper), $\overline{B}^0_{\rm tag}$ (center) and the time-dependent asymmetry between $B^0_{\rm tag}$ and $\overline{B}^0_{\rm tag}$ (lower). The solid curve is a likelihood projection of the fit result. The dashed line is the continuum-background contribution and the dotted line is the sum of continuum and B-background contributions. The points are onpeak data.*

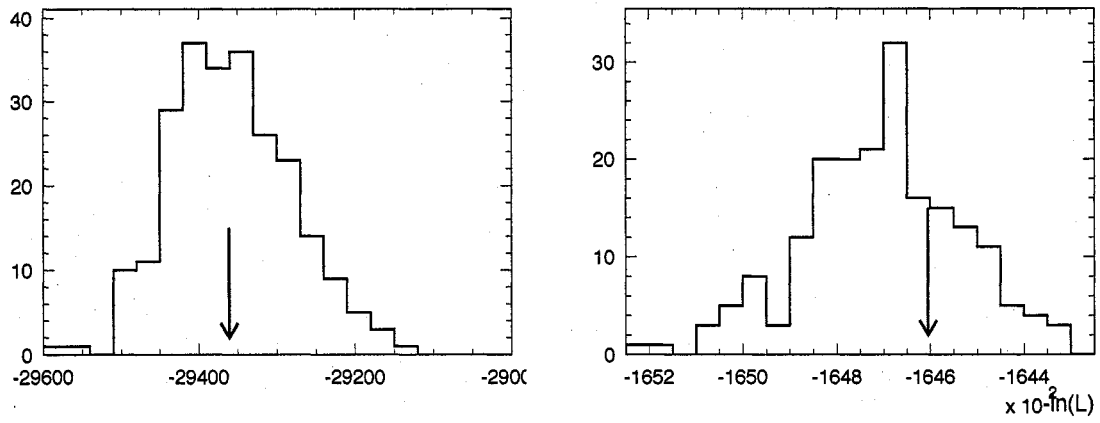

Fig. 4.6.— *The* $-\ln\mathcal{L}$ *distribution from toy fits for* ϕK_S^0 *(left) and* ϕK_L^0 *(right) only. The blue arrow corresponds tot the* $-\ln\mathcal{L}$ *value from the onpeak data fit.*

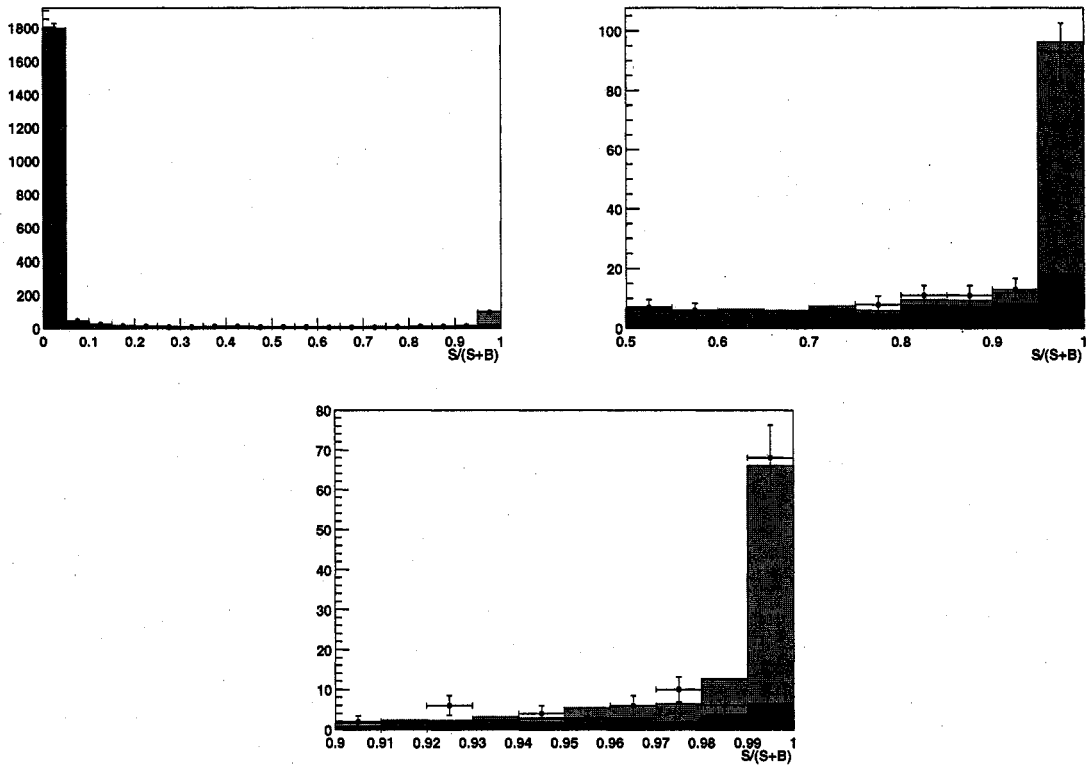

Fig. 4.7.— *Distributions of the ratio of S/S+B likelihoods (4.3) for ϕK_s^0 data and toy MC expectation, with different zooms into the signal region. The high statistics toy MC distributions are normalized to the fit results given in Table 4.4. The red shows the distribution from continuum events, the gray from B-Backgrounds and the tan from signal.*

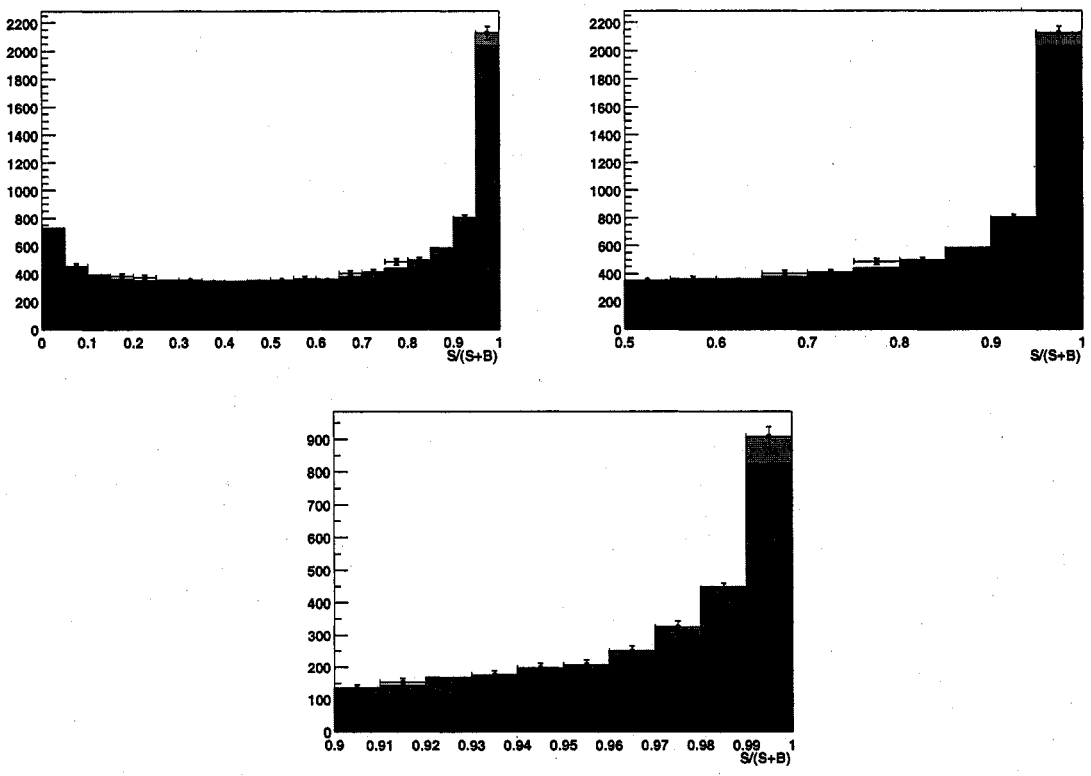

Fig. 4.8.— *Distributions of ratio of S/S+B likelihoods (4.3) for ϕK^0_L data and toy MC expectation, with different zooms into the signal region. The high statistics toy MC distributions are normalized to the fit results given in Table 4.5. The red shows the distribution from continuum events, the gray from B-Backgrounds and the tan from signal.*

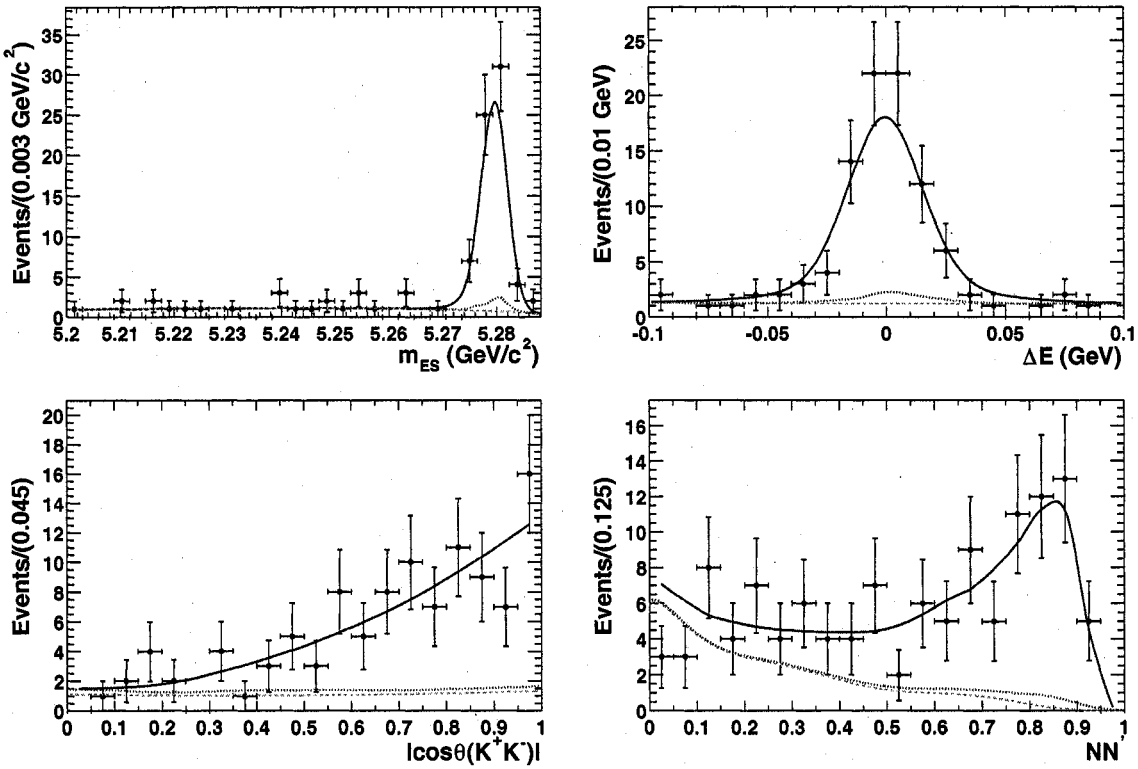

Fig. 4.9.— *Distributions of the discriminating variables after a cut on the likelihood (calculated from all variables except the one plotted) from the ϕK^0_S fit. The solid curve is a likelihood projection of the fit result. The dashed line is the continuum-background contribution and the dotted line is the sum of continuum and B-background contributions. The points are onpeak data.*

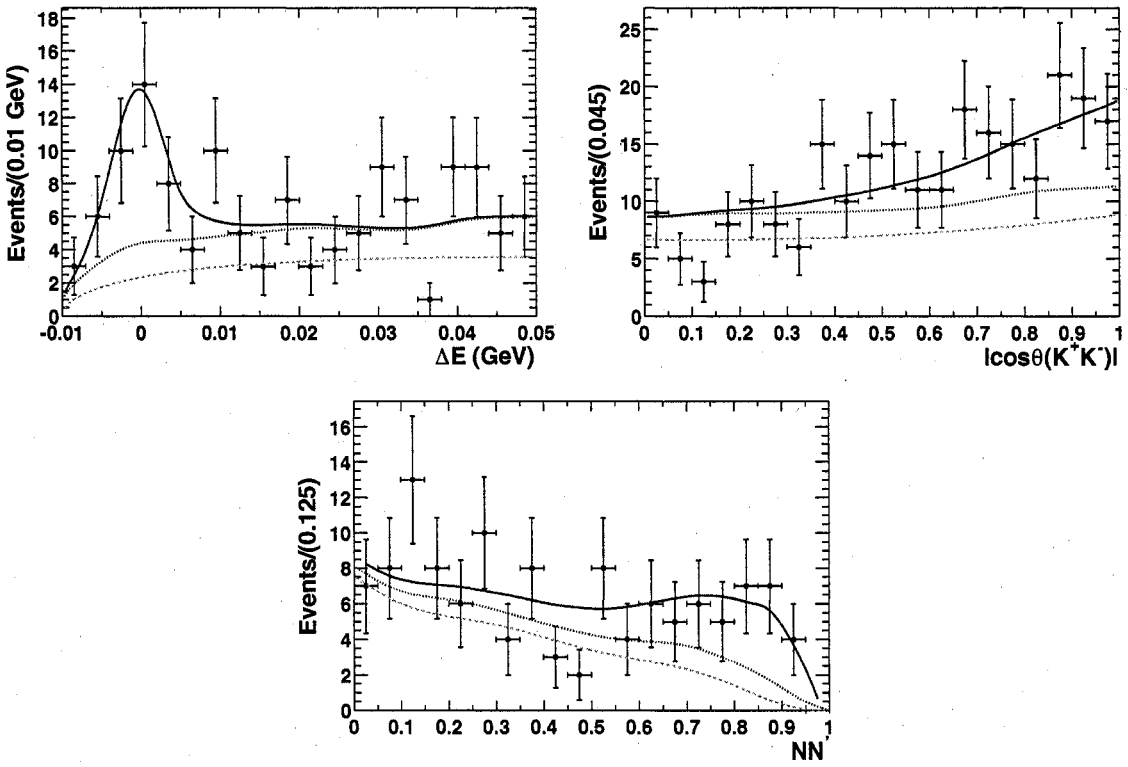

Fig. 4.10.— *Distributions of the discriminating variables after a cut on the likelihood (calculated from all variables except the one plotted) from the ϕK^0_L fit. The solid curve is a likelihood projection of the fit result. The dashed line is the continuum-background contribution and the dotted line is the sum of continuum and B-background contributions. The points are onpeak data.*

4.8 Systematic Uncertainties

The systematic uncertainties are summarized in Table 4.8. The methods we used to obtain these are summarized below.

4.8.1 Likelihood Fit

- τ **and** Δm The values of the B lifetime and the mass difference were fixed in the fit to the values from the 2002 PDG. They are varied within 1 σ to obtain the systematic error in S and C.

- **Fitting procedure:** The `RhoPiTools` toolkit has been extensively debugged in the various $B \to \rho\pi$ analyses[35,57–60]. For the present analysis, we have performed fit validations with the use of toy Monte Carlo samples samples. The fit model has been tested by means of fits to mixtures of high statistics ϕK^0_S SP5 Monte Carlo samples. and off-resonance events, and by performing fits to embedded Monte Carlo samples that contain the signal and background components determined with the nominal fit to on-resonance data. The differences between fit and generated values, added quadratically to the statistical errors of these validation studies, are assigned as systematic errors.

- $m_{\rm ES}$ **and** ΔE **PDFs:** for the continuum, the ξ parameter of the Argus function and the slope and second order coefficients of the ΔE polynomial are free varying parameters in the fit, so that their statistical uncertainties are properly propagated among the fit parameters. No additional systematic errors are assigned to the $m_{\rm ES}$ and ΔE continuum parameterizations.

For signal however, even if the mean values $\langle m_{\rm ES}\rangle$ and $\langle \Delta E\rangle$ of the PDFs are floating parameters in the fit, the impact of the fixed widths and possible shape uncertainties in the Monte Carlo parameters has to be studied. This is achieved by smearing the signal PDFs according to the differences found between data and SP5 in fully reconstructed $B^0 \to D^-\pi^+$ decays. For ϕK^0_S, they are selected by cutting the narrow mass band $1.85 < m_{-0} < 1.88\,{\rm GeV}/c^2$ out of the $\pi^+\pi^- K^0_S$ Dalitz plot, and by requiring NN > 0.4. We find 1252 $D^-\pi^+$ events with a purity of 96%. With the exception of the core mean (which, we recall, is a free parameter in the fit), we observe agreement between data and SP5 within the statistical uncertainties.

For ϕK^0_S, scale factors derived from the observed width (resolution) ratio of data to SP5 are applied to the PDFs of ΔE and $m_{\rm ES}$, and the fit is repeated to obtain the associated systematics. We find scale factors of 0.87 ± 0.02 (core) and 0.95 ± 0.15 (tail) (double Gaussian fit with relative fraction fixed to SP5 value) for ΔE, and 1.01 ± 0.04 for $m_{\rm ES}$ (single Gaussian fit).

For ϕK^0_L, ref [50] validates their ΔE shape using $J/\psi K^0_L$ data. They find an error on $\sigma(S) = 0.023$ and $\sigma(C) = 0.016$. We use these errors.

- **MVA PDF:** For the continuum, the NN′ PDF is extracted from the nominal data fit by adjusting a polynomial with four free parameters to it. For the signal, fully reconstructed $B^0 \to D^-\pi^+$ decays are used to determine a correction function for the MC distribution. For ϕK^0_L, ref [50] validates ther NN shape using $J/\psi K^0_L$ data. They find $\sigma(S) = 0.018$ and $\sigma(C) = 0.018$. We use these errors.

- **Signal Δt and Tagging**

The Δt resolution parameters were fixed to the values found from the BReco sample. The tagging fractions for the different categories as well as the mistag rates were also taken from BReco. All of these parameters were varied by $\pm$ 1 σ for systematics.

4.8.2 B-Backgrounds

All B-background yields are varied $\pm$ 1 sigma (errors given in Table 4.3) and the change in fitted parameters are taken as the systematic error. In addition, the *CP* parameters for each mode are varied with in their physical ranges (or, in the case of $f_0(980)K^0$, within their measured errors).

4.8.3 Q2B Approximation

In order to estimate the systematic due to ignoring interference effects between the ϕ and f_0, we used a dedicated toy MC generator to produce events with arbitrary amplitudes and unlimited statistics but which neglects effects from detector acceptance and resolution. For more information on this approach, see Section 5.8.5.

We generate many samples of ϕK^0_S and $B^0 \to f_0 K^0_S$ in the ratio of 2.4:1 (from their measured braching ratios) with the appropiate weak phases (assumed to be $\sin 2\beta$) and a random strong phase between them. We take as the systematic error as the spread in the resulting S and C distributions. We use the ϕ mass and decay angle in the ML fit so that the restriction to the Q2B Dalitz region is in effect tighter than the Q2B Dalitz cuts given in Section 4.2. Since the ML fit is not integrated into this generator study, we mimick this effect by applying the reinforced requirement $|\cos\theta(\pi^+\pi^-)| > 0.7$.

4.8.4 Doubly-Cabibbo-Suppressed B Decays

The systematic uncertainties due to interference between the doubly-Cabibbo-suppressed (DCS) $\bar{b} \to \bar{u}c\bar{d}$ amplitude with the Cabibbo-favored $b \to c\bar{u}d$ amplitude for tag-side B decays are discussed in great detail in Ref. [61]. The associated errors on S and C have been obtained from simulation by varying freely all relevant strong phases. We use the numbers corresponding to the $B^0 \to \pi^+\pi^-$ toy MC analysis [61] (they are similar to the corresponding numbers in $B^0 \to \rho^\pm\pi^\mp$).

Source	S	C
Δm_d, τ_B^0	0.003	0.003
Δt signal model	0.005	0.007
B-background yields	0.010	0.005
B-background CP parameters	0.015	0.043
$m_{\rm ES}$ and ΔE resolution	0.026	0.017
Embedded toy biases	0.071	0.040
Tag-side DCS decays	0.013	0.037
Signal tagging fractions	0.002	0.002
Mistag biases	0.006	0.005
Mistag probabilities	0.006	0.005
Q2B approximation	0.054	0.056
PDFs: NN′ shape	0.018	0.018
Total	0.098	0.093

Table 4.8: *Summary of systematic uncertainties on S, C, for the combined $\phi K_S^0/\phi K_L^0$ analysis as described in the text. The total systematic errors are obtained by adding up in quadrature all individual sources.*

4.9 Conclusions

We have presented the measurement of *CP*-violating asymmetries in $B^0 \to \phi K_S^0$ and $B^0 \to \phi K_l$ decays, using a quasi-2-body approximation. The results are obtained from a data sample of 227×10^6 $\Upsilon(4S) \to B\overline{B}$ decays collected during the Runs 1-4 (Black Diamond). From a time-dependent maximum likelihood fit we find 98.9 ± 11.0 ϕK_S^0 and 98.7 ± 20.1 ϕK_L^0 signal events. We measure the mixing-induced *CP* violation parameter $S = 0.48 \pm 0.28 \pm 0.10$ and the direct *CP* violation parameter $C = 0.16 \pm 0.25 \pm 0.09$. The measured value for S is in agreement with the world average $\sin 2\beta = 0.68 \pm 0.03$ [30] of the charmonium modes.

Chapter 5

$f_0 K_S^0$ Experimental Analysis

5.1 Overview

The f_0 resonance is much wider than the ϕ, which increases the amount of continuum and B-background when studying the mode $B^0 \to f_0 K_S^0$ relative to $B^0 \to \phi K_S^0$. Additionally, the $B^0 \to \pi^+\pi^- K_S^0$ dalitz plane is complicated by many different resonances. (See Section 5.2.) Finally, the width and, to a lesser degree, the mass of the f_0 is not well know (see Table 1.1.) Other than the need to consider a larger number of B-background modes, the $f_0 K_S^0$ analysis is very similar to the ϕK_S^0 analysis, with the major difference being that the mass of the f_0 candidate is included as a discriminating variable in the final maximum likelihood fit, unlike the mass of the ϕ candidate. We use a relativistic Breit-Wigner to parameterize the f_0 lineshape, although studies show our data set is not large enough to allow us to be sensitive to the exact parameterization used. The mass and width are floating parameters in the final fit.

We quote a branching ratio of $B^0 \to f_0(\to \pi^+\pi^-)K_S^0$ for a fit to a smaller

data sample of (122.56 ± 0.68) million $B\overline{B}$ pairs, and find the measurement to be systematics-dominated for reasons related to the Q2B approach (see Section 5.8.5.) We measure the *CP* parameters S and C for a larger data set of approximately 209 million BB^0 pairs. Since $\eta_{f_0 K^0_S} = +1$, we expect that $S_{\phi K^0_S} = -\sin 2\beta$.

5.2 Modeling the $B^0 \to \pi^+\pi^- K^0_S$ Decay Amplitude

The full $B^0 \to \pi^+\pi^- K^0_S$ decay amplitude consists of a coherent sum of amplitudes belonging to various intermediate states, of which some are long-lived, but most are strongly decaying resonances. A summary of the resonant charmless Q2B modes contributing to the $\pi^+\pi^- K^0_S$ Dalitz plot is given in Table 5.1.

The quasi-2-body approximation consists of reducing the decay kinematics of the kinematically allowed region in the Dalitz plot to bands or cross-bands, which (usually) are dominated by a single resonance, with more or less significant cross feed from other resonances through interference. The Dalitz plot of the decay $B^0 \to \pi^+\pi^- K^0_S$ is plotted in Fig. 5.1. The shaded area gives the kinematically allowed region. Shown are truth-matched and misreconstructed $B^0 \to f_0 K^0_S$ MC events, where misreconstruction mostly occurs due to combinatorial background. They accumulate at the Dalitz corners, where one of the f_0 decay pions has little momentum. Also shown is the narrow f_0-mass band we restrict the Dalitz plot to in the Q2B approximation (*cf.* Section 5.3). The selection efficiencies used in the present analysis (*cf.* Section 5.3) are obtained with the use of MC. All other contributions (B-related backgrounds, continuum background) to the likelihood model are added incoherently, *i.e.*, only considering the squares of their transition amplitudes.

Q2B mode	Resonance parameters: Mass (MeV/c^2)	Width (MeV/c^2)	Spin	Ref.
$\rho^0(770)K_S^0$	~ 773	~ 147	1	[62]
$\rho^0(1450)K_S^0$	~ 1410	$300 \sim 500$	1	[62]
$\rho^0(1700)K_S^0$	~ 1748	~ 235	1	[62]
$\sigma(500)K_S^0$	~ 478	324	0	[63]
$f_0(980)K_S^0$	975 ± 3	44 ± 3	0	[64]
$f_0(1370)K_S^0$	1434 ± 18	173 ± 32	0	[64]
$f_2(1270)K_S^0$	~ 1275	~ 185	2	[3]
$f_2'(1525)K_S^0$	~ 1525	~ 76	2	[3]
$K^*(892)\pi$	~ 892	~ 51	1	[3]
$K^*(1410)\pi$	~ 1414	~ 232	1	[3]
$K_0^*(1430)\pi$	~ 1412	~ 294	0	[3]
$K_2^*(1430)\pi$	~ 1426	~ 100	2	[3]
$K^*(1680)\pi$	~ 1717	~ 322	1	[3]

Table 5.1: *Quasi-2-body modes contributing to the $\pi^+\pi^-K_S^0$ Dalitz plot. Masses and widths quoted correspond to the Breit-Wigner parameterizations as defined in this note with the exception of the $\rho(770)$, for which the Gounaris-Sakurai parameterization is used [62]. Since statistics is low and the branching fractions for most of the Q2B modes are only fairly known or unknown, a precise knowledge of the resonance parameters is not required (we omit the errors for most of the parameters). The values for the ρ^0 resonances are obtained from e^+e^- annihilation data [62]. The f_0 parameters stem from the Dalitz plot analysis of $D_s^+ \to \pi^+\pi^-\pi^+$ decays [64], and the parameters of the other resonances are taken from Ref. [3].*

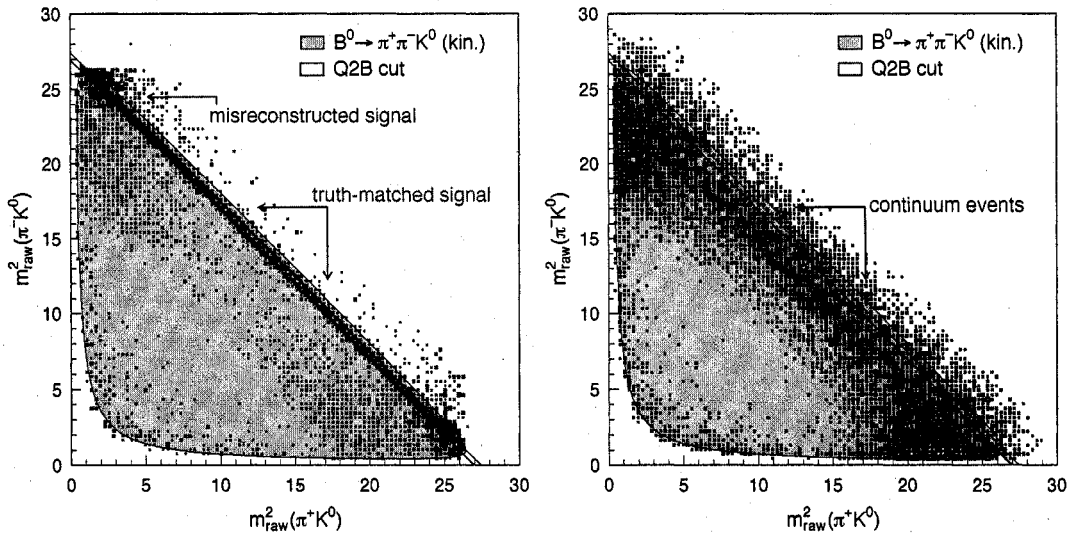

Fig. 5.1.— *Dalitz plots of the decay* $B^0 \to \pi^+\pi^- K_s^0$ *for signal (left) and continuum background (off-resonance events). The shaded area gives the kinematically allowed region. For the signal Dalitz plots, both truth-matched and misreconstructed* $B^0 \to f_0 K_s^0$ *MC events are shown. The latter accumulate at the Dalitz corners, where one of the* f_0 *decay pions has little momentum. Also shown is the narrow* f_0*-mass band we restrict the Dalitz plot to in the Q2B approximation.*

5.3 Event Selection

The main line of the $B^0 \to f_0 K^0_S$ event selection is similar to the one described in [35]. The candidate selection is straightforward and uses general Q2B rules.

- **Lists**: tracks are taken from the **GoodTracksVeryLoose** list and K^0_S candidates are taken from the **KsDefault** list (using tracks from the **ChargedTracks** list).

- **Charged track requirements**:

  - Number of hits in the DCH ≥ 12.

  - $p_T(\text{track}) > 0.1\,\text{GeV/c}^2$.

  The above track quality cuts make the list used in the analysis equivalent to **GoodTracksLoose**.

- **PID**: both tracks forming the f_0 candidate must fail the *tight* electron, proton and kaon flags of the standard Micro selectors. In addition, at least one track must fail the tight muon criterion. These requirements remove about 45% of the continuum background and 5% of the signal events.

- $\boldsymbol{K^0_S}$ **requirements**: the $K^0_S \to \pi^+\pi^-$ decay (the $K^0_S \to \pi^0\pi^0$ branch is ignored in the present analysis) is reconstructed from two oppositely charged tracks, without applying particle identification, fit to a common vertex. A candidate is required to have

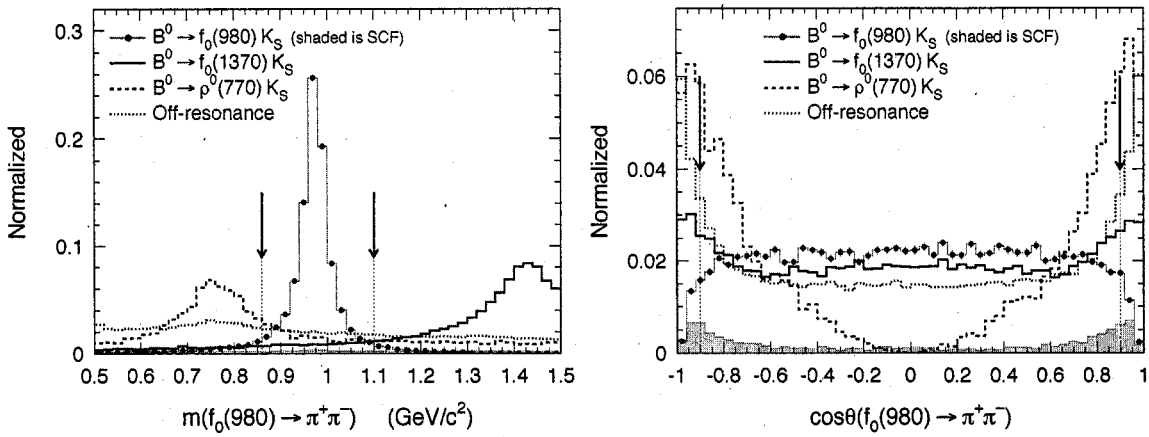

Fig. 5.2.— *Left: Reconstructed invariant mass of the $f_0 \to \pi^+\pi^-$ candidates for correctly reconstructed $B^0 \to f_0 K_S^0$ signal (dots with error bars), misreconstructed signal (shaded area), the background modes $B^0 \to f_0(1370)K_S^0$ (solid line), $\rho^0 K_S^0$ (dashed), and continuum events from off-resonance data (dotted). The arrows indicate the requirements applied. Right: decay angle distribution for the $f_0 \to \pi^+\pi^-$ candidates.*

  - a $\pi^+\pi^-$ invariant mass within $|m(\pi^+\pi^-) - m(K_S^0)| < 10\,\mathrm{MeV}/c^2 2$
  - a decay length significance $\ell(K_S^0)/\sigma_{\ell(K_S^0)} > 5$.
  - an opening angle α between the K_S^0 flight direction and the vector between the f_0 and the K_S^0 vertices of $\cos\alpha > 0.99$ ($\alpha < 8°$).

- **Dalitz plot (DP)**: The quasi-2-body approach consists of choosing a particular band in the Dalitz plot, which is determined by the presence of a f_0 resonance. Due to the close neighbourhood of the ρ^0 on the low mass side, and the $f_0(1370)$ on the high mass side, we apply tight mass requirements for the f_0 candidate:
  - $0.86 < m(f_0 \to \pi^+\pi^-) < 1.10\,\mathrm{GeV}/c^2$ (*cf.* left hand plot in Fig. 5.2).
  - and $|\cos\theta(f_0)| < 0.9$ for the f_0 decay angle, defined as the angle between

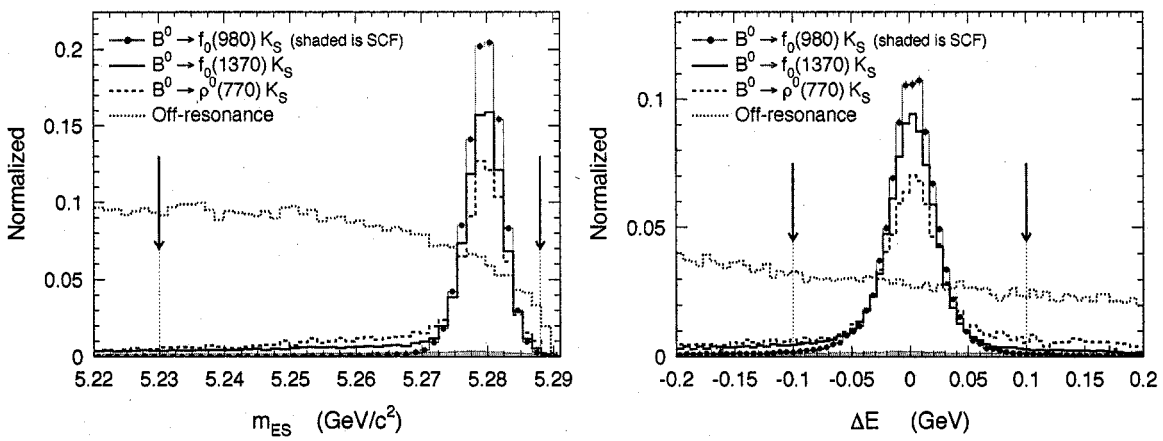

Fig. 5.3.— *Distributions of $m_{\rm ES}$ (left plot) and ΔE (right plot) for correctly reconstructed $B^0 \to f_0 K^0_S$ signal (dots with error bars), misreconstructed signal (shaded area), the background modes $B^0 \to f_0(1370) K^0_S$ (solid line), $\rho^0 K^0_S$ (dashed), and continuum events from off-resonance data (dotted). The arrows indicate the requirements applied.*

the positive pion in the f_0 center-of-mass and the f_0 flight direction in the laboratory frame (*cf.* right hand plot in Fig. 5.2).

The Dalitz plot requirements remove about 93% of the continuum background and 18% of the signal events.

- **Two-body veto**: no invariant mass veto is applied to remove two-body topologies.

- **Kinematic cuts**:

  - $\boldsymbol{m_{\rm ES}}$, the energy-substituted mass (3.2). We require $5.230 < m_{\rm ES} < 5.288$ GeV/c^2. See left hand plot in Fig. 5.3 for the signal and continuum distributions of $m_{\rm ES}$.

  - $\boldsymbol{\Delta E}$, the difference between the reconstructed B energy in the CM, and the nominal CM beam energy (3.3) is required to be within the interval $-0.1 < \Delta E < 0.1\,\mathrm{GeV}$. This relatively tight requirement removes about 75% of the continuum background and 12% of the signal events. It is applied to improve the rejection of misreconstructed events (self-cross-feed – SCF) hence increasing the efficiency of truth-matched (TM) events. Also, a tighter cut on ΔE simplifies the B-background treatment since less modes have to be considered in the likelihood model.

- $\boldsymbol{\Delta t}$: We require $|\Delta t| < 20$ ps and $\sigma_{\Delta t} < 2.5$ ps, where $\sigma_{\Delta t}$ is the Δt per-event error (see Ref. [35] for details on the vertexing algorithm used).

- **MVA**: a description of the dedicated continuum-fighting Multivariate Analyzer (MVA) is given in Section 5.3.2. We use a four-variable Neural Network for which the output is required to be larger than -0.8.

The selection efficiencies relative to the previous cut in the column, and the total selection efficiencies, for $B^0 \to f_0 K^0_S$ signal, off-resonance and on-resonance data are given in Table 5.2. The total MC efficiency includes K^0_S decays to final states other than $\pi^+\pi^-$. We give the corresponding $B^0 \to f_0 K^0_S(\to \pi^+\pi^-)$ efficiency in the last line. For the *CP* fit, we select a total of 12586 events, with a signal efficiency of approximately 39%. For the BR fit, we select a total of 7556 on-resonance events, with a signal efficiency of $(37.2 \pm 3.1)\%$.

Cuts	Relative Efficiencies		
	$B^0 \to f_0 K_s^0$ [SP5]	off-resonance	on-res. (2003)
Preselection	0.4579 ± 0.0029	-	-
Track Quality	0.9996 ± 0.0001	0.9986 ± 0.0000	0.9987 ± 0.0000
$\lvert\Delta E\rvert < 0.1\,\mathrm{GeV}$	0.8808 ± 0.0018	0.2481 ± 0.0006	0.2491 ± 0.0004
$5.230 < m_{\mathrm{ES}} < 5.288\,\mathrm{GeV}/c^2$	0.9822 ± 0.0006	0.4735 ± 0.0018	0.4643 ± 0.0011
$0.86 < m(f_0 \to \pi^+\pi^-) < 1.10\,\mathrm{GeV}/c^2$	0.8626 ± 0.0021	0.0803 ± 0.0009	0.0797 ± 0.0005
$\lvert\cos\theta(f_0)\rvert < 0.9$	0.9464 ± 0.0012	0.9038 ± 0.0034	0.9055 ± 0.0021
$\lvert\Delta t\rvert < 20\,\mathrm{ps}$	0.9936 ± 0.0004	0.9676 ± 0.0019	0.9701 ± 0.0011
$\sigma(\Delta t) < 2.5\,\mathrm{ps}$	0.9646 ± 0.0010	0.8957 ± 0.0038	0.9025 ± 0.0023
$K_s^0 \to \pi^+\pi^-$ mass and opening angle	0.9540 ± 0.0012	0.3508 ± 0.0094	0.3428 ± 0.0058
$\ell(K_s^0)/\sigma_{\ell(K_s^0)} > 5$	0.9827 ± 0.0007	0.8173 ± 0.0100	0.8204 ± 0.0062
Kaon Veto	0.9702 ± 0.0010	0.6245 ± 0.0190	0.6276 ± 0.0119
Electron, Muon, Proton Vetoes	0.9798 ± 0.0008	0.8717 ± 0.0092	0.8563 ± 0.0063
NN > -0.8	0.9760 ± 0.0010	0.5687 ± 0.0264	0.5816 ± 0.0165
Total SP5 Efficiency	0.2693 ± 0.0017	-	-
Total SP5 Efficiency (for $K_s^0 \to \pi^+\pi^-$)	0.3926 ± 0.0017	-	-

Table 5.2: *Selection efficiencies relative to the previous cut for uncorrected $B^0 \to f_0 K_s^0$ ($f_0 \to \pi^+\pi^-$ only) SP5 signal (including misreconstructed events), off-resonance and on-resonance (Run 3 only) data. The total SP5 MC efficiency includes K_s^0 decays to final states other than $\pi^+\pi^-$. We give the corresponding $B^0 \to f_0 K_s^0(\to \pi^+\pi^-)$ efficiency in the last line.*

5.3.1 Multiple Candidate Selection and Misreconstruction of Signal Events

Events with multiple B candidates passing the full selection occur in only 0.8% of the correctly reconstructed signal $B^0 \to f_0 K_s^0$ events, while 28.2% of the misreconstructed events have more than one selected B candidate. This criterion can be used to effectively reduce the number of misreconstructed events, but would create correlations between this variable and the Dalitz plot (decay angle). This would require a multi-dimensional treatment in the fit, which is to be avoided here.

To prevent biasing the PDFs of the discriminant variables that enter the ML fit, we apply the following criteria to select a single candidate:

(A) if the multiple candidates have different K^0_S, we choose the one with a reconstructed $\pi^+\pi^-$ mass closest to the nominal K^0_S mass;

(B) use random choice for events without multiple K^0_S.

The SCF fractions are tagging category dependent; their values for each category are:

Lepton	Kaon I	Kaon II	inclusive	untagged
1.0 ± 0.1	6.2 ± 0.4	3.9 ± 0.3	3.0 ± 0.2	6.4 ± 0.3

Fractions of misreconstructed events (in %).

5.3.2 Multivariate Continuum Suppression

Two MVA techniques, a linear Fisher discriminant (FI) [36], and a non-linear Neural Network (NN) [37], have been studied. The latter is a *MultiLayerPerceptron* Neural Network with the following architecture:

- number of input variables: $N_{\rm var} = 4$;
- number of output classes: 2 (signal and background;
- number of layers: 4 (input, output & 2 hidden layers);
- number of neurons per layer: $N_{\rm var}$, $N_{\rm var} - 1$, $N_{\rm var} - 2$, 2;
- number of training cycles: ca. 5000;
- size of the training samples: 10000 signal MC events and 10000 off-resonance data events.

To simplify an empirical fit of the NN output shape for continuum events, one can transform the MVA so that it is confined within $[-1, 1]$ after selection:

$$\mathrm{NN} \longrightarrow \mathrm{NN}' \equiv 1 - \arccos\left(\mathrm{NN} + \mathrm{offset}\right) , \tag{5.1}$$

where we use and offset of 0.001.

5.4 *B*-Related Background

We investigate the cross-feed from other B-decays into $B^0 \to f_0 K^0_S$ using Monte Carlo events. We use two different sets of MC, "SP5" corresponding to R12 data, and "SP6", corresponding to R14 data. The branching fraction fit, relies only on SP5 events, while the *CP* fit relies on a ratio of the amount of SP5 to SP6 that is approximately equal to our ratio of Runs 1-3 data to Run 4 data. The shapes between the two types of MC are very similar. We use only SP5 generic B MC. Note also that since the branching fraction is found using a smaller data set, the expected yields of the different B-background modes are of course smaller than for the fit of the larger data set which is used for the CP result.

The inclusive branching fraction $B^0 \to \pi^+\pi^- K^0_S$ has been measured by Belle and CLEO, with an average of $(23.4 \pm 3.3) \times 10^{-6}$ [30], and recently by *BABAR* who finds $(22.0 \pm 1.9 \pm 1.7) \times 10^{-6}$ [65], so that the new average is $\mathcal{B}(B^0 \to \pi^+\pi^- K^0_S) = (22.5 \pm 2.0) \times 10^{-6}$. We can make use of this measurement to obtain upper limits on possible non-resonant or exotic contributions, which may produce background to $f_0 K^0_S$.

Charmed neutral B meson decays into the $\pi^+\pi^- K^0_S$ final state can proceed via $D^-(\to K^0_S\pi^-)\pi^+$ for which the branching fraction (including the decay into $K^0_S\pi^-$)

has been measured to $(41.6 \pm 6.2) \times 10^{-6}$. This mode is not vetoed, but considered as an individual background class in the likelihood model, which is justified since it is long-lived and no interference with the signal occurs. It has signal-like ΔE, $m_{\rm ES}$ and NN distributions, but a very different decay angle and resonant mass distributions so that it is well distinguished from signal in the fit. It was found in the Dalitz analysis of $B^0 \to \pi^+\pi^-\pi^0$ decays [38] that using the PDG branching fraction of $B^0 \to D^-(\to \pi^-\pi^0)\pi^+$ overestimates significantly the number of events present in the on-resonance data sample events.We therefore decide to let the corresponding event yield free to vary in the fit. We have tested that this does not decrease the statistical accuracy of the signal observables (yield and *CP* parameters).

Other charmed background occurs from the decay $B^+ \to \overline{D}^0(\to K^0_S\pi^0)\pi^+$ for which the product branching fraction amounts to $(57.3 \pm 6.4) \times 10^{-6}$ [3]. Individual background classes are attributed in the fit to both of the above modes.

All other charmed B decays are treated inclusively, using generic Monte Carlo, in two dedicated classes in the B background fit model. We expect from from MC 97 (81 for the *CP* fit) events from neutral $b \to c$ decays, and 51 (167 for the *CP* fit) events from charged $b \to c$ decays in the selected sample. However, when leaving the contributions to these two classes free in the fit close to zero events are preferred in both cases. We conclude from this that the simulation may overestimate the $b \to c$ contribution and as a consequence use conservatively half of the predicted neutral and charged sample sizes in our likelihood model, and assign systematic uncertainties of 100% to these numbers. This assumption is validated by means of a fit with wide ΔE cut to increase the sensitivity of the fit to $b \to c$ background.

We find that only modes that produce a K^0_S in the final state contribute sig-

nificantly to the data sample after the candidate selection. Many other modes have been studied, however. The significant modes, along with their expected numbers of events, are given in Tables 4.3.

Mode	$\mathcal{B}(10^{-6})$	ϵ_{SP5} (%)	N_{expected}	Cl
$B^0 \to \rho^0 K_S^0$	$2.4 \pm 2.4*$	1.82	5.1 ± 5.1	0
$B^0 \to D^-(\to K_S^0\pi^-)\pi^+$	41.6 ± 6.2	0.78	37.4 ± 5.6	1
$B^0 \to \pi^- K^{*+}(\to K_S^0\pi^+)$	5.1 ± 1.3	0.52	3.1 ± 0.8	2
$B^0 \to (K_0^*(1430)\pi)^0$	14 ± 14	0.13	2.0 ± 2.0	3
$B^0 \to (K_2^*(1430)\pi)^0$	14 ± 14	0.15	2.3 ± 2.3	3
$B^0 \to (K^*(1680)\pi)^0$	14 ± 14	0.15	2.4 ± 2.4	3
$B^0 \to \rho^- K^{*+}(\to K_S^0\pi^+)$ [long]	$7.1 \pm 7.1*$	0.21	1.7 ± 1.7	4
$B^0 \to f_0(1370)K_S^0$	2.0 ± 2.0	1.91	4.40 ± 4.40	5
$B^+ \to \overline{D}^0(\to K_S^0\pi^0)\pi^+$	57.3 ± 6.4	0.22	14.2 ± 2.0	6
$B^+ \to \rho^+ K_S^0$	$2.9 \pm 2.9*$	0.64	2.1 ± 2.1	7
$B^+ \to \pi^+ K^{*0}(\to K_S^0\pi^0)$	1.5 ± 0.2	0.52	0.9 ± 0.1	7
$B^0 \to f_2(1270)(\to \pi^+\pi^-)K_S^0$	1.7 ± 1.7	2.06	4.3 ± 4.3	8
$B^0 \to \eta'(\to \rho\gamma)K_S^0(\to \pi^+\pi^-)$	6.6 ± 0.9	2.50	19.9 ± 2.6	9
generic B^+B^-			$51^\dagger$	11
generic $B^0\overline{B}^0$			$97^\dagger$	12

Table 5.3: *List of the significant B-background modes in the $f_0K_S^0$ BR fit. When measured, the branching fractions are taken from the HFAG 30. Note that if decay modes are explicated the branching fractions given are products of branching fractions. If no measurements are available, educated guesswork (modes denoted by an asterisk) is used to infer conservative branching fraction ranges. If the efficiencies are expected to be low, we normalize $\mathcal{B}$ to ad hoc 20 ± 20 as a probe for the number of events expected after selection. For $B \to VV$ modes with unknown polarization, we assume them to be fully longitudinally polarized with an uncertainty of* 100%. *The class-Id (Cl) gives the number used for the classification of the individual modes in the fit (see text).* †*: The number of events actually included in the fit is half this, with an uncertainty of* 100% *(see text.)*

5.5 $f_0 K_S^0$ Maximum Likelihood Fit

The likelihood model used for the $f_0 K_S^0$ BR and *CP* fits is identical, and is similar to the one described in Section 3.8. We use the mass of the f_0 candidate, $m(\pi^+\pi^-)$ as a discriminating variable in the fit.

To parameterize the signal distribution of $m(\pi^+\pi^-)$, we use a relativistic Breit-Wigner (RBW) resonance line shape and determine the model parameters $m_{f_0(980)}$ and $\Gamma^0_{f_0(980)}$ with the final fit to data.

Figure 5.4 shows on the left hand plot the reconstructed invariant mass of the selected SP5 $f_0 \to \pi^+\pi^-$ candidates (solid) compared with the SP5 truth (dashed). When fitting a scalar RBW to these masses one finds a width of $(44.8 \pm 0.4)\,\mathrm{MeV}/c^2$ for SP5 truth and $(46.7 \pm 0.4)\,\mathrm{MeV}/c^2$ for reconstructed events, with satisfying fit quality in both cases. The difference between reconstructed and generated f_0 mass for MC is plotted on the right hand side. The core resolution is found to be $3.1\,\mathrm{MeV}/c^2$, which is small compared to the intrinsic width of the f_0 resonance (to be divided by approximately a factor of 2.5 if compared with a core Gaussian resolution function). Due to the excellent resolution, it is unnecessary to move to a more involved model that takes into account the convolution of the RBW function with a resolution function for the detector response. We use the above scale factor of 0.959 ± 0.012 to correct the width that is determined by the fit. SCF events are parameterized with Keys PDFs [71].

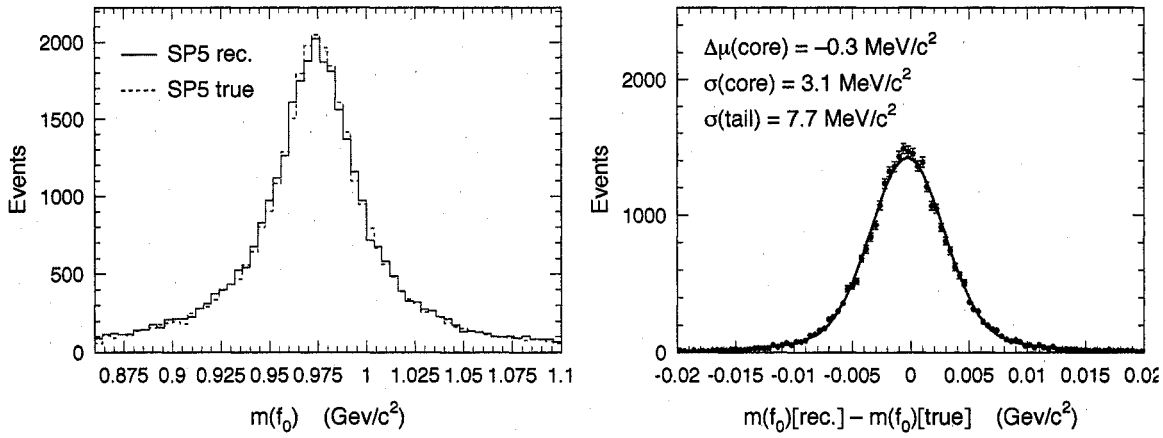

Fig. 5.4.— *Left: Reconstructed invariant mass of the selected* $f_0 \to \pi^+\pi^-$ *candidates (solid) compared with the SP5 truth (dashed). When fitting a scalar RBW to these masses one finds a width of* $(44.8 \pm 0.4)\,\mathrm{MeV}/c^2$ *for SP5 truth and* $(46.7 \pm 0.4)\,\mathrm{MeV}/c^2$ *for reconstructed events, with satisfying fit quality in both cases. Right: Difference between reconstructed and generated* f_0 *mass for SP5, and the results of a double Gaussian fit.*

Mode	$\mathcal{B}(10^{-6})$	ϵ_{sp5} (%)	ϵ_{sp6} (%)	N_{expected}	Cl
$B^0 \to \rho^0 K_S^0$	$2.4 \pm 2.4*$	4.72	4.46	22.96 ± 22.96	0
$B^0 \to D^-(\to K_S^0\pi^-)\pi^+$	41.6 ± 6.2	0.78	0.80	67.58 ± 10.02	1
$B^0 \to \pi^- K^{*+}(\to K_S^0\pi^+)$	5.1 ± 1.3	0.52	0.43	5.16 ± 1.32	2
$B^0 \to (K_0^*(1430)\pi)^0$	14 ± 14	0.13	0.09	3.24 ± 3.24	3
$B^0 \to (K_2^*(1430)\pi)^0$	14 ± 14	0.15	0.11	3.76 ± 3.76	3
$B^0 \to (K^*(1680)\pi)^0$	14 ± 14	0.15	0.12	3.98 ± 3.93	3
$B^0 \to \rho^- K^{*+}(\to K_S^0\pi^+)$ [long]	$7.1 \pm 7.1*$	0.21	0.18	2.93 ± 2.93	4
$B^0 \to f_0(1370)K_S^0$	2.0 ± 2.0	1.91	1.97	7.96 ± 7.96	5
$B^+ \to \overline{D}^0(\to K_S^0\pi^0)\pi^+$	57.3 ± 6.4	0.22	0.20	25.06 ± 2.80	6
$B^+ \to \rho^+ K_S^0$	$2.9 \pm 2.9*$	0.64	0.61	3.75 ± 3.75	7
$B^+ \to \pi^+ K^{*0}(\to K_S^0\pi^0)$	1.5 ± 0.2	0.52	0.51	2.46 ± 0.33	7
$B^0 \to f_2(1270)(\to \pi^+\pi^-)K_S^0$	1.7 ± 1.7	2.06	2.08	7.24 ± 7.24	8
$B^0 \to \eta'(\to \rho\gamma)K_S^0(\to \pi^+\pi^-)$	6.6 ± 0.9	2.50	2.45	33.74 ± 4.60	9
$B^0 \to \pi^+\pi^- K_S^0$ [nonres]	$0 - 9.3$	1.15	1.08	10.8 ± 10.8	10
generic B^+B^-			$81^\dagger$	11	
generic $B^0\overline{B}^0$			$167^\dagger$	12	

Table 5.4: *List of the B-background modes included in the final CP $f_0K_S^0$ ML fit where the number of expected events is scaled to the CP data set luminosity. When measured, the branching fractions are taken from the HFAG 30. Note that if decay modes are explicated the branching fractions given are products of branching fractions. If no measurements are available, educated guesswork (modes denoted by an asterisk) is used to infer conservative branching fraction ranges. The class-Id (Cl) gives the number used for the classification of the individual modes in the fit. The $N_{expected}$ is calculated from the luminosity weighted average of Runs 1-3 and Run 4. †: The number of events actually included in the fit is half this, with an uncertainty of* 100% *(see text.)*

5.6 Results from the BR fit

This section contains the results of the nominal BR fit to the 7556 selected on-resonance data as well as various consistency checks.

5.6.1 Nominal BR Fit Results

The results of the full fit after convergence (41 floating parameters) to the selected on-resonance data are given in Table 5.5. Also included in the table are the global correlation coefficients.

Using the difference between the $\ln(\mathcal{L})$ values obtained in the nominal fit and in a fit in which the signal yield is fixed to zero, and assuming a parabolic behaviour of $\ln(\mathcal{L})$ around its maximum, one can estimate the confidence level of obtaining the observed value for $N_{f_0 K^0_S}$ or less in the absence of a signal. We find $\Delta[\ln(\mathcal{L})] = 72.8$ corresponding to an observation of 12.1 standard deviations. This extimate does not take into account systematic uncertainties.

For the exclusive charmed background the fit converges at the value

$$N_{D^-(\to\pi^- K^0_S)\pi^+} = 39.3 \pm 9.2$$

which is in agreement with the 39.1 ± 5.8 events expected from the PDG branching fraction (*cf.* Tables 4.3-5.4). We conclude that the disagreement with the PDG expectation found in $B^0 \to \pi^+\pi^-\pi^0$ decays [38] has to be due to an overestimated $D^+ \to \pi^+\pi^0$ branching fraction, rather than a problem in the $B^0 \to D^-\pi^+$ branch of the decay chain.

Parameter	Fit Value	Global Corr.
Signal Parameters:		
$N_{f_0 K^0_S}$	93.6 ± 13.6	0.29
S	$-1.62 \,^{+\,0.56}_{-\,0.51}$	0.15
C	0.27 ± 0.36	0.20
$m_{f_0(980)}$ (MeV/c^2)	980.6 ± 4.1	0.10
$\Gamma^0_{f_0(980)}$ (MeV/c^2)	43 ± 11	0.29
$\langle m_{\rm ES} \rangle$ (GeV/c^2)	5.28090 ± 0.00038	0.16
$\langle \Delta E \rangle$ (GeV)	$(1.4 \pm 3.3) \times 10^{-3}$	0.15
B-background Parameters:		
$N_{D^-(\to \pi^- K^0_S)\pi^+}$	39.3 ± 9.2	0.15
Continuum Parameters:		
$N_{q\bar{q}}$ (Lepton)	50 ± 7	0.05
$N_{q\bar{q}}$ (Kaon I)	978 ± 31	0.03
$N_{q\bar{q}}$ (Kaon II)	1272 ± 36	0.04
$N_{q\bar{q}}$ (Inclusive)	1372 ± 37	0.04
$N_{q\bar{q}}$ (Untagged)	3629 ± 61	0.05

Table 5.5: *Results and global correlation coefficients for select floating parameters in the* $B^0 \to f_0 K^0_S$ *BR fit after convergence. Note that* $\Gamma^0_{f_0(980)}$ *has been rescaled by* 0.959 ± 0.012 *to correct for the detector resolution.*

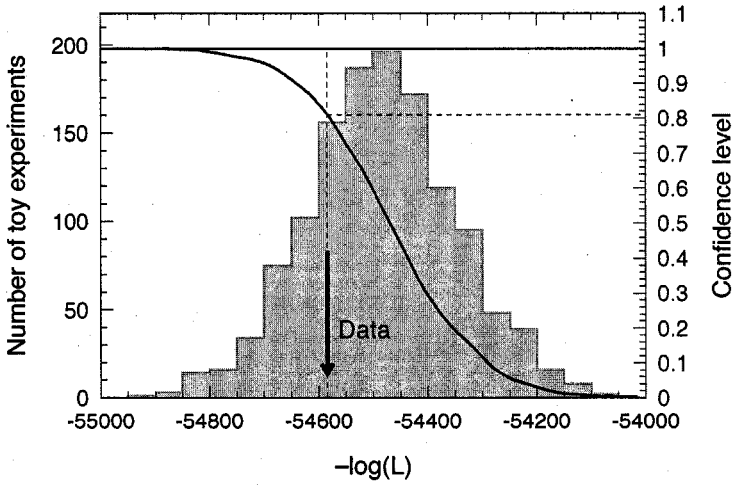

Fig. 5.5.— *Distribution of the quantity* $-\ln \mathcal{L}$ *for toy MC, generated according to the results in Table 5.5, and the value obtained in the fit (vertical line).*

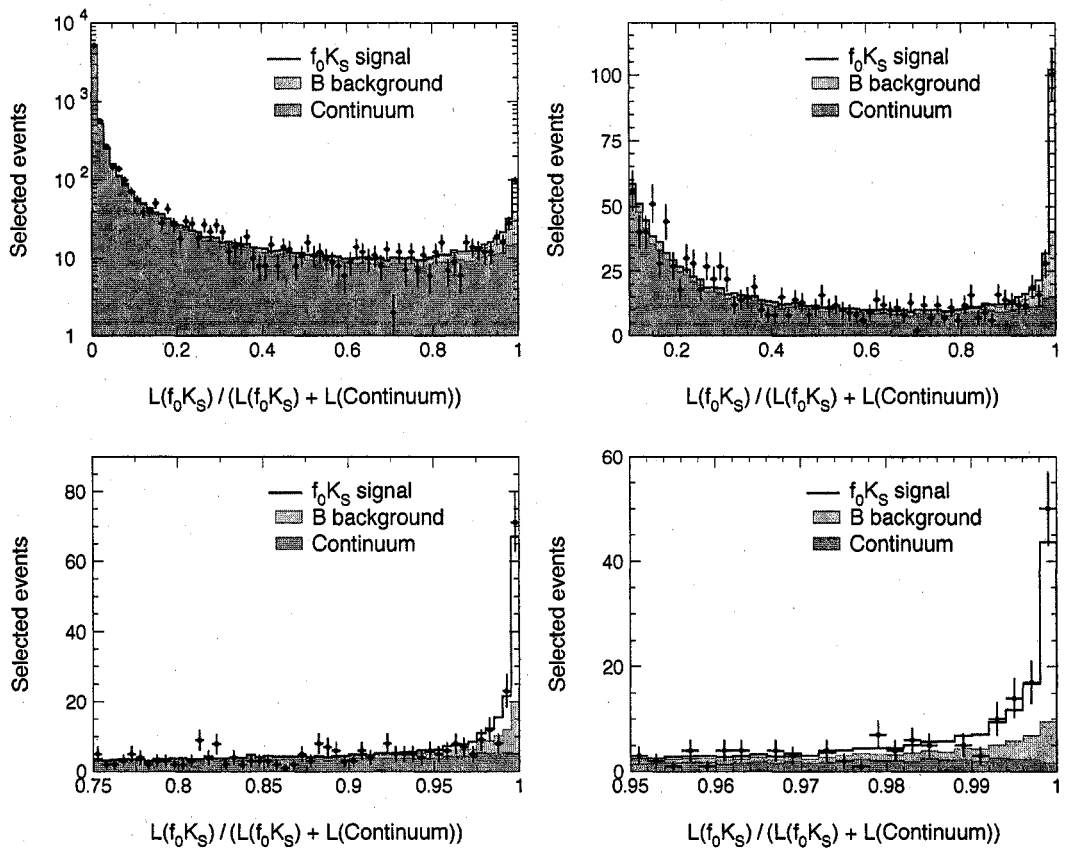

Fig. 5.6.— *Distributions of the likelihood projections (5.2) for data and toy MC expectation (upper left: logarithmic scale, other: linear scale with different zooms into the signal region) for the $f_0K_S^0$ BR fit. The high statistics toy MC distributions are normalized to the fit results given in Table 5.5. Note that these plots have been made with PAW, which does not show Poissonian errors.*

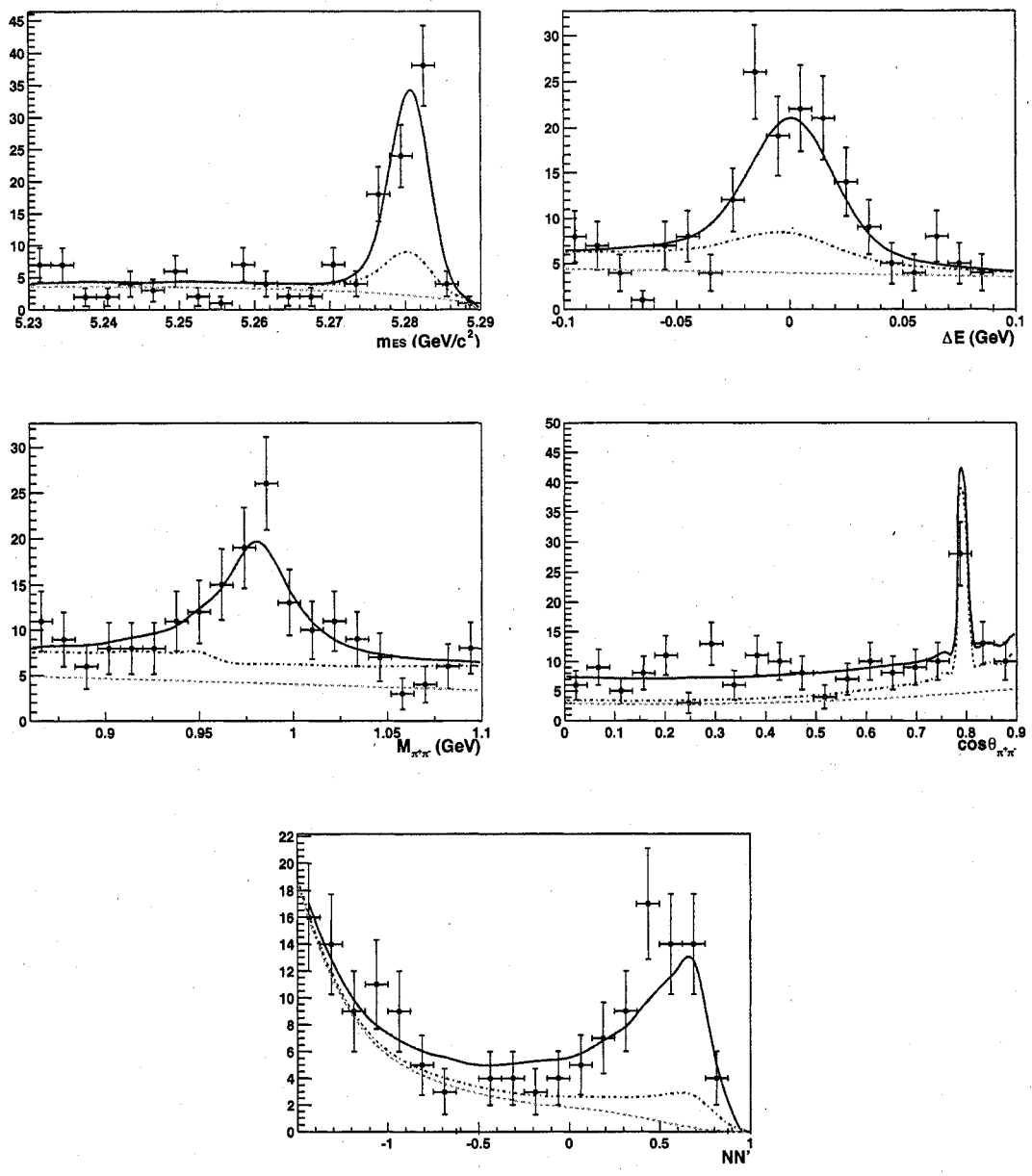

Fig. 5.7.— *Distributions of* $m_{\rm ES}$, ΔE *(upper plots),* $m(\pi^+\pi^-)$, $|\cos\theta(\pi^+\pi^-)|$ *(center plots) and* NN′ *(bottom plot) for samples enhanced in* $f_0K^0_s$ *signal using likelihood ratio cuts for the* $f_0K^0_s$ *BR fit. The solid curve represents a projection of the maximum likelihood fit result (*cf. *Table 5.5). The dashed curve represents the contribution from continuum events and the dotted line indicates the combined contributions from continuum and B-background events.*

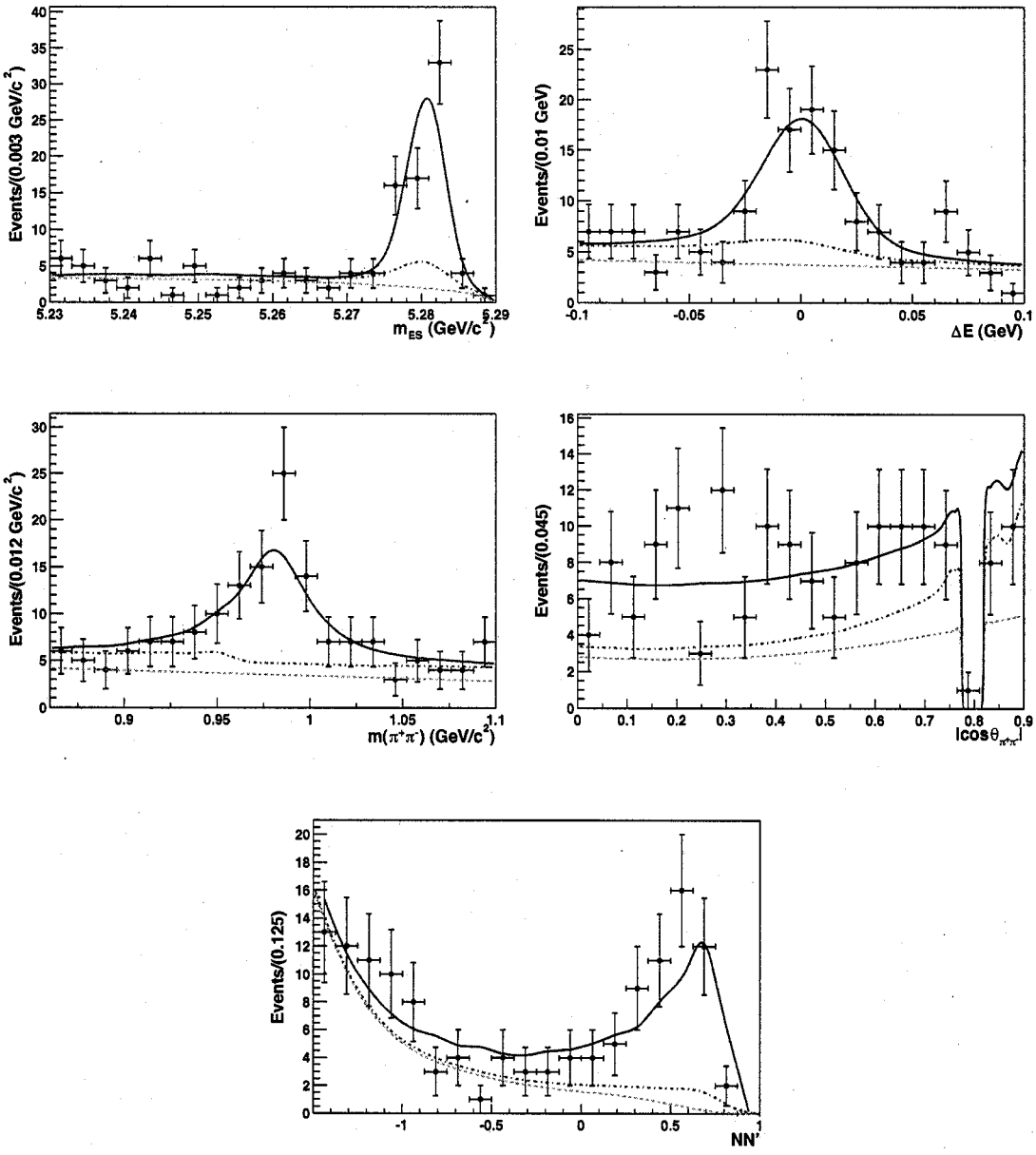

Fig. 5.8.— *Distributions of* $m_{\rm ES}$, ΔE *(upper plots),* $m(\pi^+\pi^-)$, $|\cos\theta(\pi^+\pi^-)|$ *(center plots) and* NN′ *(bottom plot) for samples enhanced in* $f_0K^0_S$ *signal using likelihood ratio cuts for the* $f_0K^0_S$ *BR fit. The solid curve represents a projection of the maximum likelihood fit result (*cf. *Table 5.5). The dashed curve represents the contribution from continuum events and the dotted line indicates the combined contributions from continuum and B-background events. The region* $0.77 < |\cos\theta(\pi^+\pi^-)| < 0.82$ *has been removed to suppress the contribution from* $D^-\pi^+$ *events.*

	$N_{f_0K^0_S}$	$N_{D^-(\to\pi^-K^0_S)\pi^+}$	S	C	$m_{f_0(980)}$	$\Gamma^0_{f_0(980)}$
$N_{f_0K^0_S}$	1	−0.068	−0.129	−0.118	0.004	0.236
$N_{D^-(\to\pi^-K^0_S)\pi^+}$	-	1	0.019	0.034	−0.001	−0.068
S	-	-	1	−0.007	0.014	−0.084
C	-	-	-	1	0.006	−0.158
$m_{f_0(980)}$	-	-	-	-	1	0.062

Table 5.6: *Correlation coefficients found between selected parameters in the* $B^0 \to f_0K^0_S$ *BR fit.*

5.6.2 Goodness-of-Fit and Likelihood Projections

The traditional test of the goodness-of-fit is shown in Fig. 5.5, where the distribution of $-\ln\mathcal{L}$ from toy MC is plotted along with the value observed in the fit. The confidence level that the data are described by our likelihood model amounts to 81%.

The fit quality can be further illustrated by means of the likelihood projections [33,35]

$$r_i^c = \frac{(1-f^c_{\rm SCF})\mathcal{P}^c_{fK_S-{\rm TM},i} + f^c_{\rm SCF}\mathcal{P}^c_{fK_S-{\rm SCF},i}}{(1-f^c_{\rm SCF})\mathcal{P}^c_{fK_S-{\rm TM},i} + f^c_{\rm SCF}\mathcal{P}^c_{fK_S-{\rm SCF},i} + \left(1+q_{{\rm tag},i}A^c_{q\bar{q},{\rm tag}}\right)\mathcal{P}^c_{q\bar{q},i}}\,, \qquad (5.2)$$

for all selected events $i = 1,\ldots,\sum_c N_c$ in tagging category c. The data distribution for a given mode is compared to the sum of the various signal and background contributions of the likelihood fit, obtained from high statistics toy integration and normalized to the fit results given in Table 5.5. The corresponding projections are displayed in Fig. 5.6. Agreement is observed between data and the toy MC expectation for both signal modes.

Figures 5.7 and 5.8 show the distributions of some of the discriminating variables used in the fit for data samples that have been signal-enhanced using a cut on the

likelihood ratio not containing the variable shown. An additional $|\cos\theta(\pi^+\pi^-)|$ cut has been applied in Fig. 5.8 to veto $D^-(\to K^0_S\pi^-)\pi^+$ events. The figures include projections of the fit result after correction for the efficiency of the likelihood ratio cuts. Agreement is found between data and the likelihood model.

5.6.3 Branching Fraction

We exploit the measured event yield to derive a branching fraction for the $B^0 \to f_0(980)(\to \pi^+\pi^-)K^0_S$ decay. Assuming $N_{B^0\bar{B}^0} = N_{B^+B^-} = 0.5 \cdot N_{B\bar{B}}$, we obtain the branching fraction from the relation

$$\mathcal{B}(B^0 \to f_0(980)(\to \pi^+\pi^-)K^0) = \frac{2\, N_{f_0 K^0_S}}{N_{B\bar{B}} \cdot \epsilon_{\mathrm{SP5}}(B^0 \to f_0(\to \pi^+\pi^-)K^0_S(\to \pi^+\pi^-)) \cdot C_\epsilon \cdot \mathcal{B}(K^0_S \to \pi^+\pi^-)}\,, \quad (5.3)$$

where $\epsilon_{\mathrm{SP5}}(B^0 \to f_0(\to \pi^+\pi^-)K^0_S(\to \pi^+\pi^-)) = 0.3926 \pm 0.0017$ (see Section 5.3), $\mathcal{B}(K^0_S \to \pi^+\pi^-) = 0.6860 \pm 0.0027$ [3], $C_\epsilon = 0.949 \pm 0.060$ is the efficiency correction factor that accounts for tracking and PID differences between data and SP5 (see Section 5.8.3), and where $N_{B\bar{B}} = (122.56 \pm 0.68) \times 10^6$ is the number of produced $B\overline{B}$ events used for this analysis (see Section 3.7). We find

$$\mathcal{B}(B^0 \to f_0(980)(\to \pi^+\pi^-)K^0) = (6.0 \pm 0.9(\mathrm{stat}) \pm 0.6(\mathrm{sys}) \pm 1.2(\mathrm{model})) \times 10^{-6}\,, \quad (5.4)$$

where the third error is due to the quasi-two body approximation. See Section 5.8 for a discussion of the systematic errors.

5.7 Results from the *CP* Fit

This section contains the results of the nominal *CP* fit to the 12586 selected on-resonance data as well as various consistency checks.

5.7.1 Nominal *CP* and Yield Fit

The results of the full *CP* fit after convergence (41 floating parameters) to the selected on-resonance data are given in Table 5.7. Also included in the table are the global correlation coefficients. No major correlations are found among the signal parameters, with the small exception of the anti-correlation between $N_{f_0 K^0_S}$ and $N_{D^-(\to\pi^- K^0_S)\pi^+}$, which however does not increase the error on the signal yield significantly.

For the exclusive charmed background the fit converges at the value

$$N_{D^-(\to\pi^- K^0_S)\pi^+} = 60.0 \pm 11.0$$

which is in agreement with the 58.4 ± 6.4 events expected from the PDG branching fraction (*cf.* Tables 4.3-5.4).

The improvement in error on S with respect to the BR fit is due mainly to the increased luminosity, but also due to one event with a large signal probability, and to the proximity of the measured S to the physical limit ($|S| \leq 1$).

5.7.2 Goodness-of-Fit and Likelihood Projections

The traditional test of the goodness-of-fit is shown in Fig. 5.9, where the distribution of $-\ln \mathcal{L}$ from toy MC is plotted along with the value observed in the fit.

Parameter	Fit Value	Global Corr.
Signal Parameters:		
$N_{f_0(980)}$	152.2 ± 18.4	0.291
S	-0.947 ± 0.277	0.229
C	-0.236 ± 0.306	0.227
$m_{f_0(980)}$ (MeV/c^2)	979.60 ± 4.63	0.190
$\Gamma_{f_0(980)}$ (MeV/c^2)	64.45 ± 16.49	0.343
$\langle m_{\rm ES} \rangle$ (GeV/c^2)	5.28074 ± 0.00031	0.139
$\langle \Delta E \rangle$ (GeV)	(-0.999 ± 2.723) $\times 10^{-3}$	0.155
B-background Parameters:		
$N_{D^-(\to\pi^- K^0_S)\pi^+}$	69.3 ± 12.3	0.1
Continuum Parameters:		
$N_{q\bar{q}}$ (Lepton)	80.3 ± 9.4	0.044
$N_{q\bar{q}}$ (Kaon I)	1661.1 ± 41.2	0.036
$N_{q\bar{q}}$ (Kaon II)	2104.9 ± 46.5	0.048
$N_{q\bar{q}}$ (Inclusive)	2293.2 ± 48.4	0.041
$N_{q\bar{q}}$ (Untagged)	5983.9 ± 78.1	0.051

Table 5.7: *Results and global correlation coefficients for the floating parameters in the* $B^0 \to f_0 K^0_S$ *CP fit after convergence. A fit allowing asymmetric errors found* $S = -0.95^{+0.32}_{-0.23}$. *The asymmetry in the error is due to the fitted value of* S *being so close to the boundary of its physical value.*

The fit quality can be further illustrated by means of the likelihood projections [33,35]

$$r_i^c = \frac{(1 - f_{\rm SCF}^c)\mathcal{P}_{fK_S-{\rm TM},i}^c + f_{\rm SCF}^c \mathcal{P}_{fK_S-{\rm SCF},i}^c}{(1 - f_{\rm SCF}^c)\mathcal{P}_{fK_S-{\rm TM},i}^c + f_{\rm SCF}^c \mathcal{P}_{fK_S-{\rm SCF},i}^c + \left(1 + q_{{\rm tag},i} A_{q\bar{q},{\rm tag}}^c\right)\mathcal{P}_{q\bar{q},i}^c} \,, \qquad (5.5)$$

for all selected events $i = 1, \ldots, \sum_c N_c$ in tagging category c. The data distribution for a given mode is compared to the sum of the various signal and background contributions of the likelihood fit, obtained from high statistics toy integration and normalized to the fit results given in Table 5.7. The corresponding projections are displayed in Fig. 5.10. Agreement is observed between data and the toy MC expectation for both signal modes.

Figure 5.11 show the distributions of some of the discriminating variables used in the fit for data samples that have been signal-enhanced using a cut on the likelihood ratio not containing the variable shown. A $|\cos\theta(\pi^+\pi^-)|$ cut has been applied in Fig. 5.11 to veto $D^-(\to K_S^0\pi^-)\pi^+$ events. The figures include projections of the fit result after correction for the efficiency of the likelihood ratio cuts. Agreement is found between data and the likelihood model. Figure 5.12 represents the corresponding signal-enhanced Δt distributions for events tagged as B^0 (upper plot) and as $\overline{B}^0$ (center plot). Also shown is the raw time-dependent asymmetry $A_{B^0_{\rm tag}/\overline{B}^0_{\rm tag}} = (N_{B^0_{\rm tag}} - N_{\overline{B}^0_{\rm tag}})/(N_{B^0_{\rm tag}} + N_{\overline{B}^0_{\rm tag}})$ for tagged events in all tagging categories (lower plot).

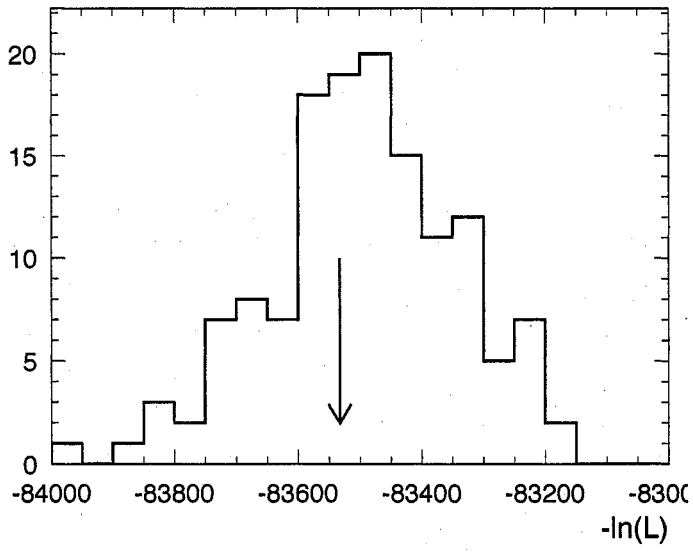

Fig. 5.9.— *Distribution of the quantity* $-\ln\mathcal{L}$ *for toy MC, generated according to the results in Table 5.7, and the value obtained in the* $f_0K_s^0$ *CP fit (vertical line).*

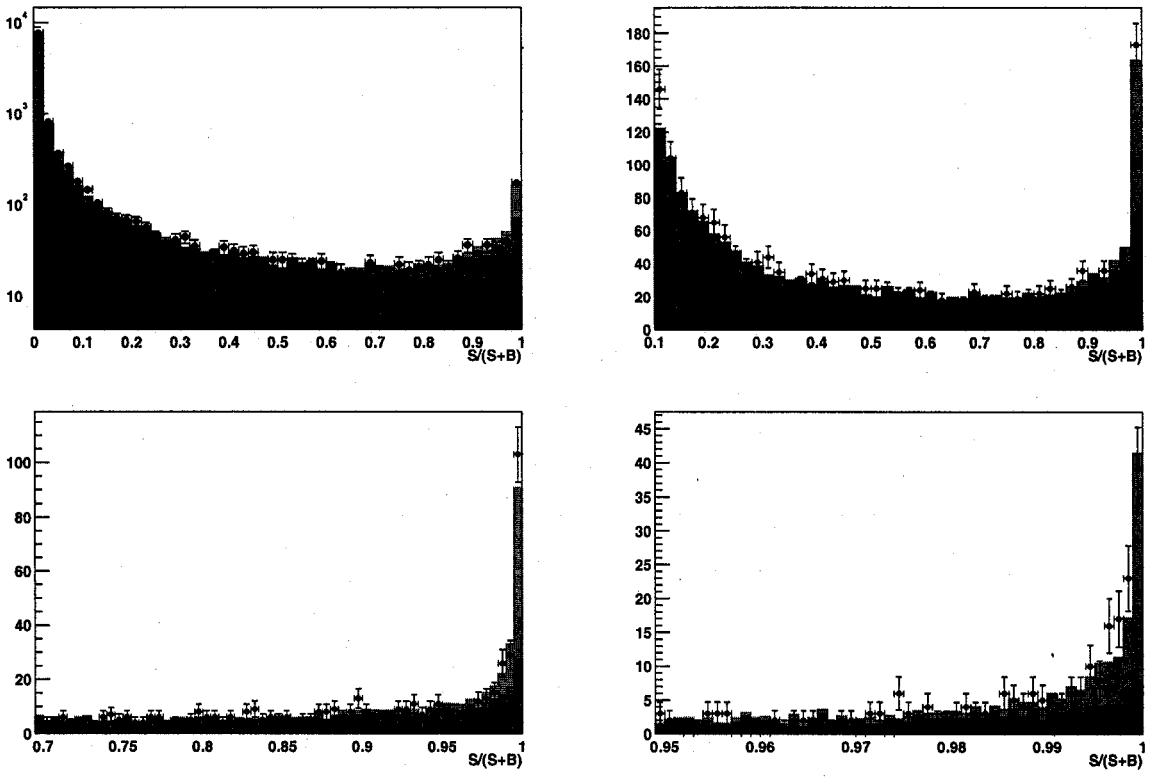

Fig. 5.10.— *Distributions of the likelihood projections (5.5) for data and toy MC expectation (upper left: logarithmic scale, other: linear scale with different zooms into the signal region) for the $f_0K_s^0$ CP fit. The high statistics toy MC distributions are normalized to the fit results given in Table 5.7. The red shows the distribution from continuum events, the gray from B-Backgrounds and the tan from signal.*

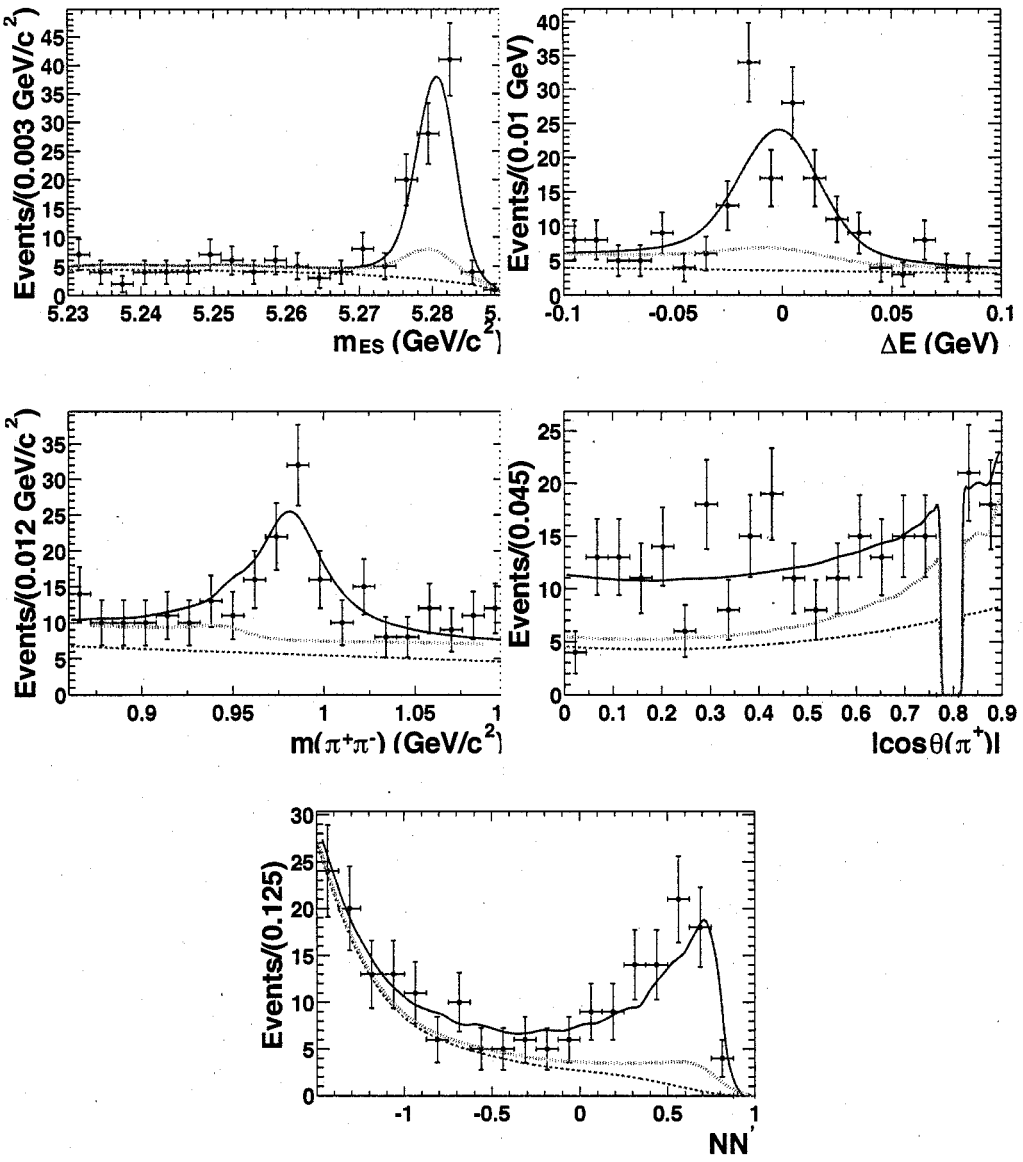

Fig. 5.11.— *Distributions of* $m_{\rm ES}$, ΔE *(upper plots),* $m(\pi^+\pi^-)$, $|\cos\theta(\pi^+\pi^-)|$ *(center plots) and* NN′ *(bottom plot) for samples enhanced in* $f_0K^0_S$ *signal using likelihood ratio cuts for the* $f_0K^0_S$ *CP fit. The solid curve represents a projection of the maximum likelihood fit result (*cf. *Table 5.7). The dashed curve represents the contribution from continuum events and the dotted line indicates the combined contributions from continuum and B-background events. The region* $0.77 < |\cos\theta(\pi^+\pi^-)| < 0.82$ *has been removed to suppress the contribution from* $D^-\pi^+$ *events.*

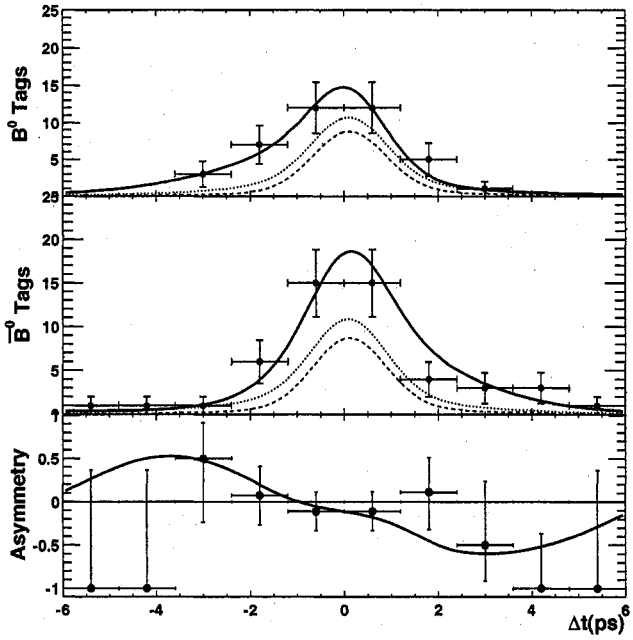

Fig. 5.12.— *Time distributions for events selected to enhance the $f_0 K^0_S$ signal tagged as $B^0_{\rm tag}$ (upper), $\overline{B}^0_{\rm tag}$ (center) and the time-dependent asymmetry between $B^0_{\rm tag}$ and $\overline{B}^0_{\rm tag}$ (lower). The solid curve is a likelihood projection of the fit result. The dashed line is the continuum-background contribution and the dotted line is the sum of continuum and B-background contributions.*

5.8 Study of Systematic Uncertainties

The systematic effects are summarized in Tables 5.10 and 5.9.

5.8.1 Resolution Function, Tagging and Signal Reconstruction

- **Δm_d and τ_{B^0}:** the systematic errors are obtained by varying incoherently the values of the B^0 oscillation frequency $\Delta m_d = (0.502 \pm 0.007)\,\mathrm{ps}^{-1}$ and the B lifetime $\tau_{B^0} = (1.536 \pm 0.014)\,\mathrm{ps}$ [30] within their experimental uncertainties.

- **Δt resolution function:** the six parameters used to describe the time distribution for continuum events are floated in the nominal fit to on-resonance data, so that their statistical uncertainties are properly propagated among the fit results. We do not account for additional systematics in the continuum shape parameterization.

  The parameters of the signal Δt resolution function are obtained from fits to fully reconstructed B decays [43]. We determine the associated systematics by varying incoherently each parameter of the resolution model (scale factors, biases, fraction of tails...) up and down by 1σ. Since the incoherent variation neglects the (mostly anti-)correlations that are present between the fit parameters it is a conservative procedure. The loss of precision is negligible with respect to the dominant statistical error on the measurement.

- **Tagging:** the tagging efficiencies, mistag rates and mistag biases are obtained from fits to fully reconstructed B decays to flavor eigenstates [43]. We determine

the associated systematics by varying incoherently each parameter up and down by 1σ of its experimental error.

- **Fraction of misreconstructed events:** misreconstructed events mainly arise due to combinatorial background in the presence of soft tracks (*cf.* Section 5.3.1) at the formation of a $f_0 \to \pi^+\pi^-$ candidate. Most of these events are removed by the $|\cos\theta(f_0)| < 0.9$ requirement. Since the fraction of misreconstructed events is small in the selected sample (3.6%), we do not attempt to validate the Monte Carlo prediction with control samples. Instead, we apply a conservative relative uncertainty of $\pm 25\%$ on $f^c_{\rm SCF}$, which is fully taken to be correlated among all tagging categories c.

  The fraction of misreconstructed events has been calibrated with control samples of fully reconstructed $B \to D\rho$ events in the Q2B *CP* analysis of $B^0 \to \rho^\pm\pi^\mp$ decays [35]. It was found to be in good agreement with the Monte Carlo prediction: $f_{\rm SCF}({\rm data - fitted})/{\rm f_{SCF}}({\rm MC - counted}) = 1.04 \pm 0.05$.

5.8.2 Likelihood Fit

- **Fitting procedure:** the `RhoPiTools` toolkit has been extensively debugged in the various $B \to \rho\pi$ analyses [35,57–60]. For the present analysis, we have performed fit validations with the use of toy Monte Carlo samples samples. The fit model has been tested by means of fits to mixtures of high statistics $B^0 \to f_0 K^0_S$ SP5 Monte Carlo samples and off-resonance events, and by performing fits to embedded Monte Carlo samples that contain the signal and background components determined with the nominal fit to on-resonance data. The differences

between fit and generated values, added quadratically to the statistical errors of these validation studies, are assigned as systematic errors.

- **$m_{\rm ES}$ and ΔE PDFs:** for the continuum, the ξ parameter of the Argus function and the slope and second order coefficients of the ΔE polynomial are free varying parameters in the fit, so that their statistical uncertainties are properly propagated among the fit parameters. No additional systematic errors are assigned to the $m_{\rm ES}$ and ΔE continuum parameterizations.

  For signal however, even if the mean values $\langle m_{\rm ES}\rangle$ and $\langle \Delta E\rangle$ of the PDFs are floating parameters in the fit, the impact of the fixed widths and possible shape uncertainties in the Monte Carlo parameters has to be studied. This is achieved by smearing the signal PDFs (truth-matched and SCF) according to the differences found between data and SP5 in fully reconstructed $B^0 \to D^-\pi^+$ decays. With the exception of the scale (which, we recall, is a free parameter in the fit), we observe agreement between data and SP5 within the statistical uncertainties.

  Scale factors derived from the observed width (resolution) ratio of data to SP5 are applied to the PDFs of ΔE and $m_{\rm ES}$, and the fit is repeated to obtain the associated systematics. We find scale factors of 1.00 ± 0.04 (core) and 1.25 ± 0.22 (tail) (double Gaussian fit with relative fraction fixed to SP5 value) for ΔE, and 0.97 ± 0.05 for $m_{\rm ES}$ (single Gaussian fit).

- **MVA PDF:** for the continuum, the NN$'$ PDF is extracted from the nominal data fit by adjusting a polynomial with four free parameters to it. For the truth-matched signal and SCF, fully reconstructed $B^0 \to D^-\pi^+$ decays are used to determine a correction function for the SP5 distribution. The PDFs are

reweighed according to the parameterized ratio and the fit is repeated to obtain the associated systematics.

5.8.3 Tracking and PID Efficiencies

There are discrepencies in the tracking and PID efficiencies between data and MC. To correct the tracking efficiency, we follow the standard *BABAR* procedure in [72]. We apply a flat correction to the efficiency of 0.8% for each track (including the two tracks from the K_S^0 decay), with a systematic of 1.4% from each track for a total of 5.6% systematic. Given our 15% statistical error on the event yield, and the 20% model-dependent error (see Section 5.8.5), this amount of extra systematic error is small.

We also apply the standard SP5 K_S^0 correction tables [72]. This leads to a flat efficiency correction of $(2 \pm 1)\%$. The contribution to the systematic error from the K_S^0 correction is obtained as follows: the recipe provides various K_S^0 correction tables each of which assumes a different set of K_S^0 quality cuts; we determine the correction for our K_S^0 list for each one of these tables, and take the weighted average of the resulting deviations from zero as a measure of the related systematic uncertainty. This amounts to 2.5%, to be added in quadrature with 1% for a total systematic error on the selection efficiency of 2.7%.

In summary, tracking leads to a correction to the efficiency of $C_\epsilon = (1-0.008)^4 * (1-0.02) = 0.949 \pm 0.060$.

For the PID correction, we very conservatively account for systematics the sum of the inefficiencies of the various PID requirements, which amounts to 5%.

5.8.4 B Background

The B background modeling is a major source of systematics in the present analysis.

- The uncertainties from the expected yields are evaluated by varying the individual branching fractions of the contributing modes within the ranges given in Tables 5.3-5.4.

- The uncertainties from the (mostly) unknown CP parameters are evaluated by varying them incoherently between $\pm 1/\sqrt{3} \sim 0.6$, where the factor $\sqrt{3}$ accounts for the reduced RMS when assuming a uniform Bayesian prior for these uncertainties [35]. Known CP parameters are varied within their measurement errors.

- We use the same Δt model parameters for the B background as for signal. All model parameters are varied coherently among all modes for systematics. We neglect the difference in the vertex resolution between a nominal signal candidate and a B-background event.

- The tagging fractions for the B background modes are obtained from MC simulation. The systematics are evaluated by varying them coherently among all modes within their statistical errors.

5.8.5 Quasi-2-Body Approximation: Residual Interference

The systematic error introduced in the Q2B approximation by ignoring interference effects between the f_0 and the other resonances in the Dalitz plot is estimated from simulation by varying freely all relative strong phases and taking the largest

observed change in each parameter as the error. Eleven resonances are used in this studing including the three loweset lying ρ resonances, $f_0(980)$, $f_0(1370)$, $f_2(1270)$, and the $K^{*\pm}$ and higher kaon states. In addition, a non-resonant component is allowed. The proportion of each contribution is estimated using known exclusive measurements and the inclusive $\pi^+\pi^- K^0_S$ rate. The systematic effects due to interference on the *CP* parameters are small compared with statistical error. However, their effect on the branching fraction is large, on the order of 20%, making the branching fraction ratio measurement systematics-error-dominated.

5.8.6 Doubly-Cabibbo-Suppressed *B* Decays

The systematic uncertainties due to interference between the doubly-Cabibbo-suppressed (DCS) $\bar{b} \to \bar{u}c\bar{d}$ amplitude with the Cabibbo-favored $b \to c\bar{u}d$ amplitude for tag-side B decays are discussed in great detail in Ref. [61]. The associated errors on S and C have been obtained from simulation by varying freely all relevant strong phases. We use the numbers corresponding to the $B^0 \to \pi^+\pi^-$ toy MC analysis [61] (they are similar to the corresponding numbers in $B^0 \to \rho^\pm\pi^\mp$).

Source	S	C	$N_{f_0K^0_S}$	$m(f_0)$	$\Gamma(f_0)$
Δm_d	0.007	0.004	0.03	0.0000	0.0001
τ^0_B	0.004	0.001	0.11	0.0000	0.0000
Δt signal model	0.012	0.015	0.13	0.0000	0.0001
Δt continuum model	0.001	0.002	0.45	0.0000	0.0000
Signal tagging fractions	0.003	0.003	0.05	0.0000	0.0001
Mistag probabilities	0.037	0.009	0.04	0.0000	0.0001
Mistag biases	0.010	0.013	0.08	0.0000	0.0002
Misreconstructed signal	0.001	0.001	0.16	0.0000	0.0000
B-background: yields	0.072	0.058	4.23	0.0002	0.0029
B-background tagging fractions	0.009	0.014	0.32	0.0000	0.0003
B-background: CP parameters	0.050	0.037	0.41	0.0000	0.0006
ΔE resolution	0.018	0.003	0.32	0.0001	0.0002
$m_{\rm ES}$ resolution	0.007	0.003	0.42	0.0001	0.0001
PDFs: NN$'$ shape	0.008	0.005	0.20	-	-
Toy biases	0.024	0.022	1.46	0.0001	0.0001
Embedded toy biases	0.058	0.081	2.40	0.0005	0.0011
Tag-side DCS decays	0.013	0.037	-	-	-
Total	0.128	0.118	6.59	0.0006	0.0032
Q2B approximation	0.040	0.067	18.7	0.0040	0.0085

Table 5.8: *Summary of systematic uncertainties on S, C, $N_{f_0K^0_S}$, $m(f_0)$ and $\Gamma(f_0)$ for the $B^0 \to f_0K^0_s$ BR fit, as described in the text. The total systematic errors are obtained by adding up in quadrature all individual sources. The model-dependent errors due to the Q2B approximation (last line) are not included in the total systematic errors quoted. The systematic errors that add to the systematics on the yields when deriving the branching fraction are given in Table 5.9.*

Source	BR
Yield Systematic	0.4
MC stat error on efficiency	0.0 (0.6%)
Tracking	0.4 (6.2%)
B-Counting	0.0 (0.6%)
PID	0.3 (5%)
Total	0.6
Q2B approximation	1.2 (20%)

Table 5.9: *Summary of systematic uncertainties on the branching ratio for the* $B^0 \rightarrow f_0 K_s^0$ *BR fit. The total systematic error is obtained by adding up in quadrature all individual sources.*

Source	S	C	$N_{f_0K^0_S}$
Δm_d	0.005	0.003	0.02
τ^0_B	0.002	0.001	0.19
Δt signal model	0.012	0.008	0.17
Signal tagging fractions	0.001	0.002	1.18
Mistag probabilities	0.031	0.008	0.08
Mistag biases	0.010	0.013	0.08
Misreconstructed signal	0.001	0.001	0.16
B-background: yields	0.033	0.023	7.02
B-background tagging fractions	0.007	0.009	0.79
B-background: CP parameters	0.036	0.063	0.94
ΔE resolution	0.018	0.007	2.11
$m_{\rm ES}$ resolution	0.001	0.001	0.11
PDFs: NN$'$ shape	0.015	0.014	1.66
Toy biases	0.026	0.021	2.04
Embedded toy biases	0.058	0.098	5.11
Tag-side DCS decays	0.013	0.037	-
Q2B approximation	0.040	0.067	-
Total	0.100	0.145	9.39

Table 5.10: *Summary of systematic uncertainties on S, C, and $N_{f_0K^0_S}$ for the $B^0 \to f_0K^0_S$ CP fit as described in the text. The total systematic errors are obtained by adding up in quadrature all individual sources. The model-dependent errors due to the Q2B approximation (last line) are not included in the total systematic errors quoted.*

5.9 Conclusions

We have presented the measurement of *CP*-violating asymmetries in $B^0 \to f_0(980)K^0_S$ decays, using a quasi-2-body approximation. For the fit to Runs 1-4, the results are obtained from a data sample of 209×10^6 $\Upsilon(4S) \to B\overline{B}$ decays collected. From a time-dependent maximum likelihood fit we find 152.2 ± 18.4 signal events. We measure the mixing-induced *CP* violation parameter $\sin 2\beta_{\rm eff} = -S = 0.95^{+0.23}_{-0.32} \pm 0.10$ and the direct *CP* violation parameter $C = -0.24 \pm 0.31 \pm 0.15$.

For the fit to Runs 1-3, the results are obtained from a data sample of 122.6×10^6 $\Upsilon(4S) \to B\overline{B}$ decays. From a time-dependent maximum likelihood fit we find $93.6 \pm 13.6 \pm 6.4$ signal events corresponding to a branching fraction of $\mathcal{B}(B^0 \to f_0(980)(\to \pi^+\pi^-)K^0) = (6.0 \pm 0.9 \pm 0.6 \pm 1.2) \times 10^{-6}$, where the first error is statistical, the second systematic, and the third due to model uncertainties.

Assuming that the decay $B^0 \to f_0 K^0_S$ is dominated by penguin transitions, we can relate our S measurement to $-\sin 2\beta$ to very good accuracy. With this assumption, only a single weak phase contributes to the decay so that direct *CP* violation is absent, which is in agreement with the result for the C parameter. The measured value for S is in agreement with the world average $\sin 2\beta = 0.68 \pm 0.03$ [30] of the charmonium modes.

Bibliography

1. A.D. Sakharov, JETP Letters, vol. 5, pp32-5 (1967).
2. M.B. Gavela *et al.*, Mod. Phys. Lett. A **9**, 95 (1994); Nucl. Phys. **B340**, 382 (1994); P. Huet and E. Sather, Phys. Rev. D **51**, 379 (1995).
3. Particle Data Group (K. Hagiwara *et al.*), Phys. Rev. **D66**, 010001 (2002/2003/2004)
4. Lueders, G. *Kgl. Danske Videnskab. Selskab Mat. Fys. Medd.* **28**, No. 5, 1954.
5. Pauli, W. In *Niels Bohr and the development of physics.* Pergamon, London 1955.
6. Jost, R. *Helvetica Physica Acta* **30**, 409, 1957.
7. Streater, R. F. and Wightman, A. S. *CPT, spin, statistics and all that.* Benjamin, New York, 1964.
8. G.C. Branco, L. Lavoura and J.P. Silva, *CP Violation*, Oxford Science Publications, New York, 1999
9. Lee, T.D. and Yang, C.N. (1956). *Physical Review* **104**, 254, 1956.
10. Wu, C.S., Ambler, E., Haywood, R.W., Hoppes, D.D., and Hudson, R.P. *Physical Review* **105**, 1413, 1957.
11. Christenson, J.H., Cronin, J.W., Fitch, V.L., and Turlay, R. *Physical Review Letters* **13**, 138, 1964.
12. P.F. Harrison and H.R. Quinn, The Babar Physics Book, 1998.
13. M. Beneke and M. Neubert, Nucl. Phys. **B675**, 333 (2003)
14. M. Beneke, B. Buchalla, M. Neubert, C.T, Sachrajda, Phys. Rev. lett. **83**, 1914 (1999)
15. *BABAR* Collaboration, Contribution to ICHEP2006, hep-ex/0607107(2006).

16. Y. Grossman, Talk at Lepton-Photon 2003, hep-ph/0310229 (2003); private communication.

17. G. Hiller, Phys. Rev. D **66**, 071502(R) (2002).

18. A.B. Carter and A.I. Sanda, Phys. Rev. D **23**, 1567 (1981); I.I. Bigi and A.I. Sanda, Nucl. Phys. B **193**, 85 (1981); R. Fleischer and T. Mannel, Phys. Lett. B **511**, 240 (2003);Y. Grossman, G. Isidori and M.P. Worah, Phys. Rev. D **58**, 057504 (1998); Y. Grossman, Z. Ligeti, Y. Nir and H. Quinn, Phys. Rev. D **68**, 015004 (2003); Y. Grossman and M.P. Worah, Phys. Lett. B **395**, 241 (1997); R. Fleischer, Int. J. Mod. Phys. A **12**, 2459 (1997); D. London and A. Soni, Phys. Lett. B **407**, 61 (1997); M. Beneke, Phys. Lett. **B** 620, 143(2005);G. Buchalla, G. Hiller, Y. Nir and G. Raz, JHEP **0509**, 074 (2005).

19. J. Weinstein and N. Isgur, Phys. Rev. Lett. **48**, 659 (1982); Phys. Rev. **D27**, 583 (1983); Phys. Rev. **D41**, 2236 (1990); M.P. Locher *et al.*, Eur. Phys. J. **C4** 317 (1998)

20. R.J. Jaffe, Phys. Rev. **D15**, 267 (1997); M. Alford and R.J. Jaffe, Nucl. Phys. **B578**, 367 (2000)

21. N.A. Torinqvist, Phys. Rev. Lett. **49**, 624 (1982); N.A. Tornquits and M. Roos, Phys. Rev. Lett. **76**, 1575 (1996)

22. F. DeFazio and M.R. Pennington, Phys. Lett. **B521**, 15 (2001); R. Delborgo, D. Liu and M.D. Scadron, Phys. Lett. **B446**, 332 (1999); T.M. Aliev *et al.*, Phys. lett. **B527**, 193 (2002);

23. A.V. Anisovich, V.V. Anisovich and V.A. Nikonov, hep-ph/0011191 (2000)

24. F. Kleefeld *et al.*, Phys. Rev. **D66**, 034007 (2002); E. van Beveren, G. Rupp and M.D. Scadron, Phys. Lett. **B495**, 300 (2000); A. eandrea *et al.*, Phys. lett. **B502**,

79 (2001)

25. *BABAR* Collaboration, hep-ex/0308065 (2003)
26. Belle Collaboration, Phys. Rev. **D65**, 092005 (2002)
27. Belle Collaboration, [arXiv:hep-ex/0610081], submitted to PRL.
28. M. Beneke, G. Buchalla, M. Neubert and C. T. Sachrajda Nucl. Phys. **B606** 245, (2001); M. Beneke and M. Neubert, Nucl. Phys. **B675** 333 (2003)
29. C. Chen, hep-ph/0210028 (2002)
30. The Heavy Flavor Averaging Group (HFAG), http://www.slac.stanford.edu/xorg/hfag/
31. *BABAR* Collaboration, B. Aubert *et al.*, Nucl. Instr. Meth. A **479**, 1 (2002).
32. ARGUS collaboration, H. Albrecht *et al.*, Z. Phys. **C48**, 543 (1990).
33. A. Höcker, S. Laplace F. Le Diberder, V. Shelkov *et al.*, *BABAR* Analysis Document #141 (2001)
34. N. Danielson, A. Höcker, H.M. Lacker, F. Le Diberder, R. Liu, J. Ocariz, M. Pivk, L. Roos and J. Wu, *BABAR* Analysis Document #346 (2001)
35. R. Aleksan, P.F. Giraud, A. Höcker, S. Laplace, F. Le Diberder, R. Liu, H. Li, Y. Pan, V. Shelkov, J. Stark, J. von Wimmersperg-Toeller, J. Wu, S.L. Wu and C. Yèche, *BABAR* Analysis Document #350 (2003); see also *BABAR* Analysis Document #682 (2003)
36. A. Gaidot *et al.*, *BABAR*-Note-461 (1998)
37. P. Gay, B. Michel, J. Proriol, and O. Deschamps, "*Tagging Higgs Bosons in Hadronic LEP-2 Events with Neural Networks.*", In Pisa 1995, New computing techniques in physics research, 725 (1995)
38. N. Arnaud, M. Graham, A. Höcker, S. Laplace, J. Stark, J. Wu and S.L. Wu,

BABAR Analysis Document #637 (2003)

39. A. Gritsan and L.M. Mir, *BABAR* Analysis Document #483 (2003);
    A. Gritsan, Y. Groysman and L.M. Mir, *BABAR* Analysis Document #604 (2003);
    A.J. Bevan, G.A Schott, C. Touramanis, and C. Yeche, *BABAR* Analysis Document #634 (2003)
40. D. Lange *et al.*, *BABAR* Analysis Document #356 (2001);
    B. Dahmes *et al.*, *BABAR* Analysis Document #358 (2002);
    J. Albert *et al.*, *BABAR* Analysis Document #308 (2002);
    S. Ricciardi *et al.*, *BABAR* Analysis Document #381 (2002)
41. *BABAR* Collaboration, B. Aubert *et al.*, Contribution to ICHEP 2006, [arXiv:hep-ex/0308035].
42. J. Beringer, *BABAR* Analysis Document #317 (2002)
43. A. Bevan, G. Cavoto, C. Dallapiccola, N. Danielson, A. Farbin, F. Ferroni, A. Jawahery, D. Kovalskyi, F.R. Le Diberder and J. Olsen, *BABAR* Analysis Document #699 (2001); see also Refs. [40]
44. ARGUS collaboration, *Kaons in flavour tagged B decays*, Z. Phys. **C62** (94) 371
45. *BABAR* Collaboration, Phys. Rev. **D66**, 032003 (2002);
46. J. Smith, A. Soffer and R. Waldi, *BABAR*Note 497 (1999)
47. M. Pivk, Thesis, LPNHE and Université de Paris VI (2003)
48. J. Albert, http://babar-hn.slac.stanford.edu:5090/HyperNews/get/EHBDOC/272/1.html (2001)
49. A. Roodman, Proceedings of PhyStat2003, SLAC, Stanford, California, Sept. 8-11, 2003 physics/0312102.
50. G. Cavoto; E. Di Marco; F. Ferroni; M. Pierini, *BABAR* Analysis Document #1131

(2005)

51. A. Gritsan, *BABAR* Analysis Document #498 (2003)
52. D. Dujmic, *BABAR* Analysis Document #737, #819 (2003)
53. *BABAR*Analysis Document #890 (July 2004)
54. F. Bianchi *et al.*, *BABAR* Analysis Documents #357, #224 (2001-2002)
55. P. Clark, K. Ford, W. Gradl, M. Graham, A. Höcker, P. Kutter, E. Olaiya, J. Wu, S.L. Wu, Y. Xie, *BABAR* Analysis Document #810 (2004)
56. D. Dujmic, A. Gritsan, M. Krishnamurthy, S. Spanier, A. Telnov, *BABAR* Analysis Document #742 (2003)
57. H. Li, R. Liu, A. Mihalyi, Y. Pan, J. Wu and S.L. Wu, *BABAR* Analysis Document #573 (2003)
58. A. Höcker, P.E. Kutter, S. Laplace, H. Li, R. Liu, A. Mihalyi, Y. Pan, V. Shelkov, J. Wu, S.L. Wu and Z. Yu, *BABAR* Analysis Document #667 (2003)
59. A. Höcker, P. Kutter, S. Laplace, Y. Pan V. Shelkov, Z. Yu and S.L. Wu, *BABAR* Analysis Document #494 (2003)
60. H. Li, R. Liu, A. Mihalyi, Y. Pan, J. Wu and S.L. Wu, *BABAR* Analysis Document #575 (2003)
61. O. Long and M. Baak, *BABAR* Analysis Document #572 (2003)
62. M. Davier, hep-ex/0312064 (2003)
63. E791 Collaboration (E.M. Aitala *et al.*). Phys. Rev. Lett. **86** 770, (2001)
64. E791 Collaboration (E.M. Aitala *et al.*). Phys. Rev. Lett. **86**, 765 (2001)
65. K. Ford, P. Harrison, S. Morgan and E. Olaiya, *BABAR* Analysis Document #581 (2003)
66. L.M. Mir and A. Gritsan, *BABAR* Analysis Document #381 (2003)

67. See discussion of possible $B^0 \to \kappa(797)^+\pi^-$ contributions in: P. Chang for the Belle Collaboration, *"Charmless multi-body B decays"*, talk given at ICHEP'02. For more information on the $\kappa(797)^+$, see: Fermilab E791 Collaboration, Phys. Rev. Lett. **89**, 121801 (2002)

68. Belle Collaboration (K. Abe *et al.*), KEK-PREPRINT-2001-76, BELLE-CONF-0115 (2001)

69. J. Back, *BABAR* Analysis Document #505.
W. Bhimji, N. Chevalier, T.E. Latham, H.W. Shorthouse and F. Wilson, *BABAR* Analysis Document #362 (2003)

70. *BABAR* Collaboration, hep-ex/0306030, *submitted to PRL* (2003); *BABAR* Analysis Document #489 (2003); Analysis description in Ref. [35]

71. K.S. Cranmer, "*Kernel Estimation for Parameterization of Discriminant Variable Distributions*", ALEPH 99-144 (1999)
(see also http://www-wisconsin.cern.ch/~cranmer/keys.html)

72. Recipe for correcting MC tracking efficiencies and assigning systematics, http://www.slac.stanford.edu/BFROOT/www/Physics/TrackEfficTaskForce/TrackingTaskForce-2004.html

73. Belle Collaboration, Phys. Rev. Lett. **91**, 261602 (2003)

74. S. Spanier and M. Krishnamurthy, *BABAR* Analysis Document #772 (2003), *to be submitted to PRL*

75. A. Farbin *et al.*, *BABAR* Analysis Document #849 (2003)

76. R. Fleischer and T. Mannel, Phys. Lett. **B506** 311 (2001)

77. A. Farbin *et al.*, *BABAR* Analysis Document #774 (2003)

78. WA76 Collaboration (T.A. Armstrong *et al.*). Z. Phys. **C51**, 351 (1991)

79. S. Gardner and U.G. Meissner, Phys. Rev. **D65**, 094004 (2002);
U.G. Meissner, Talk at International Workshop on Heavy Quarks and Leptons, Vietri sul Mare, Salerno, Italy, May 2002, hep-ph/0206125

80. L.M. Barkov *et al.* (OLYA, CMD Collaboration), Nucl. Phys. **B256** (1985) 365.

81. M. Krishnamurthy, S. Spanier, *BABAR* Analysis Document #713 (2003)

82. Muriel Pivk and Francois R. Le Diberder, arXiv:physics/0402083.

83. ALEPH Collaboration, (R. Barate *et al.*), Z. Phys. **C76** 15, (1997)

84. S. Bagnasco, R. Baldini-Ferroli, V. Brigljevic, C. Campagnari, B. Dahmes, G. Finocchiaro, D.J. Lange, S. Passaggio, W. Verkerke, D. Wright, R. de Sangro, *BABAR*Analysis Document #56 (2001)

85. A. Deandrea, A.D. Polosa, Phys. Rev. Lett. **86**, 216 (2001);
A. Deandrea, R. Gatto, M. Ladisa, G. Nardulli, P. Santorelli, Phys. Rev. **D62**, 036001 (2000)

86. Y. Grossman, Z. Ligeti, Y. Nir and H. Quinn, Phys. Rev. **D68**, 015004 (2003)

87. J.H. Kühn and A. Santamaria, Z. Phys. **C48** 445, (1990)

88. H.C. Huang (for the Belle Collaboration), hep-ex/0205062 (2002)

89. J. Tandean and S. Gardner, Phys. Rev.**D66**, 034019 (2002)

90. J. Blatt and V. Weisskopf, *"Theoretical Nuclear Physics"*, John Wiley & Sons, New York, 1956

91. G.J. Gounaris and J.J. Sakurai, Phys. Rev. Lett. **21** 244, (1968)

92. *BABAR* Collaboration, Phys. Rev. Lett. **91**, 161801 (2003)

93. R. Fleischer and T. Mannel, Phys. Lett. **B511** 240 (2001)

94. K. Abe *et al.* [Belle Collaboration], Phys. Rev. Lett. **91**, 261602 (2003) [arXiv:hep-ex/0308035].